Towards a hydrogen-driven society?

Calculations and neutron scattering on potential hydrogen storage materials

Towards a hydrogen-driven society?

Calculations and neutron scattering on potential hydrogen storage materials

PROEFSCHRIFT

ter verkrijging van de graad van doctor
aan de Technische Universiteit Delft,
op gezag van de Rector Magnificus Prof.dr.ir. J.T. Fokkema,
voorzitter van het College voor Promoties
in het openbaar te verdedigen op dinsdag 1 februari 2005 om 15.30 uur

door

Hendrikus Gijsbertus SCHIMMEL

natuurkundig ingenieur
geboren te Gouda

Dit proefschrift is goedgekeurd door de promotor:
Prof. dr. G.J. Kearley

Toegevoegd promotor:
Dr. F.M. Mulder

Samenstelling promotiecommissie:
Rector Magnificus   voorzitter
Prof. dr. G.J. Kearley   Technische Universiteit Delft, promotor
Dr. F.M. Mulder   Technische Universiteit Delft, toegevoegd promotor
Prof. dr. J. Huot   Université du Québec à Trois-Rivières, Canada
Dr. M.R. Johnson   Institut Laue-Langevin, France
Prof. dr. K.P. de Jong   Universiteit Utrecht
Prof. dr. P.H.L. Notten   Technische Universiteit Eindhoven
Prof. dr. J. Schoonman   Technische Universiteit Delft

Printed in the Netherlands

Contents

Chapter 1

Towards a hydrogen-driven society?

In this chapter we first deal briefly with the history of transport and show thereafter that concerns about greenhouse gasses bring on the need for a sustainable solution for our mobility, probably using hydrogen as an energy carrier. Finally we present the research questions that are dealt with in this thesis and describe the limiting conditions for practical hydrogen storage materials.

1.1 Transport and trade: a short time-line

When the primary necessities of life are fulfilled, luxury goods become important. The definition of luxury goods depends very much on what one is used to: when everything that King Midas touched became gold, he obviously regarded food as more luxury than gold. However, generally people regard objects from remote areas, rare items or products which are labor intensive as luxury. The distance between supply and demand markets and the scarcity of these goods stimulates the development of trade. As goods and people need to be transported, wealth, trade and transport are interdependent.

History has shown that the availability of a fast, cheap, reliable and safe transport system stimulates trade and wealth. An example is the highly developed society along the banks of the Nile in Egypt, relying very much on transport over the river and the seas and on camelback through the deserts. Solomon was able to build the beautiful temple in Jerusalem by importing cedar and cypress from Lebanon. The Phoenicians that lived there were very good sailors and they traded with virtually all cities on the Mediterranean coast, which brought them prosperity and power. The expansion of the Roman Empire – expansion and power are luxury goods for leaders – and the simultaneous development of trade in Europe was possible due to a superb road system and the use of ships. Not to name more, the construction of ships that could sail across the oceans by the end of the 15$^{\text{th}}$ century, brought the seafaring nations richness and power. The older parts of many European cities show

Figure 1.1: The speed record holder in 1899, Jenatzy's electric car "La jamais contente", reached speeds over 100 km/h.

that the availability of a free entrance to the sea brought wealthiness in those times.

With the construction of the first practical steam engine in 1712 by Newcomen, a new age was entered. A machine was constructed which was able to supply work on demand and without fatigue, albeit on the expense of fuel. His engine was highly inefficient, but apparently economical as more than 100 engines were installed before the end of the patent in 1733. Efficiency and safety were continuously improved, and the first steam engines appeared on board of ships and trains around 1800. Coal was often used for transport engines, because of its high energy density as compared to wood, making farther destinations accessible without refuelling.

Soon afterwards the first electric motor was constructed, whose source of electric energy was a Voltaic pile, which was expensive and low-power. Better electric motors, generators and batteries were available shortly afterwards and the first electric vehicle was made in 1881. The competitor of the electric motor, the internal combustion engine, was invented in 1876 and found its first use in a car made by Karl Benz in 1885. The horseless age dawned.

Around the turn of the century electrical vehicles and internal combustion engines were competing options: between 1899 and 1901 the maximum speed record was held by the aluminum alloy battery-powered car 'La Jamais Contente' of Camille Jenatzy shown in figure 1.1. The number of electric and internal combustion driven cars being sold was about equal in those days. A great number of electric vehicles were manufactured and used for instance as taxis in New York city [1]. The advantages of the electric cars were their reliability, quietness and cleanliness, the internal combustion counterparts being noisy, smoky and less reliable. The internal combustion engine, however, was, because of its lower weight, better in climbing hills, had a longer range and did not need time-consuming refilling stops in the steam driven electricity station.

Given this situation the decline of the electric vehicles is remarkable: by 1913 virtually all cars sold were powered by internal combustion engines [1]. The discovery of new oil wells and the ever improving engines strengthened the position of internal combustion engines against the electric ones. The monopoly of the internal

combustion engine for road transport use lasted for more than half a century. When the oil prices quadrupled during the oil crisis in 1973, awareness grew that the sole dependence on fossil fuels made nations vulnerable. More interest rose for battery and solar cell powered cars. The recent world solar challenges in Australia have shown that it is indeed possible to travel large distances on energy from sunlight only, but it is currently neither economical nor practical.

A major step forward was made in 1997 by Toyota, when the company introduced the Prius, the first hybrid production car. Hybrid cars have an electric and an internal combustion engine combined with a battery pack and can achieve a higher overall efficiency by reducing idling and braking losses. While other companies showed demonstration cars using hydrogen and fuels cell, Toyota realized that the hybrid concept may become important in the near future, and that serious applications of hydrogen and fuel cells are not just around the corner [2].

We should not, though, trivialize the need for alternative fuels and energy carriers. Hubbert's model of a peak in the world oil production is as applicable globally as is has proven to be for American oil production rates [3, 4]. Recently Aleklett and Campbell predicted such a peak in the global crude oil production rates to occur around the year 2010 [5] and the International Energy Agency predicts this peak in 2030 [6].

1.2   Sustainability and mobility

Since several decades, people realize that the combustion of fossil fuels to fulfil our energy demands has serious drawbacks such as the pollution of air and environment, global warming and the limited availability of fossil fuels on earth. During the United Nation Conference on Environment and Development known as 'The Earth Summit' that was held in 1992 in Rio de Janeiro, these concerns were discussed. The need to sustain the availability of the natural resources of the earth was acknowledged. New developments therefore need to be sustainable and existing processes need to be transformed. In particular, the fossil fuel resources are finite and sustainable development means that we rely on other sources than fossil fuels for our energy demands. Nations promised to reduce the emission of green house gasses, such as CO_2 and confirmed this at the summits in Johannesburg and Kyoto. A stabilization of the carbon dioxide content of the atmosphere does not necessarily mean that no CO_2 is emitted. When the fuel is renewable from atmospheric CO_2, no net emission occurs. Sources such as wind, sunlight and biomass are regarded renewable in this context. Because nuclear power has no CO_2-emission, it is often considered to be sustainable, though strictly speaking it is not since it depletes uranium resources.

The energy sources used for thousands of years were renewable as they were part of natural cycles powered by energy from sunlight. The use of sails to propel ships may serve as an example. The storage of 'fuel' for the crew was no problem as ships were large enough to take food for a long period. Fuel storage became an issue when the steam engines appeared in the 18$^{\text{th}}$ century. For most ships and

locomotives wood could not be used as a fuel, because of its low energy density. Non renewable energy sources with a high energy density such as coal and oil became popular. By now people want to return to renewable processes, albeit under one condition: the standard of living that was made possible by the use of fossil fuels should be maintained.

Carbon dioxide emissions can be prevented relatively easy in *stationary* applications by switching from fossil fuels to nuclear, hydro, wind or solar energy feeded systems, though only the first two options are economical at the present time, since the latter two need state subsidy. The social acceptance for nuclear energy is low due to safety issues and the waste problem, while hydro power is limited to places with suitable geographic relief and water flow. For *mobile* applications, the onboard generation of energy from these sources is unfeasible. Problems are safety concerns (in the case of nuclear power) and the limited availability of the primary energy sources on the place where mobility is desired (for hydro-power, wind and sunlight). We conclude that a prerequisite for sustainable development is the availability of a reliable, economical, safe and fast mechanism for the storage of energy onboard a vehicle.

1.2.1   The storage of energy

We return shortly to the end of the 19th century to point out the remarkable fact that, given the wide spread use of electric vehicles by then, there are hardly any on the roads nowadays. The problems of internal combustion engines; their noisiness, emission of unhealthy fumes and unreliability could step by step be solved by improvements in the design of the engine, while electric engines could hardly be improved: the efficiency of the electric Jeantaud vehicle used in the Paris-Bordeaux-Paris race in 1895 was already very good (92.5% at 5 kW), even by present standards [1].

Why so much progress was made for internal combustion engines, while electrical cars virtually disappeared? Electricity has changed our life in plants, behind our desks, in our kitchens and living-rooms, but it did not change the processes under the hood of our cars. An answer to the question is that we know how to produce electricity, we know how to use it, but we have no feasible solution to the *storage* of large amounts of energy. The bottle neck for electric cars was and is the battery pack. Storing practical amounts of energy in a limited volume and weight is one of the most challenging problems we face nowadays. As long as oil is widely available for low prices, the solution has to compete with the enormous energy density and ease-of-use of fluid fossil fuels.

Hydrogen

When a metal such as iron and a strong acid are brought together, a gas escapes as was already known to Paracelsus (1493-1541). In 1766 Henry Cavendish showed in a paper to the Royal Society of London that this gas ('flammable air') was an elementary substance, distinguishable by its density from other gasses. Antoine Laurent Lavoisier found that it generated water when burned with air and gave the element its name hydrogène. In 1839 Sir William Robert Grove was able to convert the energy being freed in this reaction directly into electrical energy with his 'gas battery', consisting of bottles with platinum electrodes, one filled with hydrogen and the other with oxygen. When the bottles made contact via diluted sulphuric acid, a current between the electrodes began to flow and water was formed in the bottles. His 'gas battery' shown in figure 1.2 was the first demonstration of a fuel cell.
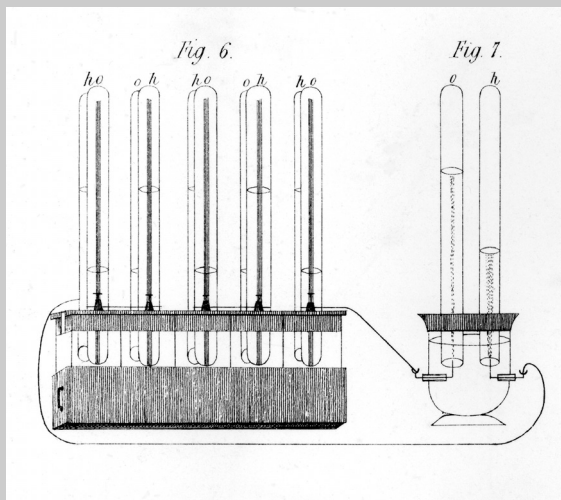
Figure 1.2: The figures reproduced from Grove's paper on the gas battery to the Royal Society of London[7].

1.3 Hydrogen the fuel of the future?

Nowadays headlines in the newspapers tell us that hydrogen is the fuel of the future. In the State of the Union of 2003, president Bush of the United States of America promised money to pave the way to the economical use of hydrogen in cars. Hydrogen is regarded to be the fuel of the future because its energy can be transformed into mechanical or electrical energy with high efficiencies (50-60 %) when used in a fuel cell [8, 9], without the emission of CO_2 or pollutants. Applied in an internal combustion engine, hydrogen behaves similar to known fuels, again without CO_2 emission. In this sense hydrogen is indeed a perfect and sustainable fuel. However, it is important to realize that hydrogen is not a primary energy source, but merely an energy carrier, which has to be produced from primary energy sources.

To make a substance a good fuel for mobile applications, it is not sufficient to know how energy can be converted to mechanical energy efficiently and without pollution. The storage properties are of decisive importance for mobile applications. Hydrogen transportation, however, faces us with a serious problem. Hydrogen is the lightest element on earth and it is very volatile. Despite its high energy content per kilogram of hydrogen (three times that of gasoline), it has the drawback that the volume of one kg of hydrogen is roughly 10 m^3 under standard conditions. Realizing that we need at least 4 kg of hydrogen to drive 600 km with a fuel cell powered

car, this is a gigantic volume that needs to be reduced for practical purposes. A hydrogen storage tank should be safe, compact, light, long lasting, economical and should preferably not contain poisons or pollutants. It is the storage of hydrogen as a fuel this thesis is about.

1.3.1   Questions and outline

Two obvious options for the storage of hydrogen have been shown to work: cooling hydrogen below its critical point to condense it and secondly compressing the hydrogen gas to high pressures. The first option was used by BMW in demonstration cars. The second option is now used by several public transport companies in buses in e.g. Amsterdam. Both options have drawbacks such as the cost of operation, evaporation of hydrogen gas due to heat leakage, safety issues concerning the high pressures used or the volume of the storage containers. The common approach is to find a material which attracts hydrogen, thereby lowering the pressure that is needed to achieve useful hydrogen densities. The options for such a material are nowadays commonly divided into two: 1) storage by adsorption on surfaces and 2) by chemical absorption for instance interstitially in a crystal lattice. We distinguish between *ad*sorption on surfaces and *ab*sorption inside materials. Open questions are which optimal properties a hydrogen storage material needs to have, which of the above named options is the best to store hydrogen, how mechanisms of sorption can be improved and which role can catalysts play here?

   In this thesis we report research on the questions given above. This thesis has been written in a review-type format. The body of the thesis consists of three relatively small chapters, including the present and some concluding remarks. Considering the technical targets set for hydrogen storage, we first define the minimum requirements of a hydrogen storage material in the next section. Then we introduce two subjects: hydrogen storage by physisorption on high surface area materials, mainly carbon materials in chapter 2 and kinetics of the storage of hydrogen interstitially in metals such as magnesium in chapter 3. We draw some general conclusions in the fourth chapter. Our results were also published in the form of articles in peer-reviewed journals where more experimental details, analysis and discussion are presented. For the interested reader these articles have been included as appendices. We reckon that this format makes the main text of this thesis more accessible for the general public due to its summarizing and review-type character.

1.4   Chemical potentials and hydrogen storage targets

The department of energy of the United States has set a range of targets for on-board hydrogen storage systems [10]. Parameters that depend very much on the materials used for hydrogen storage and less on the actual realization of the storage system are

Table 1.1: Some DOE technical targets: On-Board Hydrogen Storage Systems [10].

				Year	
Storage Parameter	Symbol	Units	2005	2010	2015
net useful H_2/max system mass		kg H_2/kg	0.045	0.06	0.09
net useful H_2/max system volume		kg H_2/l	0.036	0.045	0.081
Energy efficiency of system	η_{stor}	%	90	90	90
Storage system cost		\$/kg H_2	200	133	67
Min. pressure of H_2 from tank	P_{use}	bar	2.5	2.5	2
Refuelling rate		kg H_2/min	0.5	1.5	2
Loss of useable hydrogen		(g/hr)/kg H_2	1	0.1	0.05

summarized in table 1.1. To assess whether a certain material can store hydrogen in a way that is efficient with respect to energy conservation considerations, one should examine the thermodynamics of the chemistry that is involved.

A storage material for hydrogen can in general be described as a thermodynamic system with a certain number of sites, N, per unit amount of storage material and the Gibbs free energy, G_{mat}, assuming that G_{mat} does not depend on the hydrogen site occupancy, θ. The Gibbs free energy, G_{mat}, of hydrogen in the storage material is defined as $G_{mat} = H_{mat} - TS_{mat}$, where T is the temperature of the system, H_{mat} is the sorption enthalpy and S_{mat} is the entropy contribution. Properties of the system in equilibrium may be derived from the chemical potential of the hydrogen atom in the material which is defined as $\mu = (\mathrm{d}G_{mat}/\mathrm{d}n)_{T,P}$, where n is the number of hydrogen atoms that occupy sites in or on the material.

Some storage materials, such as Mg and Mg_2Ni form stoichiometric compounds where all available sites are filled. The entropy contribution to the chemical potential is then negligible because no freedom in the arrangement is left[1] and the chemical potential can be approximated by $\mu_{mat} = H_{mat}$, when H_{mat} is given in J/mol H_2. Such materials exhibit a plateau in the average chemical potential versus overall hydrogen occupation since a two phase equilibrium is established.

On the other hand, materials that possess a gradual change in site occupancy when the chemical potential of the gas increases like Pd, Nb and typical physisorption materials, possess an entropy contribution that varies with occupancy and which can be approximated by $(\mathrm{d}S_{mat}/\mathrm{d}n)_{T,P} = R\ln[(1-\theta)/\theta]$. For a site occupancy $\theta = 0.5$, the entropy contribution is zero again and the chemical potential of the storage material is equal to the absorption enthalpy only: $\mu_{mat} = H_{mat}$.

In equilibrium the chemical potential of hydrogen in the storage material is equal to the chemical potential of the hydrogen gas, $\mu_{mat} = \mu_{H_2}$. Hydrogen is loaded from the gas-phase using a pressure P_{load}, for which the Gibbs free energy and thus the chemical potential has been determined experimentally as a function

---

[1]The difference in entropy between Mg and MgH_2 at 298.15 K is only 1.6 J/(K mol) [11]

of temperature and pressure [11, 12] ($\mu = G$ for a single component system). We conclude that the absorption enthalpy needs to be more negative than the chemical potential of hydrogen gas at a certain temperature and pressure in order to achieve a site occupancy of at least 0.5:

$$H_{mat} \leq \mu_{gas}(T, P_{load}). \tag{1.1}$$

The target that has been set for the efficiency of the storage system, puts additional restrictions on the range of possible adsorption enthalpies, H_{mat}. We use the following assumptions: a) for high temperature (HT) systems that operate above the temperature of the environment, $T_{op} > T_{env}$, the heat that is generated during absorption is dissipated to the environment, while the heat input needed to release hydrogen from the storage material costs energy from the fuel and b) for low temperature (LT) systems that operate below the temperature of the environment, $T_{op} < T_{env}$, the heat of absorption has to be brought to T_{env}, which costs energy from the fuel, while the heat input needed for the release of hydrogen comes from the environment. Furthermore we take the ideal Carnot efficiency for the amount of energy needed to establish these energy flows. The Carnot efficiency,

$$\eta_C = \frac{T_h - T_l}{T_h} = 1 - \frac{T_l}{T_h}, \tag{1.2}$$

is the maximum theoretical efficiency of any cyclic heat engine that provides work from a heat flow between a high temperature reservoir with a temperature T_h and a low temperature reservoir at T_l. For systems that pump heat from a low temperature reservoir to a high temperature reservoir, the expression is inverted and the maximum theoretical efficiency is given by

$$\eta_C = \frac{T_h}{T_h - T_l}. \tag{1.3}$$

These energy costs should be weighed against the useable energy content in hydrogen gas, which is $H_{H_2} = 240$ kJ/mol H_2 (lower heating value, i.e. exhaust gases are at 150 degrees Celsius) for the reaction of hydrogen gas with oxygen to form water.

For HT systems we derive that the practical storage efficiencies exceed η_{stor} when the adsorption enthalpies fulfill:

$$H_{mat,HT} \geq \frac{H_{H_2}(1 - \eta_{stor})}{1 - T_{env}/T_{op}}, \tag{1.4}$$

and for LT systems T_{op} and T_{env} are exchanged:

$$H_{mat,LT} \geq \frac{H_{H_2}(1 - \eta_{stor})}{1 - T_{op}/T_{env}}. \tag{1.5}$$

Finally we consider the fact that the work needed to compress hydrogen isothermally from the desorption pressure, P_{des}, to the working pressure, P_{use}, is theoretically $RT \ln(P_{use}/P_{des})$ (treating H_2 as an ideal gas). If the energy efficiency of the
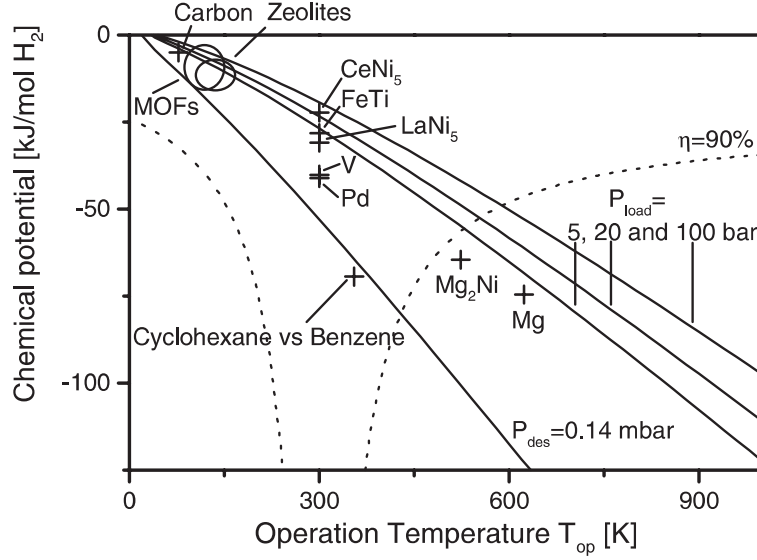
Figure 1.3: The chemical potentials per H_2 formula unit of different hydrogen storage materials plotted against their operation temperature. The upper three solid lines mark the chemical potentials of hydrogen gas for loading pressures of 5, 20 and 100 bar and the lowest one for the minimum decomposition pressure of 0.13 mbar (taking minimum storage efficiency $\eta_{stor} = 0.9$). The dotted line gives the operation temperature at which the energy efficiency of storage is 90%.

process needs to be higher than η_{stor}, this means that the desorption pressure should be higher than:

$$P_{des} \geq P_{use}\,\mathrm{e}^{-\frac{(1-\eta_{stor})H_{H_2}}{RT}},\tag{1.6}$$

which is 0.13 mbar at P_{use}=2 bar and $T = 300$ K. Using $\mu_{mat} = H_{mat}$ again, we get the last equation:

$$H_{mat} \geq \mu_{gas}(T, P_{des}).\tag{1.7}$$

The conditions in equation (1.1) to equation (1.7) define a region in the H–T plane where materials need to be positioned. They are visualized in figure 1.3 using $T_{env} = 300$ K, $P_{load} = 5$, 20 and 100 bar, $P_{use} = 2$ bar and $\eta_{stor} = 0.9$ as a function of the temperature of operation, T_{op}. We note that practical efficiency limitations may be much stricter since the efficiencies that were used for these calculations are theoretical maximum values.

The overall efficiency may be increased when the waste heat from a fuel cell can be used to desorb hydrogen from the storage material The restrictions given by equation (1.4) then shift to higher temperatures. However, for successful applications, breakthroughs in the operation temperature of the electrolyte are needed so that the fuel cells can work at 200-300 degrees Celsius, depending on the storage material that is used. Recently it was shown that this indeed works using acid-doped polybenzimidazole membranes, which operate between 100 and 200 degrees Celsius,
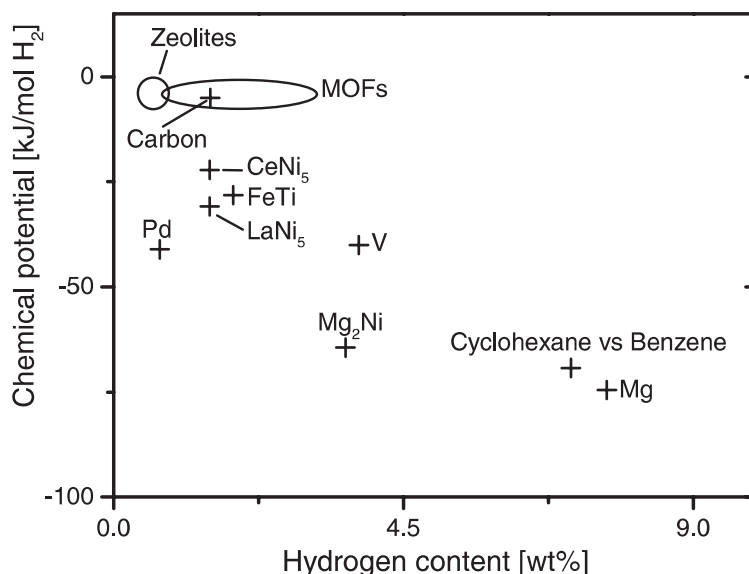
Figure 1.4: Enthalpies of hydrogen storage materials plotted against their maximum theoretical storage capacities in weight percentages.

high enough to desorb hydrogen from $NaAlH_4$ [13]. Apart from this advantage, the higher operation temperature makes the catalyst much less sensitive to poisoning.

The weight capacity of a hydrogen storage material is a very important property, especially when one considers vehicle applications. We visualize the hydrogen densities by weight in figure 1.4, where we plot the absorption enthalpy of a selection of hydrogen storage materials as a function of their weight capacity. We note that the hydrogen content by weight of carbon materials is plotted at 2 wt%, much lower than values reported in literature before. The second chapter of this thesis reviews the claims for hydrogen storage on carbons, carbon nanotubes and nanofibers and addresses the fundamental differences between hydrogen storage on carbon nanotubes and other forms of graphite.

The plot shows clearly that magnesium is still a very important material for hydrogen storage applications due to its low weight. Provided that the operation temperature can be lowered and the absorption enthalpy can be increased (i.e. less negative), magnesium metal and magnesium compounds are good candidates for hydrogen storage materials. If a fuel cell would be developed that operates at ≈ 300 degrees Celsius, the overall efficiency of operation and storage would be improved because the heating of the MgH_2 could then be supplied by the excess heat from the fuel cell. In the third chapter of this thesis we treat magnesium as a model system and concentrate on the kinetic limitations that exists for hydrogen cycling in metal hydrides.

Chapter 2

Hydrogen storage on surfaces

When a molecule is adsorbed on the surface of a material while no chemical bonds are broken or formed, we speak of physisorption. A physisorbed molecule remains intact as a molecule and by heating it can easily be removed from the host. A well known example is adsorption of water in zeolites, in which case the interaction between a polar molecule and an ionic surface gives a relatively strong interaction. Polar molecules induce dipoles in non polar surface and vice-versa, which also leads to an attractive potential. The lowest adsorption potentials can be found between two non-polar objects, which are attracted by London dispersion forces [14]. In this case, the total energy of two neutral objects in each others neighborhood is lowered when they induce dipoles in each other, leading to attraction. The resulting forces are very weak and decay with the seventh power of the distance. The research described below concentrates on hydrogen storage on carbon materials, whose mutual attraction results from these dispersion forces. The adsorption enthalpy for hydrogen on carbon materials is just feasible for hydrogen storage, according to the conditions shown in figure 1.3.

In the form of graphite, carbon is a material which is essentially two dimensional, with the typical hexagonal structure. The bond between carbon atoms in a graphite plane is strong, whereas forces between graphite planes are weak. Because the two dimensional graphite planes are rather stable on their own, exfoliated graphitic materials may possess very high surface areas.

2.1   Hydrogen storage on activated charcoal

Activated charcoal is prepared from raw materials (e.g. peat, lignite, coal), carbonized and reacted with steam at 1000 degrees Celsius. In this way some of the carbon atoms are removed by gasification, which yields a very porous structure. Activated carbons are highly micro- and mesoporous carbon materials, with a surface area ranging from 1000 m^2/g to more than 2000 m^2/g. The structure of these materials is very chaotic, which is caused by the production method.

That carbon materials with a sufficient high surface area might store an amount

of hydrogen that is interesting for applications, has been realized since several decades [15]. Nijkamp et al. systematically studied the amount of hydrogen adsorbed by different types of activated carbon materials [16]. Hydrogen storage capacities scale with the surface area obtained using BET-analysis with nitrogen at 77 K, though some scatter is present in the results.

2.2 Storage capacity reports for nanotubes and nanofibers

When graphite discs with a diameter of a few nanometer are stacked, one obtains a nanofiber with a platelet structure. A herringbone nanofiber is stacked from cone-shaped graphite elements, and a multi walled nanofiber is formed from concentric tubes of enrolled graphite sheets. A new tubular form of carbon, the single walled carbon nanotube (SWNT), was discovered by Iijima in 1991 [17]. Enrolled two dimensional graphite sheets form tubes with diameters around 1.3 nm. Since theoretically the surface area of a free graphite plane is as high as 2600 m^2/g, much interest for hydrogen storage applications was generated. The high hydrogen storage amount (5-10 wt%) and high adsorption enthalpy (19.6 kJ/mol) reported for a sample containing 0.1–0.2 wt% single walled carbon nanotubes (SWNT) stimulated research world-wide [18]. Soon even more astonishing results were published: 10–60 wt% hydrogen storage in graphitic nanofibers at ambient temperature and 125 bar [19, 20] and 14–20 wt% hydrogen storage in lithium and potassium doped multi walled carbon nanotubes [21]. These results could not be understood using different types of calculations [22, 23, 24, 25, 26, 27, 28] and some were explicitly falsified [29, 30, 31, 32].

More realistic results were reported by Ahn et al. [29] ($\approx$ 0.2 wt% in nanofibers at 100 bar and RT, room temperature), Liu et al. [33, 34] (4.0–4.2 wt% in SWNT at 100 bar and RT), Stroebel et al. [35] (1.5 wt% in activated carbon at 125 bar and RT), Tibbets et al. [36] (0.05 wt% for SWNT at 36 bar and RT) Ritschel et al. [37] (0.05–0.63 wt% at 45 bar and RT), and Gundiah et al. [38] (3.7 wt% in SWNT at 100 bar and RT). At 77 K and 1 bar Schimmel et al. measured a hydrogen storage capacity of 0.54 wt% for SWNT and 2 wt% for a high surface area activated carbon [39].

2.2.1 Sources of discrepancies

Several causes can be named to explain the differences between published hydrogen storage capacities. First we like to point out that some of the early measurements on SWNT were performed on samples containing a very limited amount of SWNT (i.e. less than 1 %), to which the hydrogen sorption was attributed completely. Secondly, the gravimetric method which is widely used to study adsorption phenomena is not accurate enough for hydrogen as its mass is very low (the lowest of all gases). Fur-

thermore one should also take into account the volume of the sample that displaces a volume of gas, leading to differences in read-out between different purge gases (e.g. between H_2 and Ar). Since virtually all impurities present in hydrogen gas are much heavier *and* possess a higher adsorption potential on most adsorbents, the method, unless very carefully used, may overestimate the hydrogen storage capacity by more than an order of magnitude. Researchers who used a volumetric method, can be caught by the third difficulty which is connected to the amount of gas that adsorbs in the sample relative to the amount that is present in gaseous form in the measurement volume. The volumetric method involves the measurement of the pressure drop of hydrogen gas in a known volume, with and without a sample. When experiments are performed at high pressures, the above mentioned ratio might be extremely low, so that temperature fluctuations as small as a few degrees causes errors as large as the actual storage capacity. This problem can be circumvented when one avoids high pressures and uses large sample amounts in small sample volumes. Finally a fourth source of confusion might be the definition of the hydrogen storage capacity. The most strict and most common interpretation uses the amount of hydrogen which is stored in a vessel filled with the sample material compared to the amount of hydrogen stored in the same but empty vessel under the same conditions. Using this definition of the *excess amount*, some hydrogen adsorbing materials have a negative storage capacity. Researchers that only measure the weight change of a sample, effectively measure the excess amount which is not corrected for self volume of the sample material.

2.2.2 Open questions

Several fundamental and important questions remained unanswered: How does hydrogen adsorb in nanostructured carbon materials such as SWNT and activated carbons? Does a hydrogen molecule form a chemical bond with the carbon nanotube adsorbent or is the interaction purely physical (i.e. the hydrogen molecule experiences a weak interaction potential and stays intact)? Is the interaction potential similar between hydrogen and nanotubes and between hydrogen and planar graphite? What is the accessible surface area of a carbon nanotube sample? What types of sites are available for hydrogen adsorption? What is the influence of the curvature of the tubes on the hydrogen storage properties of a SWNT sample?

2.3   Simulation results

Many authors tried to understand the reported high adsorption capacities using simulation results. These can be divided on the basis of the assumptions in the simulation method. When force field methods are used, no chemical bond activation is possible and only physical adsorption takes place, in which hydrogen remains a molecule. *Ab initio* methods do allow chemical absorption, in which bonds are broken and new ones are formed. Most authors find relatively high adsorption

capacities, as the interiors of the tube are generally supposed to be accessible as well.

2.3.1 Classical grand canonical Monte Carlo calculations

For classical simulations effective potentials are used to evaluate the forces acting between hydrogen molecules and the graphite layer. Williams et al. calculated the surfaces area of bundles of nanotubes with different diameters [40, 41]. They find that the inside of the tubes has a specific surface area of 783 m^2/g and that the outer surface area of the bundles varies between 0 and 1893 m^2/g, depending on the bundle diameter. The interstitial and groove sites are reported to have a low effective surface area, again depending on the bundle diameter, of about 50 m^2/g for larger bundles. The hydrogen storage capacity for a seven-tube bundle at 77 K and 10 MPa is 5.5 wt%, assuming that the inside of the tube is accessible for hydrogen. According to similar calculations by Wang and Johnson and by Cracknell, the experimental results for nanofibers (from Chambers et al.) are inconsistent with any reasonable physisorption model [42, 43, 24]. Rzepka et al. found the same and concluded further that capillary forces do not significantly enhance adsorption in nanotubes over that between graphite planes [28].

2.3.2 *Ab initio* calculations

Some authors try to find a reaction mechanism by which hydrogen can chemisorb on carbon nanotubes or can penetrate the tube walls, so that the interior becomes available for hydrogen molecules. Since classical calculations exclude dissociation of a hydrogen molecule, different *ab initio* methods are exploited. At a pressure of 50 kbar and a temperature of 800 K, dissociation of hydrogen molecules in carbon nanotubes occurred in a density functional theory molecular dynamics simulation [44]. The adsorption potential was found to be positive (i.e. non-bonding). Lee et al. proposed a mechanism by which hydrogen atoms adsorb on the surface, dissociate, penetrate the tube wall and recombine in the interior of the tube [45].

2.4 In-depth experimental results

As calculations can not explain the excessive storage capacities reported, detailed measurements on the adsorption character, mechanisms, and sites for hydrogen on SWNT are vital in the debate on these results. Experiments on the adsorption potential, on the nature of the adsorption, on the adsorption sites and on the diffusion of hydrogen will be discussed below.

2.4.1   Adsorption potentials

The amount of adsorbed hydrogen as a function of hydrogen pressure approximately follows the Langmuir isotherm given by:

$$\theta = \frac{KP}{1 + KP},\tag{2.1}$$

where θ is the coverage of the adsorbent surface, K is the equilibrium constant and P is the pressure.

Introducing the rate of adsorption, Φ_a, which is proportional to the number of molecules hitting a vacant adsorption site we get:

$$\Phi_a \propto \frac{P}{\sqrt{T}}(1 - \theta),\tag{2.2}$$

where T is the temperature of the system and $(1 - \theta)$ is the fraction of unoccupied adsorption sites. We used the fact that the density of a gas is proportional to the pressure, whereas the average gas molecule velocity is proportional to $\sqrt{T}$. The rate of desorption, Φ_d, is proportional to a frequency, f, at which the surface atoms vibrate (this frequency is of the order of 10^{13} Hz) and the Boltzmann distribution factor, giving:

$$\Phi_d \propto f e^{-\frac{H_{ad}}{kT}}\theta,\tag{2.3}$$

where H_{ad} is the enthalpy of adsorption, k is the Boltzmann constant and θ is the fraction of occupied adsorption sites. Combining these two gives:

$$P = Cf\sqrt{T}e^{-\frac{H_{ad}}{kT}}\frac{\theta}{1 - \theta},\tag{2.4}$$

with C being a constant. When the volume of the gas phase is small, we can assume the fractional coverage, θ, to be constant in the temperature range investigated.

For several samples (SWNT and an activated carbon with a high specific surface area of 2200 m^2/g [39, 16]), the pressure as a function of the sample temperature during cooling is shown in figure 2.1. From the errors associated with the fitted values of the adsorption potentials, it was concluded that the adsorption potential is 580±60 K or 5±0.5 kJ mol^{-1}. The review article of Vidali et al. on potentials of physical adsorption gives a well depth of 51.7 meV for graphite, which equals 600 K or 5 kJ mol^{-1} [46], in agreement with these results. The value of Dillon et al. of 19.6 kJ mol^{-1} for hydrogen adsorbed onto single walled carbon nanotubes was not reproduced [18].

2.4.2   Evidence for physisorption

The question whether hydrogen adsorbs on nanotubes as a molecule or as an atom can be answered by measuring the change of the characteristics of the hydrogen molecule on adsorption. Particularly the rotational spectrum of adsorbed hydrogen molecules contains valuable information on the nature of the bond of the molecule and of the symmetry of the adsorption site.
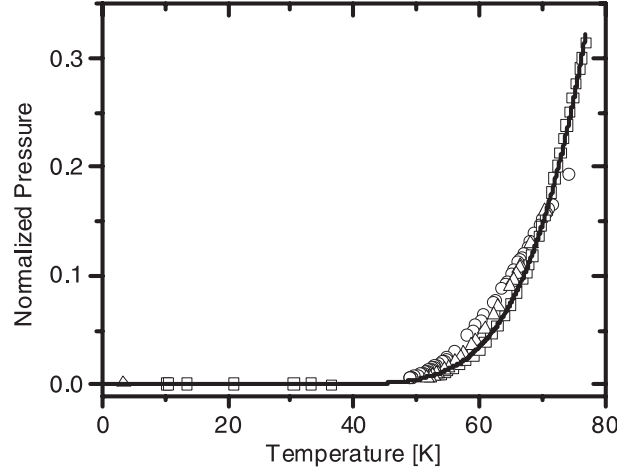
Figure 2.1: Temperature-pressure curves for SWNT (circles) and two activated carbons (triangles and squares). The line is a fit with the model $P = C'\sqrt{T}\mathrm{e}^{-H_{ad}/kT}$, giving an adsorption potential of 580±60 K.

Hydrogen as a probe in rotational spectroscopy

Due to its diatomic nature, hydrogen can rotate around two axes. The possible energies, E_J, of the rotation of the hydrogen molecule are quantized and are labelled by the rotational quantum number, J. For a hydrogen molecule that is free to rotate (this is in good approximation the case in solid hydrogen [47]) the energies of the rotational levels are given by $E_J = J(J+1)B$. The rotational constant, B, can be evaluated with the formula [47]:

$$B = \frac{\hbar^2}{m_p R^2} \, , \tag{2.5}$$

where $\hbar$ is Planck's constant divided by 2π, m_p is the mass of a proton and R is the distance between the protons. From the experimental value of B, 7.35 meV, [47] we can evaluate the difference between the two lowest rotational states ($J = 0$ and $J = 1$): 14.7 meV (or $\approx$170 K). Though it is trivial, we note that the rotational transition only occurs for molecular hydrogen, i.e. atomic hydrogen bonded to a carbon plane does not show this transition.

Hydrogen in rotational states with odd values of J is called ortho-hydrogen, whereas hydrogen in rotational states with even values of J is denoted para-hydrogen. At high temperatures (e.g. room temperature) the ratio of ortho- to para-hydrogen molecules is 3 to 1. At temperatures much lower than 170 K the lowest rotational state $J = 0$ is energetically favorable. The conversion from ortho- to para-hydrogen is promoted by the presence of paramagnetic catalysts or impurities in the samples. The neutron cross-sections of ortho and para hydrogen are rather different (ortho: 80 barn/molecule, para: 1.8 barn/molecule). Atomic hydrogen has a large cross

section (80 barn/atom). When it is known that all hydrogen has converted from the ortho to the para form, it can immediately be judged from the amount of scattering whether atomic hydrogen is present.

When a hydrogen molecule is adsorbed on a surface, the potential it feels is not isotropic nor circular symmetric because of the atomic nature of any surface, which hinders the rotation of the adsorbed hydrogen molecule. Spherical symmetry is broken, causing the triplet $J = 1$–level to split. Such splitting contains information on the symmetry of the site at which hydrogen is adsorbed. An example was observed by Fitzgerald et al. for hydrogen molecules in interstitial sites in solid C_{60} [48].

If the molecular hydrogen electron cloud is severely altered because it takes part in a bond with the surface, the distance between the protons increases due to reduced electronic screening (this H-H bond lengthening effect is also known as bond activation [49]). This leads to a smaller value of the rotational constant B (see equation 2.5). Such bond elongation effects were illustrated by Eckert and co-workers in experiments on different metal-complexes with a dihydrogen ligand. They found that the separation of the lowest two rotational levels of the dihydrogen ligand is smaller in complexes where the dihydrogen ligand molecule was more tightly bound, and the larger proton-proton bond lengths found in this way were confirmed by neutron diffraction [49].

Results

Brown et al. and Ren et al. measured the rotational spectrum with neutron scattering. Both find that the first rotational peak has a small shift with respect to the value for solid hydrogen, indicating that hydrogen molecules are weakly bound and that the hindering of the rotations is very small [50, 51]. Brown et al. estimate a binding energy of 6 kJ/mol, which is close to the literature value for the binding of hydrogen to graphite [46] and conclude that hydrogen is located on the surface of the tubes. Ren et al. found no peak broadening on increasing the temperature, indicating that hydrogen mobility is lower than hydrogen on graphite, and conclude that hydrogen is located in the interstitial sites, that is sites between the tubes in the nanotube bundles. We will discuss the location of hydrogen in a carbon nanotube sample in more detail below.

A comparison between adsorption on SWNT, activated carbons and graphitic nanofibers was published by us [39] (see also appendix B). The rotational spectra that were obtained are presented in Fig. 2.2. No sign of atomic hydrogen was found under the experimental conditions (77 K and 1 bar). Carbon nanofibers adsorb such a low amount, that experimental statistics are very poor. The spectra are not shifted with respect to the spectra of hydrogen in solid hydrogen: no significant bond activation or rotational hindering could be observed, which leads us to conclude that hydrogen is really only physically adsorbed with a low adsorption potential, a conclusion which supports the findings of an adsorption potential that is the same or similar to that for hydrogen on planar graphite [39].
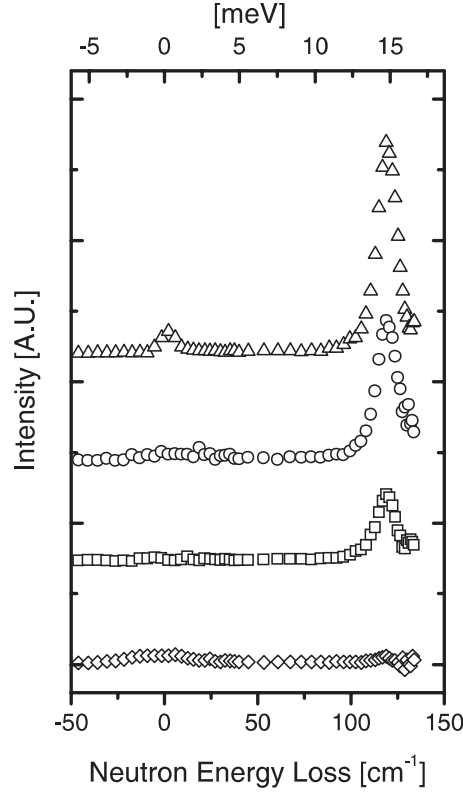
Figure 2.2: Neutron energy loss spectra of hydrogen adsorbed in activated carbon (triangles and squares), single walled carbon nanotubes (circles) and graphitic nanofibers (diamonds). The scattering of the sample without hydrogen has been subtracted.

The bond-lengthening effect also affects the vibrations of the hydrogen molecule, which are visible as Q-branches in Raman spectra. Williams et al. found no strong shifts of this branch, indicating that no significant bond lengthening occurs for hydrogen adsorbed on carbon nanotubes, and charge transfer is ruled out [40]. In contrast, for more strongly bound chemisorbed molecular hydrogen in e.g. zeolites strong shifts of the $J = 1$–level and the Raman Q-branch can be observed [52, 53].

2.4.3 Adsorption sites for hydrogen on SWNT bundles

Carbon nanotubes experience mutual interaction due the Van der Waals forces, comparable to the interaction between graphite planes, though nanotubes have a smaller contact area due to their curvature. As the interaction potential is negative, the lowest energy configuration is achieved when the contact area between tubes is maximal. The interaction area is maximized when tube arrange themselves to form bundles. Results by Mulder et al. show that carbon nanotubes are indeed arranged in bundles with thicknesses up to 50 nm and these are in turn arranged in domain with a size of about 10 μm [54]. The grooves between the tubes in the bundles may
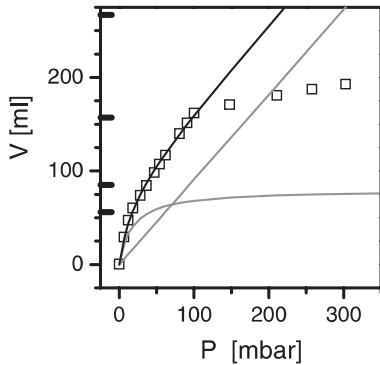
Figure 2.3: The pressure-composition isotherm for 0.85 g of SWNT at 60 K, which can be described by the sum of a Langmuir function and a straight line (grey lines).

form a site which is favorable for hydrogen adsorption: the adsorption potential is known to be about twice that of hydrogen on planar graphite, basically because the hydrogen molecule can touch two surfaces there [40, 55, 56, 57, 58]. In literature there has been a long discussion about the nature of the adsorption sites for gases in nanotube samples. Some authors suggested interstitial sites (between the tubes) or intertubular sites (inside the tubes) [51, 59, 60]. However adsorption of hydrogen is not possible in interstitial sites when all tubes have comparable diameters, because the intertubular voids are much to small (2.1 Å diameter) for hydrogen molecules (2.9 Å diameter) [39, 48]. Surface area measurements give a relative small number, indicating that the accessibility of the interstitial channels and the tube interiors is very limited [61]. Lately Bienfait and co-workers proposed another model introducing the idea of a bundle of nanotubes with different diameters [62]. Due to the differences in diameters of the tube misfits occur which provide voids large enough for interstitial molecules to adsorb in. It is an interesting question whether this effect is indeed visible in the specific surface area of such a sample, as well as in the spectra from the techniques described above (maybe using smaller molecules than hydrogen).

The isotherm we obtained (see figure 2.3) shows some remarkable features: it starts with a curved part which may be fit using a Langmuir isotherm, followed by a straight part ending in a sharp kink in the isotherm at the completion of the first monolayer.

Four different lines can be discriminated in figure 2.4 showing the high resolution results from the TOSCA spectrometer (ISIS, UK) on the rotational peak of hydrogen adsorbed on SWNT at different loadings [63] (see also appendix C). From these measurements it was inferred that hydrogen first occupies groove sites in the bundle, for which the pressure follows the Langmuir isotherm. The shape and the depth of the groove potential splits the first rotational level, giving line I and II. On further loading, line III shows that the surface of the bundles becomes covered. The width of this line starts narrow as the rotational hindering is small when the surface coverage is low, and increases when the layer becomes more dense. The straight line in the isotherm is associated with the filling of the surface layer. The straight character of the isotherm indicates that the number of possible confirmations
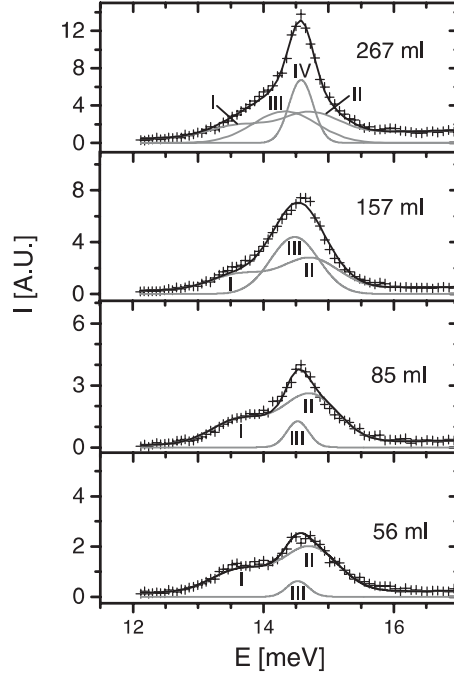
Figure 2.4: Inelastic neutron spectra for indicated hydrogen loadings in single walled carbon nanotubes. The fit (solid line) of the spectra (symbols) with spectral contributions as described in the text drawn separately (gray line). Gaussian lineshapes were used for the $J = 0$ to $J = 1$ rotational transition of hydrogen adsorbed on several surface sites in the nanostructured SWNT matrix. Lines I and II represent one type of adsorption site in the grooves, line III is the adsorption on the surface of the SWNT and line IV is the second layer.

$W = \exp(S/k)$ scales linearly with the coverage. The highest loading shows that hydrogen starts to occupy a second layer (line IV), which has a small interaction potential and a small rotational hindering (the line is resolution limited). From equivalent neutron scattering experiments, Georgiev et al. draw the conclusion that at least two different adsorption sites play a role [64].

The effective mass of an adsorbed molecule is determined by the potential energy landscape it feels. Steep and high potential walls result in a high effective mass. From an analysis of the difference between scattering in forward and backward directions, presented in figure 2.5, information on the effective mass of the hydrogen molecules can be obtained [65]. The molecules which adsorb in the grooves of the nanotube sample scatter isotropically (line I and II) as they are bound by hard walls (i.e. the nanotube surfaces) in two directions. The first molecules on the surface of the bundles (line III) scatter mainly forward, which indicates that they are restricted much less and are very free to move over the surface. When the surface layer becomes more dense, more neighbor interactions are present, which increases the effective mass. The last contribution (line IV), representing a partly occupied
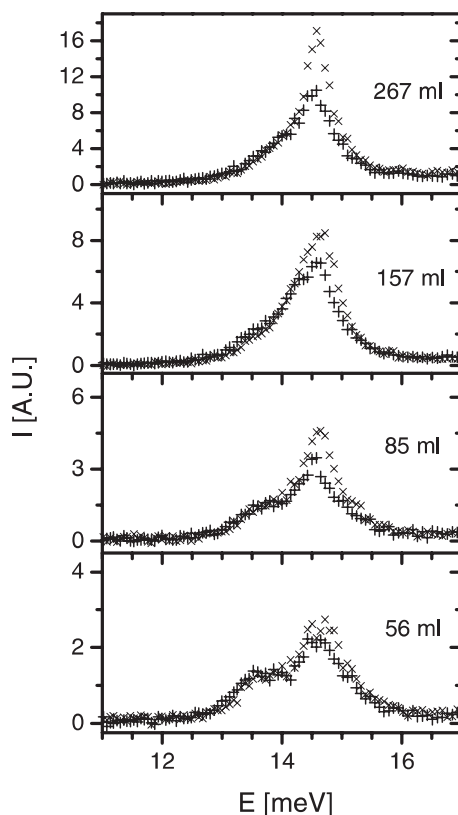
Figure 2.5: Neutron scattering spectra for hydrogen on SWNT that were shown in Fig. 2.4 decomposed in forward ($\times$) and backward ($+$) scattering contributions. The adsorbed hydrogen molecules scatter more isotropically when a site becomes filled.

second layer, is only visible in the forward scattering direction indicating that the potential walls are again very soft.

Quasi-elastic neutron scattering measurements reported by Narehood et al. show thermally activated diffusion on the surface of the nanotubes [66]. Their sample was loaded to 0.5 wt%, which means that at low temperatures only the grooves were filled. When the temperature was increased, the signal from moving hydrogen molecules appeared as they were activated from the groove sites to the surface. These results are consistent with the calculation that predict that the adsorption potential in a groove site is about twice that in the surface sites [55].

2.5 Zeolites, Metal Organic Frameworks and Hydrogen Clathrates

There exist other materials with a high surface area that are potentially interesting for hydrogen storage applications. The class of materials with a very open regular

structure known as zeolites —crystalline aluminosilicates— are mostly used in chemical processing, but also store hydrogen. Zeolites draw particularly interest as they combine a high surface area with a relatively high adsorption enthalpy due to the ionic nature of the surface. They store hydrogen in reasonable amounts, provided that the hydrogen molecule can enter the zeolite, which is not the case for some types of zeolite. The interaction between zeolites and a hydrogen molecule is about 10-15 kJ/mole H_2, much larger than that between hydrogen and graphite due to the presence of ionic centers [67]. Low temperature operation, however, is still needed in order to achieve practical storage pressures. As the building blocks of zeolites, SiO_4 and AlO_4 tetrahedra, are quite heavy, the weight capacity is always low (see the values published by Nijkamp et al. [16]). We measured the zeolite known as NaY, which has a structure that is large enough for hydrogen molecules to enter, and found a storage capacity of about 0.1 wt% at 77 K and 1 bar H_2 pressure. Since zeolites are used world wide in industry, they may play a role for hydrogen storage in stationary applications. For storage of hydrogen onboard a vehicle, the capacity is too low at the present moment.

Metal organic framework (MOF) materials with an exceptional high surface area were reported to exhibit a high adsorption capacity (4.5 wt% at 78 K and 1 bar) [68], though more recently lower values (in the range 1-2 wt% at 77 K and 1 bar) were reported by the same group for slightly different high surface area MOFs [69]. Metal organic frameworks are crystalline structures of metal-oxide corner groups linked together by aromatic bridges (small graphitic parts). The material used for the first hydrogen storage experiments, MOF5, has a cubic structure with a lattice parameter of 25.85 Å. Because the structure has only atoms on the edges and in the corners, a large void is present which can be occupied by guest molecules such as hydrogen. The interaction potential is estimated to vary between 5 kJ/mole for graphitic parts and 10-15 kJ/mole for the ionic centers. Eckert et al. report inelastic neutron scattering experiments showing that several adsorption sites exist in this material [68]. Since an activated carbon with a surface area of 2200 m^2/g stores about 2 wt% under these conditions [16], the hydrogen storage capacities reported in the second paper are more plausible as the surface areas and the interaction potentials of this activated carbon and the MOFs are comparable.

Under high pressure water and gas molecules can form solids in which the water molecules form cages filled with and stabilized by the gas molecules, known as clathrate hydrates. For hydrogen storage these materials were always considered as highly impractical due to the extremely high equilibrium pressure (around 2000 bar) at ambient temperatures [70]. Recently Florusse et al. was able to show that the hydrogen hydrate can be stabilized at room temperature about 100 bar when a small amount of the promotor tetrahydrofuran (THF) is added [71]. This pressure is obviously more practical, though still relatively high. The clathrate with THF promotor that is formed is reported to be of the sII-type with a structure that is equivalent to that found by Mao et al. for the pure hydrogen hydrate [70]. Florusse et al. find evidence that the small cages in the sII structure are filled by more than

one hydrogen molecule, which makes that approximately 5 wt% may be stored in practice [71]. These hydrogen hydrates may be produced in stationary plants, after which hydrogen can be loaded in the hydrate form in vehicles. The hydrogen can easily be released by decomposition of the hydrate when the pressure is lowered or the temperature is increased.

2.6   Conclusions

We started this chapter by stating that the adsorption enthalpy of hydrogen on carbon materials is just right for hydrogen storage applications according to the demarcation given in section 1.4. We have shown that although hydrogen adsorbed on carbon nanotubes has some remarkable features, most likely due to the curved nature of the surface, carbon nanotubes are not adsorbing better, and with respect to specific surface area even worse than activated charcoals. The fact that we need to cool hydrogen physisorption systems is a major drawback of these materials. Further, we need to realize that all physisorption materials suffer from a slow capacity degradation when the hydrogen that is loaded contains some contaminants as all other gases except some noble gases have a stronger adsorption interaction.

The use of physisorption systems at room temperature is also an option when one applies pressures of the order of 100 bar, either in the form of gas hydrates, in metal organic frameworks or in ordinary charcoal. However, the social acceptance of such relatively high pressure systems is likely to be very low, given the fact that the use of liquified petroleum gas (LPG), which works with pressures around 10 bar, is already very controversial because of projected explosion risks: in many countries LPG-cars are not allowed in parking garages and in the Netherlands a workgroup recently suggested to stop the distribution of LPG completely. Another questions is whether a storage tank filled with a high-pressure (100 bar) adsorbent will be so much lighter that drawbacks such as the cost of the adsorbent and the capacity loss with time are compensated. We conclude that hydrogen storage by physisorption on high surface area materials is a valuable option from a fundamental viewpoint. From a practical view-point, however, economic and safety considerations might hamper its widespread use in the near future.

Chapter 3

Kinetics of hydrogen storage in magnesium

Hydrogen often behaves as an element of the halogen group like fluorine and chlorine. In this role, it forms hydrocarbons like methane, gasoline and all sorts of plastics. In the periodic system, however, Mendelejev positioned it above the alkali metals on the basis of its mass and it stayed there as it has a single electron in the s–shell like all elements in the first row. When hydrogen behaves like a metal, it forms compounds with metals like $LaNi_5$, FeTi, Pd and others [8]. Generally the Miedema model applies, which says that the more stable an intermetallic compound is, the less stable its hydride is and vice versa [72]. These intermetallics form initially a solid solution α phase when they are hydrided. The lattice of the α–phase expands as each hydrogen atom adds an effective volume of 2–3 Å^3 [73]. The α–phase is characterized by a relatively low hydrogen concentration, so that the interactions between hydrogen atoms are weak and the mobility is generally very high. Mutual interactions between dissolved hydrogen atoms cause a 'gas–liquid' α–α' transition when the hydrogen concentration increases [74]. The two phases basically differ only by the lattice parameter and the hydrogen occupation. The 'gas–liquid' analogy comes especially to the fore in the existence of a critical point in the phase diagram, above which no phase transition occurs.

When hydrogen shows more halogen-like character, it forms complex metal hydrides such as $LiAlH_4$, $MgAlH_4$ and MgH_2. For most of these compounds a version where hydrogen is substituted by chlorine or fluorine is known. On hydriding, these compounds undergo a phase transition which cannot be described by the analogy of a gas–liquid transition: the typical critical point is absent. The resulting compounds are not metallic, but ionic or covalent and most of them appear as white solids in their pure form. The alanates (i.e. the compounds of the form $MAlH_4$, with M a metal) are not easily reversible with respect to their hydrogen content, though the addition of titanium particles improves the reversibility in the case of $NaAlH_4$ [75].

In this chapter we will describe our investigations on the limitations of the kinetics of the reaction of hydrogen and magnesium. First we report the influence of ball

milling, then we analyze the diffusion of hydrogen through magnesium metal and finally show why the heat of the hydride formation should be taken into account as well. We start reviewing the literature on the limiting factors for hydrogen sorption kinetics in magnesium.

3.1 Magnesium as a hydrogen storage material

Magnesium metal may be hydrided with hydrogen gas to form magnesium dihydride. It is one of the most promising hydrogen storage materials, as it stores about 7 wt% of hydrogen reversibly. Magnesium exhibits very slow hydriding and dehydriding processes even for laboratory-size samples. This and the high adsorption enthalpy (i.e. low equilibrium pressures at ambient temperatures) makes that magnesium requires a high operation temperature of about 350 degrees Celsius [76].

3.1.1 Limiting factors for hydrogen sorption kinetics

An important parameter of hydrogen storage systems, especially for mobile applications, is the speed of hydriding. The goal is to store a few kg of hydrogen in a few minutes (when hydrogen is loaded in the form of a hydride the absorption rate can be smaller). The hydriding process involves the following steps: gas transport to the surface of the particles, surface adsorption and dissociation, transition from surface to bulk, diffusion through the material and finally nucleation and growth [77, 78]. Usually these processes are relatively fast for practical-size batches, so that thermal conductivity and gas permeability are the limiting factors in applications [79].

Several authors conclude that the shell model applies (see figure 3.7). In this model hydride formation starts at the surface of a magnesium metal particle. When more than three of these hydride grains nucleate at the surface, they will eventually merge and form a gas-tight, closed shell (due to the low hydrogen mobility) of magnesium hydride around the remaining metal core [80, 81, 82, 83, 84, 85]. Vigeholm et al. found that the diffusion of hydrogen is not through the magnesium hydride phase, but rather along the hydride-metal interface [86, 80]. Experimentally it has been found that for particles larger than about 75 μm, the hydriding progress becomes very slow when about 30% of the sample has converted to MgH$_2$ and that at the end the particle still contains an unreacted magnesium metal core [77, 78]. The isolating effect of a hydride layer near the interface has also been observed in the case of thin magnesium layers [87]. On dehydriding, the magnesium hydride starts to convert to magnesium metal at the surface while the size of the magnesium hydride phase decreases. The hydriding and dehydriding processes may therefore be intrinsically asymmetric [83]. The importance of the dissociation process has been stressed by Gerasimov et al. [88]. They also found that cracking of the magnesium oxide layer occurs during a heat treatment, which makes the magnesium metal surface accessible for hydrogen molecules [89]. Mintz et al. showed that the diffusion process may be relevant [90]. Liang et al. found that initially nucleation

and growth and in a later stage the long range hydrogen diffusion is most important [91]. Mechanical grinding and the addition of alloying elements such as indium [90] or cerium [92] to improve diffusion speeds has been exploited already more than 20 years ago [77]. Another option is the addition of a metallic or metal-oxide catalyst to the surface of the magnesium particle [80, 93, 94].

3.1.2   Ball milling and catalysts

Recently, high energy ball milling was applied to magnesium hydride which decreases the particle size and induces stresses and defects in the structure [76, 95, 96]. The ball milling treatment increases the hydriding kinetics by approximately a factor of 10 and the addition of vanadium as a catalyst may increase the kinetics by another order of magnitude. As ball milling breaks down the particles, a higher surface area is present for hydrogen to enter the particles. Other effects may be that hydrogen diffusion is speeded by the introduction of defect zones or that defects form multiple nucleation centers for MgH_2. In order to be able to point the most relevant factor, it is crucial to have a better understanding of the changes made by the ball milling treatment.

3.2   Structural changes in ball milled magnesium hydride

Huot and co-workers investigated ball milled magnesium in detail using X-ray diffraction [96]. They found that a ball milling treatment of β–MgH_2 forms the high-pressure γ–MgH_2–phase [97] to a concentration of 18%. Cycling the hydrogen content removes this phase again. The average particle size for such ball milled samples was determined to be 12 nm. The background of the diffraction patterns obtained after ball milling is significantly increased, which means that a large part of the scattering is not found in the Bragg peaks any more, possibly due to very small crystallites, very high defect concentrations, strongly distorted structures or amorphous parts in the crystallites. The fact that diffraction relies on long-range ordering is clearly a drawback when one wants to study materials which are heavily deformed (for instance by ball milling). Vibrational spectroscopy may be used in such situations because very small structural units already produce a typical spectrum [98].

3.2.1   Vibrational spectroscopy as a sub-nanometer probe

Vibrations are governed by forces between atoms that have in general a range less than 1 nm. Thus, by probing vibrations we effectively probe the material on a nanometer scale. A drawback is that we need *a priori* knowledge of the structure and a reliable method to calculate the vibrational spectrum from the structural model. In the case of magnesium hydride structural models of the β– and γ–MgH_2–phase
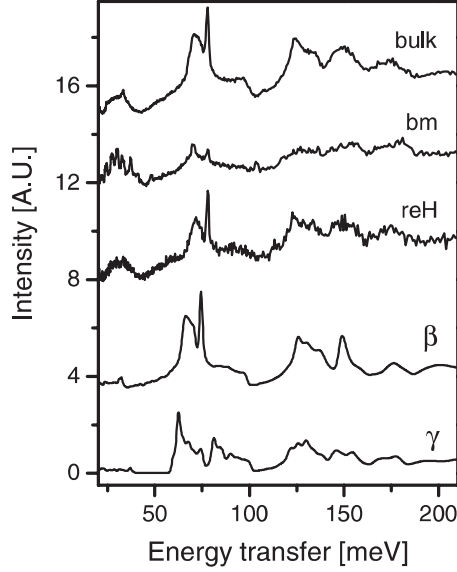
Figure 3.1: Vibrational spectra (from top to bottom) of bulk MgH_2, ball milled MgH_2 and for MgH_2 that was ball milled and rehydrided. The calculations for β– and γ–MgH_2 are also shown.

are available and calculations using Density Functional Theory predict vibrational frequencies remarkably well [99].

We measured the vibrational spectrum of bulk (i.e. unmilled) magnesium hydride on the inelastic neutron scattering spectrometer TOSCA (see also appendix D, [100]). The vibrational spectrum was simulated using Density Functional Theory calculations with the VASP package [101]. The momentum transfers at which TOSCA measures vary with the energy transfer. It is not sufficient to simulate only the Γ-point, the point of zero momentum transfer. In order to correctly describe the measured spectrum we derived all force constants, after which a full phonon spectrum was calculated using the program PHONON [102]. Then a cut from the calculated spectrum was taken using a Monte Carlo method to simulate the TOSCA spectrum.

Figure 3.1 shows our results for bulk, ball milled and rehydrided magnesium hydride, together with the calculations for the β– and γ–MgH_2 phases (see also appendix E, [103]). The resemblance is remarkable, particularly if we have in mind that the only input for this calculation was the structure of MgH_2. We observe that the spectrum of ball milled magnesium hydride is very much rounded off with respect to the spectrum for the bulk material. On dehydriding and subsequent rehydriding, we get the bulk spectrum, though X-ray diffraction showed that the particle size stays small. We performed simulations of the spectrum of β– and γ–MgH_2 that was deformed in several ways. The simulated spectra show a dependence of the peak positions on the pressure and deformation in the structure. A distribution of stresses produces a spectrum which is rounded off. In Figure 3.2a we approximated
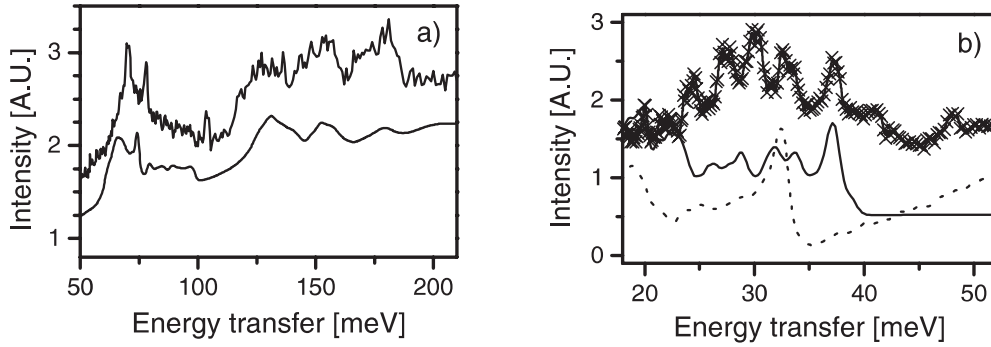
Figure 3.2: a) The vibrational spectrum of ball milled magnesium hydride (top) with 'fit' (bottom), which consists of 75% of the calculated and averaged spectrum of β-MgH$_2$ plus 25% of γ-MgH$_2$ and a background function. b) The measured vibrational spectrum for ball milled magnesium hydride (top line with crosses) and the calculated spectra for γ MgH2 (bottom solid line) and β MgH$_2$ (bottom dotted line). The calculated spectra are multiplied by 10 with respect to the scale used in a). The ratio between β and γ-phase in the ball milled sample samples might be as high as 50% and the γ–phase appears to be so distorted that it contributes mainly to the background at the higher energy part shown in a).

the experimental spectrum of ball milled MgH$_2$ by taking 75% of the calculated and averaged spectrum of β–MgH$_2$ plus 25% of γ–MgH$_2$ plus a background function. However, as becomes clear from Figure 3.2b, the actual fraction of the γ phase is much higher than 25% and a large portion of the background in the vibrational spectrum has to be attributed to γ–phase particles. Apparently the distortions of the γ–phase are that large that the peaks at higher energies are completely smeared and contribute to the background. We can explain the fact that we only see this γ–phase in the lower energy part of the spectrum by assuming that the peak shifts due to the deformations are proportional to the position of the peak, whereas the peak widths are comparable throughout the spectrum.

The initial dehydriding kinetics of a ball milled sample is very fast [96]. After a few cycles the hydriding kinetics become constant, but much faster than those for the bulk material. We found that the γ–phase disappears on cycling and that the structure that remains is very clean: no signs of stresses have been found for the rehydrided material: the defect structure that is introduced by the ball milling method, is annealed out when the hydrogen content of the material is cycled. As the hydriding speed remains high, we conclude that defects and lattice deformations do not play an important role in the observed increase in speed.

3.3 Diffusion of hydrogen through magnesium

Fick's first law states $J = -D\,\mathrm{d}c/\mathrm{d}x$, connecting the flux, J, the diffusion constant, D, and the concentration gradient, $\mathrm{d}c/\mathrm{d}x$. The solubility of hydrogen in magnesium
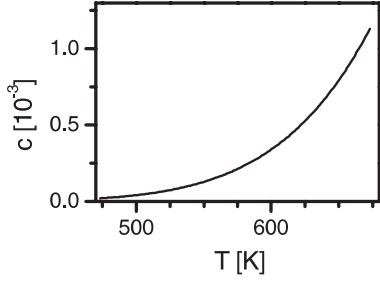
Figure 3.3: The hydrogen concentration c in magnesium metal in equilibrium with hydrogen gas and magnesium hydride as a function of temperature.

metal, c, is an important parameter for hydrogen sorption kinetics. From the Gibbs free energies of the H_2 gas phase, the MgH_c solid solution phase and the Mg metal phase, we obtain the concentration, c, in the Mg α–phase from the equation:

$$2\left[G_{Mg:H}^{0,cph}(T) - G_{Mg}^{0,cph}(T)\right] + RT[\ln(2c) - \ln(1 - 2c)] = 0.5 G_{H_2}^{gas} \qquad (3.1)$$

using the same symbols as Zeng et al. [104]. In the same way the equilibrium pressure of hydrogen gas and magnesium hydride can be found from

$$G_\beta^0(T) = G_M^{0,cph}g(T) + G_{H_2}^{gas}(T, P). \qquad (3.2)$$

The hydrogen concentration, c, in magnesium metal in equilibrium with hydrogen gas and magnesium hydride is shown in figure 3.3. The calculated points can be approximated by the function $c = 20 \, exp(-54800/RT)$. The equilibrium pressure as function of the temperature scales with $\exp(-74500/RT)$.

Renner et al. determined a diffusion coefficient of hydrogen through magnesium metal of $D = 3.8 \cdot 10^{-6} \exp(-40000/RT)$ [92]. From permeation experiments, a diffusion coefficient of $D = 1.54 \cdot 10^{-6} \exp(-24100/RT)$ was found [105]. The energy barrier between 2a sites along the c-axis was found to be 155 meV with density functional theory calculations corresponding to a diffusion coefficient of $D = 1.2 \cdot 10^{-9} \exp(-15000/RT)$ m^2/s [106] when we assume an attempt frequency of 10^{13} Hz.

Magnesium metal crystallizes in a hexagonal closed packed structure (space group $P6_3/mmc$). In this structure octahedrons and tetrahedrons with magnesium atoms on the corners are present as is shown in figure 3.4. For every Mg atom (Wyckoff site 2c), there is one octahedron site (Wyckoff site 2a) and two sites with tetrahedral coordination (Wyckoff site 4f). Two tetrahedron sites are separated by 1.32 Å via a window of three magnesium atoms. Table 3.1 shows all nearest neighbor distances between octahedrons and tetrahedrons.
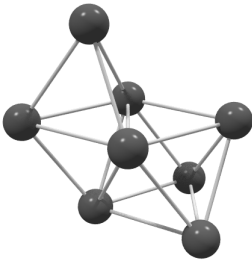
Figure 3.4: The crystal structure of magnesium metal showing the tetraedron and octaedron sites for hydrogen.

Table 3.1: The number and the length of the paths between sites in Mg metal. The coordination number of the window is always 3, the paths via a Mg-Mg line are left out.

initial site	target site	number	length [Å]
octahedron	octahedron	2	2.64
octahedron	tetrahedron	6	1.99
tetrahedron	tetrahedron	1	1.32
tetrahedron	octahedron	3	1.99

3.3.1 Molecular dynamics simulations

We applied *ab initio* molecular dynamics simulations using VASP [101] on the magnesium metal-hydrogen system so as to investigate the diffusion of hydrogen atoms through the metal matrix (see appendix F, [107]). We use a supercell of $3 \times 3 \times 2$ unit cells of magnesium metal and added one hydrogen atom. The supercell lattice parameters are a,b=9.750 Å and c=10.552 Å and it contains 36 magnesium atoms and 1 hydrogen atom. A gamma-centered k-point grid of $2 \times 2 \times 2$ points and a value for the gaussian smearing of 0.2 made the entropy contribution to the total energy smaller than 1 mev/atom [108].

Molecular dynamics simulations were performed at 673, 623, 573, 523 and 473 K with 20000 time steps of 1 fs. The structure was thermalized for a few ps before the simulation was started. The trajectories of the hydrogen atom are plotted in figure 3.5. It shows that the tetrahedron sites come in pairs (seen as the 8-shape in the trajectories). These pair sites are separated by a distance of 1.32 Å only and appear to have a relative low energy barrier between them. The octahedron site is much less occupied. At 673 K, the hydrogen atom stays about 75% of the time in tetrahedron sites and 16% of the time in octahedron sites, while for the rest of the time, no site
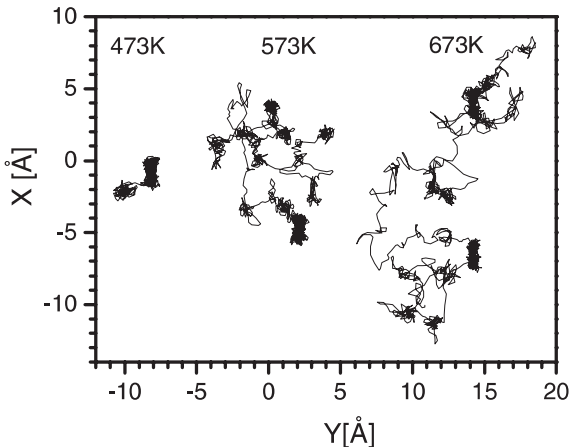
Figure 3.5: The trajectories of a hydrogen atom in a magnesium metal lattice (36 atoms) at different temperatures. The trajectory is drawn between points that are separated by 10 fs simulation time. A total number of 2000 points are drawn, which equals a simulation time of 20 ps.

can be assigned. The mean square amplitude equals 0.04 Å^2 for the tetrahedron site and is of the order of 0.1 Å^2 for the octahedron site. Using the equation in appendix A.2.6, we inferred the diffusion coefficients for these temperatures. The diffusion coefficients that we found were fitted yielding the following approximation: $D = 2 \cdot 10^{-2} \exp(-40640/RT)$. We find an activation barrier which is much higher than published by Renner et al. and Nishimura et al., although the prefactor is larger in our case, which makes that our value agrees within an order of magnitude with those of Nishimura et al. [105] in the temperature range 500–700 K, whereas the values of Renner and Grabke are consistently lower [92]. The fact that the jumps of hydrogen are correlated (see figure 3.5) makes the diffusion coefficient that we derived from the energy barrier published by Jacobson et al. much to low. We plot these results on a log scale in figure 3.6.
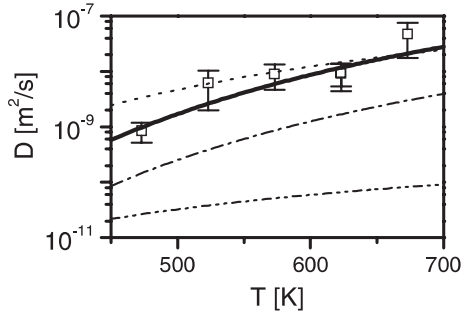
Figure 3.6: Hydrogen diffusion coefficients in magnesium metal from calculations (solid line our calculations, dash-dot-dotted line barrier calculations of Jacobson et al. [106]) and experiments (dotted line from Nishimura et al. [105] and dash-dotted line from Renner and Grabke [92]).

3.4   Heat effects

As we discussed above, the evidence for the shell model is quite convincing. Discussions in literature, however, do not handle about heat effects on the scale of a single grain. Below we show why heat effects are very important for hydriding (and dehydriding) properties of a material. The increase in temperature when a small fraction of a particle transforms into a hydride, makes the driving force for further hydriding zero.

We pose the following, realistic, situation: a bed of particles is brought at a temperature of 673 K and a pressure $P_a = 35$ bar of twice the equilibrium pressure, P_{eq}, is applied. On the application of the pressure, the magnesium metal α-phase will first start to saturate with hydrogen atoms. After a certain time, the hydride phase will nucleate somewhere in the particle. This hydride phase will grow as there exists a driving from the overpressure. Magnesium hydride is an insulator and the heat that is generated on the hydride-metal boundary will distribute over the remaining magnesium metal (α-phase). Due to the temperature rise that then occurs, the equilibrium pressure of the particle rises and the chance of new nucleation elsewhere in the particle decreases rapidly.

Consider a particle containing N_p mol magnesium atoms of which a fraction f has been converted to magnesium hydride. The heat that is released by the

a) Shell model   b) Sink model
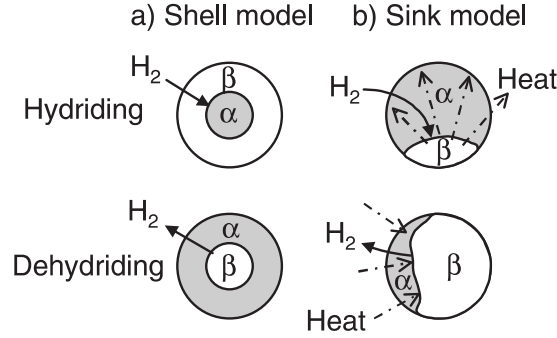
Figure 3.7: Two adsorption models, on the left the shell model that applies to large magnesium particles where so much nucleations occur that a closed hydride layer forms that hinders further hydriding at a certain stage. On the right the sink model that applies to small particles (smaller than 75 μm) wherein only one hydride nucleation occurs due to the heat which neutralized the other nucleation center. The nucleus acts as a sink which removes the hydrogen atoms before they can initiate a new nucleation elsewhere.

conversion to the hydride phase is $H_f = f H_{MgH_2} N_p$, where H_{MgH_2} is the formation enthalpy of magnesium hydride, 74.5 kJ/mol. The heat will increase the temperature of the magnesium particle by $\Delta T = H_f/(M_{Mg} C_{Mg} N_p)$, using the molar mass of magnesium, $M_{Mg} = 0.0243$ kg/mol, and the heat capacity, $C_{Mg} = 1026$ J/(kg K). The equilibrium pressure becomes equal to the applied pressure (which we assumed to be two times the equilibrium pressure initially) when the temperature of the magnesium particle increases by about $\Delta T = 35$ K (for temperatures around 673 K, for lower temperatures, ΔT is lower). Now that we know all parameters, we can calculate $f = \Delta T M_{Mg} C_{Mg}/H_{MgH_2} = 1.2\%$. We conclude that when just 1.2% of a Mg particle transforms to MgH$_2$ the heat that is released makes the driving force zero due to the temperature-rise of the particle. Only when the heat has been dissipated, a driving force exists again and more hydrogen may adsorb. This shows that heat transfer is not only important for engineering sized batches, but also for the microscopic nucleation behavior.

The characteristic time associated with the transport of the heat that is generated through a magnesium particle may be evaluated from the following model: an average temperature difference of $\frac{1}{2}\Delta T$ exists over a cube with dimension $d \times d \times d$. The time needed to transport enough heat via this cube to increase the temperature of an identical cube by ΔT may be expressed as: $t = 2\rho_{Mg} C_{Mg} d^2/G$, where G is the heat conductivity coefficient $G = 156$ W/(m K) and $\rho_{Mg} = 1738$ kg/m^3 is the density of magnesium. For $d = 10^{-6}$ m, $t = 2.2 \cdot 10^{-8}$ s. We compare this with the nucleation rate, which is commonly expressed as:

$$\dot{N} = N_c \frac{kT}{h} e^{-\frac{\Delta G}{kT}}, \qquad (3.3)$$

where ΔG is the activation energy of nucleation, which may be as high as 85 kJ/mol

[91]. The number of nucleation centers in the particle, N_c, is assumed to be of the order of 10. We find for the average time between two nucleations $t = 2.8 \cdot 10^{-8}$ s, which is comparable to the heat transportation time we determined above. However, if we take smaller particles, i.e. with a characteristic dimension $d = 20$ nm, the heat transportation time becomes much shorter, $t = 4.6 \cdot 10^{-12}$ s, whereas the average nucleation time may increase as it is likely that there are less nucleation centers in a small particle.

We conclude that heat effects become more important when particles become smaller. The characteristic particle size where heat effects make that only one nucleation center is allowed to grow is of the order of 1 μm. This is in agreement with the observation of Vigeholm et al. [86] that particle exceeding a size of about 75 μm did not react completely. For particles of this size, the particle is that big that the chance is high that more than three hydride phases nucleate, which forms a closed shell when they grow spherically. For sub micron particles it is likely to have only one nucleation center and the formation of a MgH$_2$ shell becomes unlikely.

3.5   Nb catalyst phases during hydrogen cycling of Mg

Above we discussed the effect of ball milling on the hydriding properties of Mg particles. We concluded that the main reason that the kinetics improve is that the particle size becomes smaller. Apart from the ball milling treatment, catalysts are frequently added to a Mg sample, since this increases the sorption kinetics significantly as well. Huot et al. have shown that especially V and Nb are very good catalysts for magnesium when the catalyst and magnesium hydride are ball milled together [109, 94]. Several attempts have been made to reveal how these catalysts work. Pelletier et al. used *in situ* X-ray scattering to follow the phases that exist during desorption of hydrogen from ball milled MgNb$_{0.05}$H$_2$ [94]. They found a Nb phase that acts as a gateway for hydrogen during desorption. Yavari et al. were able to point out that this gateway phase is actually a bcc solid solution NbH phase [110]. We performed neutron scattering experiments on the same system (MgNb$_{0.05}$D$_x$), though with deuterium instead of hydrogen (see appendix G). We worked at a constant temperature of 320 degrees Celsius first absorbing and then desorbing with a constant deuterium flow and found the solid solution phase with composition NbD$_x$ in all spectra. In our case the amount of deuterium in, and the lattice parameter of NbD$_x$ varied with the deuterium pressure that existed in the sample during deuterium cycling. Only when all MgD$_2$ was converted into Mg, the pressure became low enough for NbD to desorb. During the experiments of Pelletier et al. and Yavari et al., the samples were first evacuated to low pressures. The temperature was then ramped while diffraction spectra were obtained. During this procedure the sample was still evacuated. Using such a procedure, large pressure gradients exists between the pressure locally in the sample and the pressure in the pump as the particle bed is
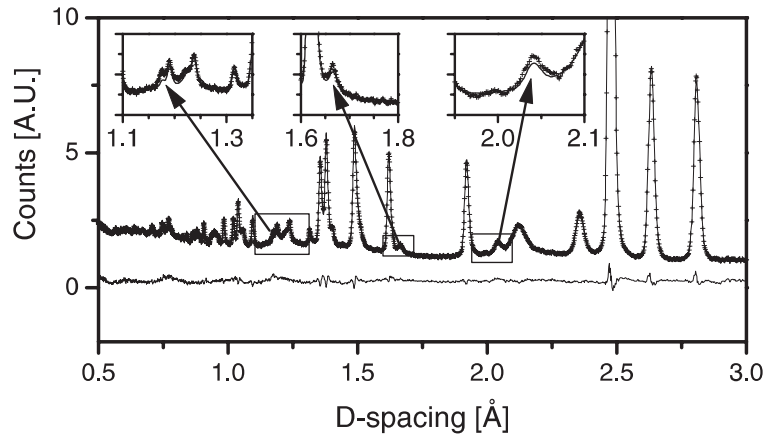
Figure 3.8: Rietveldt refinement of the fully dehydrided sample. Two unique peaks that belong to the perovskite phase are indicated by the arrows in the insets.

a considerable resistance to the hydrogen flow. The pressure in the sample container is a measure for the rate of hydrogen desorption. Since in these experiments the desorption takes place on the scale of seconds, high desorption rates and thus relatively high local pressures are found, which is visible in the hydrogen content of Nb. In our case, the deuterium was cycled under conditions much closer to equilibrium and no gateway phase was found.

To our surprise there appears on the first instant of D absorption a D-depleted $MgD_{<2}$ phase. This may represent the first nucleation stage of MgD_2 (and MgH_2). This phase could have enhanced proton mobilities since the vacancies in this initial phase facilitate hydrogen diffusion through the hydride. Most interestingly, however, is our finding of an extra phase in our spectra. Figure 3.8 emphasizes the peaks of these phase that are observable by eye in the spectrum of the fully dehydrided sample. We could uniquely identify peaks at d-spacings equal to 2.035 Å 1.661 Å and 1.175 Å which points towards a cubic phase with a lattice parameter of 4.07 Å. We propose a perovskite structure with the formula $Nb(Mg_{0.333}Nb_{0.667})O_3$. This phase could consistently be fitted in all spectra that were taken during desorption. Since some perovskites are proton conductors and/or catalytically active [111], we speculate that this new phase may be catalytically active here too. It is not unlikely that this phase, which can be formed from MgO that is already present in the sample and from Nb during ball milling, plays an important role in the transport of hydrogen through the MgO barrier, since it may replace the MgO layer on the surface of Mg particles.

3.6   Conclusions

Magnesium has been taken as a model system to study the limitations for hydriding kinetics of hydrogen storage materials. We have shown that making the hydrogen

storage materials nanostructured improves the hydrogen storage kinetics due to the fact that the accessible specific surface area becomes much larger, because diffusion paths become shorter and because only one nucleation center is activated. For magnesium, and most likely for all metallic hydrogen storage systems, the diffusion of hydrogen atoms through the metal is not a serious barrier. The diffusion of hydrogen through the hydrogen-filled hydride phase, where the mobility is much lower, can cause a blocking effect when large particles are used. The discussion on the heat effects given above does apply for every hydrogen storage material where hydrogen is stored interstitially as they all have comparable absorption enthalpies. Materials which are thought to be useful for *heat* storage by hydrogen cycling, are less useful for *hydrogen* storage since large amounts of heat need to be dissipated and supplied again on hydrogen extraction. A hydrogen depleted $MgH_{<2}$ phase was observed just at the beginning (ending) of hydrogen absorption (desorption). This phase should have enhanced hydrogen transport. Finally the in-situ study on Nb-catalyzed Mg showed an interesting new Nb-Mg-O perovskite phase that may be relevant for the catalytic activity of niobium in magnesium. We conclude that Mg based storage materials would be promising in combination with high temperature fuel cells.

Chapter 4

Concluding remarks

In the first chapter we saw that practical storage efficiencies limit the sorption enthalpies of hydrogen storage systems with respect to the temperature of operation. High surface area materials such as activated carbon and single walled carbon nanotubes need to function at low temperatures, which brings drawbacks of heat leakage and heat from adsorption that has to be brought to high temperatures.

Further, we need to realize that all cooled physisorption materials suffer from a slow capacity degradation when hydrogen contains some contaminants. This is particularly relevant because all other gases except some noble gases have a stronger adsorption interaction. We conclude that the high surface area carbon materials are expected to play no important role for hydrogen storage in the future because the hydrogen adsorption interaction is too low. No reports are available to date of the adsorption energies for hydrogen in MOFs, but it may be deduced from the low operation temperature that it will be low for most of the internal surface. Zeolites remain relatively heavy and are therefore not particularly promising.

Materials that are synthesized in a plant, such as hydrogen clathrates and hydrogen borates, which are subsequently supplied to vehicles may be investigated further. Issues to be addressed are whether they can be stabilized at close to ambient temperatures and safe pressures and whether they can be reprocessed relatively easily after the hydrogen is extracted.

High absorption enthalpy systems such as magnesium do not reach the minimum storage efficiency that is needed for practical storage systems because they need high temperatures for practical desorption pressures and for sufficient sorption kinetics. However, when these materials can be combined with an intermediate temperature fuel cell, several advantages exist: 1) a cheap and light storage material is available, 2) the storage efficiency is no issue as the waste heat from the fuel cell can be used to desorb hydrogen from the system and 3) at high temperatures the catalysts in the fuel cell and the storage system are less sensitive to poisoning, so that less pure feed gases can be used.

Summary

Towards a hydrogen-driven society?

Calculations and neutron scattering on potential hydrogen storage materials

by H. G. Schimmel

Introduction

Sustainable development means that alternatives have to be found for the use of fossil fuels to cover our energy needs without disturbance of the balance in the environment. As carbon dioxide is thought to cause major climate changes in the future, the sustainable production of energy nowadays concentrates on carbon dioxide-neutral processes. A sustainable means of transport in particular, implicates that another choice than fossil fuels for the transport of energy is necessary. Hydrogen is a perfect energy carrier in this context as it emits only water vapor when used in a fuel cell and a limited amount of undesirable by-products when used in traditional internal combustion engines. The transportation of hydrogen, however, is a major challenge. Our comparison between internal combustion engines and electric engines with a battery pack shows that the storage of energy onboard vehicles is a long standing problem.

Hydrogen storage

Hydrogen is a very light and volatile gas, which makes that high pressures, low temperatures or a sorption material are needed. From the targets for future hydrogen storage systems of the department of energy of the USA, especially the minimum efficiency figures, limiting conditions for the sorption enthalpy as a function of operation temperature are derived. The storage efficiency of high absorption enthalpy materials that operate at high temperatures, such as Mg, is shown to be lower than 90% for stand-alone applications. However, these restrictions do not apply when intermediate temperature fuel cells (operation temperatures above 200 degrees Celsius) can be used since they provide waste heat for hydrogen desorption from the high-enthalpy materials.

This thesis is about the characterization of two classes of hydrogen storage materials: high-surface area materials and nanostructured metal hydrides. For the first subject we concentrate on carbon nanotubes and activated charcoal and we regard magnesium as a model system for hydrogen storage in metal hydrides in the second part.

High surface area materials

High surface area materials store hydrogen due to an attractive interaction between the surface and hydrogen molecules. Carbon nanotubes combine a high surface area (about 550 m^2/g) with an uncommon, tubular structure, which attracted much interest for hydrogen storage applications worldwide. The reported hydrogen storage figures for single walled carbon nanotubes and nanofibers vary enormously. We point out some possible sources of the discrepancies. The high capacities cannot be understood using classical grand canonical Monte Carlo calculations or *ab initio* calculations.

We compare the adsorption capacity of activated charcoals, single walled carbon nanotubes and multi walled carbon nanotubes. The hydrogen capacities scale basically with the surface area that is accessible for hydrogen molecules. The adsorption enthalpy is obtained from measurements of the hydrogen pressure as a function of the temperature of the high-surface area sample. The results show that the interaction potential (5 kJ/mole) and adsorption environment are basically equal for all investigated materials. Apparently the curvature of the graphite of which the carbon nanotubes are constituted, does not influence storage properties of these materials under our experimental conditions. Inelastic neutron scattering experiments show that hydrogen on carbon materials is present in the form of molecules, since the rotational scattering peak is present. No atomic hydrogen is observable.

For in-detail studies we use high resolution inelastic neutron scattering to measure the rotational spectrum of hydrogen molecules adsorbed on single walled carbon nanotubes at low temperatures. Apart from that a full isotherm is also measured. We are able to interpret the isotherm and the rotational spectra as follows. The grooves between the single walled carbon nanotubes become occupied first, after which the curved surface becomes covered with hydrogen. The latter process is different from hydrogen adsorption on planar graphite, most likely due to the curved nature of the surface. Finally the surface is completely occupied, after which a second monolayer starts to form. This second layer shows a much lower interaction potential and less hindering of the rotations of the hydrogen molecules.

Materials that contain ionic centers such as zeolites and metal organic frameworks exhibit a higher adsorption enthalpy than carbon surfaces. The limited number of ionic centers per gram of material limits the adsorption capacity. Hydrogen clathrates may be promising new candidates for hydrogen storage, although they operate under relatively high pressure.

Kinetic factors for hydriding of magnesium

Magnesium metal is important for hydrogen storage applications as it is one of the few compounds that is known to absorb hydrogen in an amount (about 7 wt%) that meets the demands of the department of energy of the USA. Due to the high absorption enthalpy, however, the equilibrium pressures under ambient conditions are extremely low. During hydriding a hydride layer can form on the surface of large particles, which makes the hydriding process very slow for such particles and therefore high operation temperatures are needed. The sorption speed and operation temperature can be brought down by ball milling magnesium hydride in order to break the particles up and by adding catalysts such as Nb and V.

By a comparison of vibrational spectra of both bulk and ball milled magnesium hydride with density functional theory (DFT) calculations, we are able to show that the defects and deformations of the magnesium hydride structure inside the particles that are caused by the ball milling treatment are not important for the increase in hydriding kinetics, since these defects are annealed out when the hydrogen content of the ball milled particles is cycled. Still, the decrease in the particle size influences the surface area through which the hydrogen atoms enter the material and decreases the diffusion path lengths. The kinetics of the latter have been studied by means of molecular dynamical DFT calculations. We show that the diffusion coefficient of hydrogen in magnesium metal is large enough for fast kinetics.

We investigate the heat effects that play a role in the hydriding process of magnesium. Due to the relatively large absorption enthalpy, the heat that is generated when only 1.2% of a magnesium particle transforms to magnesium hydride is enough to neutralize the driving force completely under typical hydriding conditions. This effect is also present -although to a lesser extent- in other metal hydrides.

Apart from ball milling, the use of a finely dispersed catalyst like Nb or V increases the sorption speed while it lowers the sorption temperature by about 50 K. Overall, this brings forward applications with total sorption speeds of minutes and in a more accessible temperature range (i.e. between room temperature and 300 degrees Celsius). *In situ* neutron diffraction experiments reveal some key elements: during hydrogen sorption a magnesium hydride phase is present with a hydrogen concentration much below the equilibrium content which likely speeds up the process. The finding of a perovskite phase with an estimated composition of $Nb(Mg_{0.333}Nb_{0.667})O_3$, though in weak proportions, is likely to play a catalytic role for the Mg particles, since it may provide diffusion channels through the oxide barrier around the magnesium particles.

Conclusions

We conclude that high surface area materials are unlikely to become important in the near future since the adsorption interaction on most of the possible adsorption sites is too low to bind enough hydrogen under practical conditions. For high enthalpy materials such as magnesium we conclude that they can be used efficiently for mobile

hydrogen storage purposes when intermediate temperature (i.e. 200-300 degrees Celsius) fuel cells are available that can provide the heat for desorption of hydrogen from these materials.

Samenvatting

Naar het waterstof tijdperk?

Berekeningen en neutronen verstrooiing aan potentiële materialen voor waterstofopslag

door H. G. Schimmel

Inleiding

Duurzame ontwikkeling betekent dat er alternatieven gevonden moeten worden voor het gebruik van fossiele brandstoffen om in onze energiebehoefte te voorzien, zonder daarbij de natuurlijke balans te verstoren. Omdat koolstofdioxide over het algemeen wordt gezien als de veroorzaker van grote klimaatveranderingen in de toekomst, concentreert de duurzame productie van energie zich voornamelijk op processen die koolstofdioxide neutraal zijn. Met name een duurzame manier van transporteren impliceert dat andere keuzes dan het gebruik van fossiele brandstoffen noodzakelijk zijn. In deze context is waterstof is een goede energiedrager omdat er alleen water vrijkomt bij gebruik in een brandstofcel en een beperkte hoeveelheid bijproducten als het wordt gebruikt in traditionele verbrandingsmotoren. Het transport van waterstof is echter een grote uitdaging. Onze vergelijking tussen verbrandingmotoren en elektrische motoren met accu's laat zien dat de opslag van energie in een voertuig een oud probleem is.

Waterstofopslag

Waterstof is een erg licht en vluchtig gas waardoor hoge drukken, lage temperaturen of een opslagmateriaal nodig zijn. Gebruikmakend van de minimale waarden voor het rendement volgens de eisen van het ministerie van energie van de Verenigde Staten, hebben we randvoorwaarden voor de opslagenthalpie als functie van de gebruikstemperatuur afgeleid. We laten zien dat het rendement voor waterstofopslag in materialen die bij hoge temperatuur werken, zoals Mg, lager is dan 90% voor zelfstandige toepassingen. Deze restrictie geldt niet als er brandstofcellen worden gebruik die werken bij middelhoge temperatuur (gebruikstemperaturen hoger dan

200 graden Celsius) omdat deze cellen restwarmte produceren voor de desorptie van waterstof uit materialen met een hoge opslagenthalpie.

Dit proefschrift karakteriseert twee soorten waterstofopslagmaterialen: materialen met een hoog intern oppervlak en nanogestructureerde metaalhydriden. We concentreren ons op koolstof nanotubes en actieve koolstof voor de eerste soort materialen, terwijl we magnesium als een model systeem voor waterstofopslag in metaalhydriden beschouwen.

Materialen met een hoog oppervlak

Waterstofopslagmaterialen met een hoog oppervlak slaan waterstof op door een aantrekkende interactie tussen het oppervlak en waterstof molekulen. Koolstof nanotubes combineren een hoog oppervlak (ongeveer 500 m^2/g) met een ongewone, buisvormige structuur, hetgeen wereldwijd veel interesse voor waterstofopslag toepassingen heeft gewekt. De gerapporteerde waarden voor de waterstofopslagcapaciteit van enkelwandige koolstof nanotubes en nanofibers variëren enorm. We laten enkele oorzaken van de verschillen zien. De hoge opslagcapaciteiten kunnen niet verklaard worden gebruik makend van Monte Carlo simulaties of ab initio berekeningen.

We vergelijken de adsorptiecapaciteit van aktieve kool, enkelwandige en meerwandige koolstof nanotubes. The waterstofopslagcapaciteit schaalt in principe met het oppervlak dat bereikbaar is voor waterstofmolekulen. De adsorptieenthalpie is bepaald uit metingen van de waterstofdruk als functie van de temperatuur van de hoogoppervlakmaterialen. De resultaten laten zien dat de interactiepotentiaal (5 kJ/mol) en de adsorptieomgeving in feite gelijk zijn voor al de onderzochte materialen. Blijkbaar worden de opslageigenschappen onder de gekozen experimentele omstandigheden niet beïnvloed door het gekromde oppervlak van het grafiet waaruit de nanotube is opgebouwd. Inelastische neutronenverstrooiingsexperimenten laten een verstrooiingspiek zien die het gevolg is van moleculaire rotaties. Dit wijst erop dat waterstof op koolstof materialen aanwezig is in de vorm van moleculen. We vinden geen aanwijzingen voor atomair waterstof in deze materialen.

Om het spectrum van waterstof geabsorbeerd op enkelwandige koolstof nanotubes bij lage temperaturen meer gedetailleerd te bekijken, gebruiken we hoge-resolutie inelastische neutronenverstrooiing. Daarnaast hebben we een volledige isotherm gemeten. We kunnen de isotherm en de rotatie spectra als volgt interpreteren: de groeven tussen de nanotubes worden het eerst bezet door waterstofmolekulen en daarna wordt ook het oppervlak van de nanotubes bedekt. Dit laatste proces verschilt van het geval van waterstof op vlak grafiet, waarschijnlijk omdat het oppervlak van de nanotubes gekromd is. Tenslotte wordt het oppervlak geheel bedekt, waarna een tweede monolaag wordt gevormd. Deze tweede laag laat een veel lagere interactie en minder hindering van de rotaties van de waterstofmolekulen zien.

Materialen die ionische plaatsen bevatten zoals zeolieten en metaalorganische

netwerken hebben een hogere adsorptieenthalpie dan koolstof oppervlakken. Het lage aantal ionische plaatsen per gram materiaal limiteert de opslagcapaciteit. Waterstofclathraten zouden veelbelovende nieuwe kandidaten voor waterstofopslag kunnen zijn, hoewel ze onder relatief hoge druk werken.

Kinetische factoren voor het hydreren van magnesium

Magnesium metaal is belangrijk voor waterstofopslag toepassingen omdat het een van de weinige materialen is die genoeg waterstof opneemt (ongeveer 7 gewichtsprocent) om aan de eisen van het ministerie van energie van de Verenigde Staten te voldoen. Vanwege de hoge absorptieënthalpie, zijn de evenwichtsdrukken onder omgevingsomstandigheden extreem laag. Doordat er zich gedurende hydrering een hydride laag op het oppervlak van de deeltjes kan vormen, wordt het hydrerings proces erg traag voor grote deeltjes. Hoge temperaturen zijn hierdoor noodzakelijk. De opname snelheid en de gebruikstemperatuur kunnen worden verbeterd door het materiaal te vermalen in een kogelmolen zodat de deeltjes breken in kleinere eenheden en door katalysatoren zoals Nb en V toe te passen.

Door middel van een vergelijking van de vibratiespectra van onbehandele en vermalen magnesium hydride met density functional theory (DFT) berekeningen, kunnen we laten zien dat de defecten en deformaties die veroorzaakt zijn door het vermalen van de magnesiumhydride deeltjes, niet belangrijk zijn voor de verbetering van de waterstofopslag snelheid omdat deze defecten en deformaties verdwijnen tijdens laad-ontlaad cycli. De kleinere deeltjesgrootte zal vanzelf het beschikbare oppervlak waardoor waterstof de magnesiumdeeltjes binnengaat vergroten en zal de diffusiepadlengten door het magnesium verminderen. We laten zien dat de diffusiecoëfficiënt van waterstof in magnesium hoog genoeg is voor snelle kinetiek.

We onderzoeken de warmteëffecten die een rol spelen bij het hydreren van magnesium. Dankzij de grote absorptieënthalpie wordt de drijvende kracht voor hydrering volledig geneutraliseerd door de warmte die vrijkomt als slechts 1,2% van een magnesiumdeeltje in magnesiumhydride transformeert. Dit effect is ook aanwezig, hoewel minder uitgesproken, in andere metaalhydriden.

Naast het vermalen van de deeltjes, verhoogt ook de toevoeging van katalysator zoals Nb of V de sorptiesnelheid terwijl de temperatuur verlaagd wordt met ongeveer 50 K. Tesamen levert dit een materiaal op dat kan worden gehydreerd in enkele minuten in een beter bereikbaar temperatuurbereik (dat wil zeggen tussen kamertemperatuur en 300 graden Celsius). In situ neutronendiffractie experimenten onthullen enkele belangrijke elementen van dit gekatalyseerde systeem: tijdens waterstofadsorptie is er een magnesiumhydride fase met lagere bezettingen van waterstofposities aanwezig, die de diffusiesnelheid kan verhogen. De vondst van een perovskietfase met een geschatte samenstelling $Nb(Mg_{0.333}Nb_{0.667})O_3$, alhoewel in kleine hoeveelheden, is interessant omdat deze fase waarschijnlijk een katalytische rol speelt in het hydreren van Mg deeltjes. Deze fase zou ook diffusie kanalen door de MgO barrière rond de Mg deeltjes kunnen vormen.

We concluderen dat het onwaarschijnlijk is dat materialen met een hoog opper-vlak belangrijk worden in de nabije toekomst omdat de adsorptie interactie van de meerderheid van de plaatsen in het materiaal te laag is om genoeg waterstof te binden onder praktische condities. Voor de materialen met een hoge bindingsenthalpie zoals magnesium, concluderen we dat ze kunnen worden gebruikt met een hoge efficien-tie voor mobiele toepassingen als middelhoge temperatuur brandstofcellen (dat wil zeggen 200-300 graden Celsius) beschikbaar zijn die de warmte kunnen leveren die nodig is voor waterstof desorptie uit deze materialen.

Appendices

Appendix A

Theory and methods

In this appendix we will describe the theory and methods that were used for the experiments and calculations described in this thesis. We start with a description of the theory of neutron and X-ray diffraction experiments and of inelastic neutron scattering, which we illustrate with an example of a neutron scattering instrument. The scattering of neutron by hydrogen molecules show some special features, which we work out. After that we introduce various computational methods that are nowadays available to simulate physical systems.

A.1   Scattering techniques

Neutron and X-ray scattering are frequently used in condensed matter studies as they reveal detailed information on the structure *and* dynamics of a sample at length scales of roughly 1 Å to 1 μm and timescales between picoseconds and nanoseconds. The fact that the signal represents an average over the whole sample, contrary to microscopy methods, is in many cases an advantage. The influence of the radiation on the sample is normally very low and the sample may be kept in all sorts of special environments (high or low temperature, pressure, magnetic or electric field), provided that the probe radiation can still enter the sample area.

X-rays versus neutrons as probe radiation

Basically the theory of neutron and X-ray scattering are very similar, albeit that neutrons scatter from the nuclei, whereas X-rays scatter from the electrons in the sample. For practical use, however, there are more differences. The low flux from present-day neutron sources makes that large samples are used —typically a gram— and that therefore the whole instrument becomes larger. Conversely, X-rays are easy to produce and can be used in desktop-size diffractometers for structural investigations of most materials, especially when one wants to perform room temperature experiments. As neutrons have a large penetrating power in most materials, the need for shielding makes that the instruments not only large, but also quite heavy.
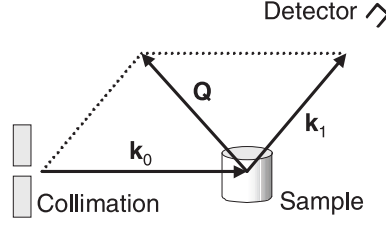
Figure A.1: Incident and scattered neutron path with their momenta $\mathbf{k}_0$ and $\mathbf{k}_1$ and the construction of the momentum transfer vector. Collimation, sample and a detector are schematically drawn.

Another drawback is that a moderate source is already very expensive, even when these costs are spread over a number of instruments around a single neutron source. The penetrating power of neutrons also enables one to use special equipment such as high-pressure, low- and high-temperature sample cells. Furthermore the scattering power varies irregularly with the composition of the nucleus of an atom itself, in contrast with X-rays where the scattering only scales with the number of electrons in an atom. Isotope substitution studies use this effect to isolate the investigated phenomenon from the background. For inelastic scattering, neutrons are especially suited as their energies and wavelengths match with those of the sample atoms. The fact mentioned above that neutrons interact with the nuclei instead of the electrons makes that calculation methods such as presented later in section A.2 are more easily used to simulate neutron than X-ray scattering patterns.

The observables of scattered radiation are changes in direction $\mathbf{e}$ and energy E. Both observables can be presented by the momentum of the radiation before, $\mathbf{p}_0 = \hbar \mathbf{k}_0 = \sqrt{2mE_0}\,\mathbf{e}_0$ and after $\mathbf{p}_1 = \hbar \mathbf{k}_1 = \sqrt{2mE_1}\,\mathbf{e}_1$ the sample, using the wavevector $\mathbf{k}$, the mass m of the radiation quanta and Dirac's constant $\hbar$. For photons these relationships are slightly different as their momenta are related to the photon energy via the speed of light c, $\mathbf{p} = \hbar \mathbf{k} = \frac{E}{c}\,\mathbf{e}$. Figure A.1 shows an incident and scattered neutron path, their wavevectors and the construction of the momentum transfer vector $\hbar \mathbf{Q}$. First we will present the theory of neutron diffraction, where we are only interested in scattered neutrons that have no energy change in the sample, after which we introduce the what is known as inelastic scattering, where we measure also energy exchange with the sample.

A.1.1 Neutron diffraction

In a diffraction experiment only momentum is transferred to the lattice and the long range structure of a material is probed. We consider a neutron emitted from a neutron source, which is characterized by its wave-vector $\mathbf{k}_0$ or, equivalently, its momentum vector $\hbar \mathbf{k}_0$. After the scattering event it is described by the vector $\mathbf{k}_1$.

The momentum transferred to the neutron is

$$\hbar\mathbf{Q} = \hbar(\mathbf{k}_1 - \mathbf{k}_0), \tag{A.1}$$

and the energy which is transferred to the neutron is

$$E = E_1 - E_0 = \frac{\hbar^2 \left(|\mathbf{k}_1|^2 - |\mathbf{k}_0|^2\right)}{2m_n}, \tag{A.2}$$

with m_n the mass of a neutron.

In a diffraction experiment we send a beam with an intensity $\Phi(\mathbf{k}_0)$ through a sample and measure the intensity I in the detector with a solid angle $\mathrm{d}\Omega$ around the direction of the scattered wavevector $\mathbf{k}_1$. The experiment is arranged in such a way that only elastically scattered neutrons (i.e. no energy transfer occurred in the scattering event) are counted or that the inelastically scattered neutron give a negligible contribution. We measure the differential cross section, given by:

$$\frac{\mathrm{d}\sigma}{\mathrm{d}\Omega} = \frac{I}{\Phi(\mathbf{k}_0)\mathrm{d}\Omega}. \tag{A.3}$$

When the scattering probability is small, $\mathrm{d}\sigma/\mathrm{d}\Omega$ is independent of the incident flux $\Phi(\mathbf{k}_0)$ and depends solely on the structure and size of the sample. If we take the sample size much smaller than the distance between sample and detector, the sample may be regarded as a perfect point-like scatterer, in which case $\mathrm{d}\sigma/\mathrm{d}\Omega$ is fully determined by the internal structure of the sample.

A neutron scattering instrument

A neutron scattering instrument will not fit on a desktop, a few exceptions excluded, but is rather of the size of a large room. We take the neutron diffractometer GEM as an example. This spectrometer is in commission at the spallation source ISIS in Oxfordshire, United Kingdom. The spallation source of ISIS consists of a water-cooled tantalum target that is bombarded with a intense, 50 Hz–pulsed proton beam. As a result of the high-energy collisions that take place in the target, neutrons with varying energies are produced, which are moderated to a certain temperature and guided to the instruments that are grouped around the target. After a certain amount of time determined by the length of the flight path between target and sample and the velocity (energy) of the neutron, the neutrons arrive at the sample. Here they may be scattered in different directions according to the cross-section of the sample.

In a diffractometer like GEM the inelastic scattering is assumed to be negligible small and of no influence on the data analysis. A certain fraction of the scattered neutrons that is determined by the solid angle of the detectors, is counted in detector tubes which are placed in banks at known distances around the sample. From the time-of-flight from target to detector, the velocity and thus the energy and initial
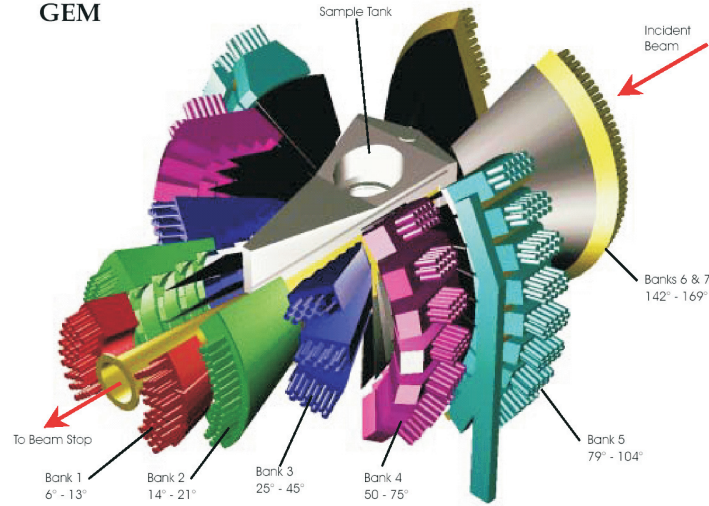
Figure A.2: The neutron scattering spectrometer GEM, ISIS, UK. Picture taken from the ISIS website.

and final momentum can be calculated, which means that the momentum transfer is easily evaluated when the angle of the detector tube is known. Since a whole range of incident neutron energies are produced by the target, the momentum transfer changes as a function of the time-of-flight and each detector tube takes a diffraction pattern. The patterns from all diffraction detectors are grouped into banks after the experiment has been stopped. Figure A.2 shows a scheme of the instrument with some the detector banks indicated. Diffraction patterns from neutron diffractometers at spallation sources are normally given as a function of the time-of-flight or, more general, of d-spacing, which is defined as $d = 2\pi/|\mathbf{Q}|$.

Using an energy selector, one can also measure the energy transfer between neutron and sample, which is used for inelastic scattering spectrometers. In the case of continuous sources such as a reactor, the neutrons are normally monochromized for diffraction experiments and monochromized *and* pulsed for inelastic experiments. The websites of the European neutron sources ILL and ISIS provide more information on the neutron scattering technique and the different types of instruments [112].

The scattering event

The neutron experiences a potential $V(\mathbf{r})$ at a point $\mathbf{r}$ in the sample due to the presence of nuclei in the sample. This potential may induce a transition of the initial state Ψ_0 of the neutron to a scattered state Ψ_1 and of the sample from state n_0 to n_1. In the language of quantum mechanics, Fermi's Golden Rule gives the

transition probability as:

$$W_{0 \to 1} = \frac{2\pi}{\hbar} |\langle \Psi_1 n_1 | V(\mathbf{r}) | \Psi_0 n_0 \rangle|^2 \rho(\mathbf{k}_1), \tag{A.4}$$

where $\rho(\mathbf{k}_1)$ is the density of scattered states. We can now relate the potential $V(\mathbf{r})$ of the sample to the differential cross section as follows:

$$\left(\frac{d\sigma}{d\Omega} \right)_{0 \to 1} = \frac{W_{0 \to 1}}{\Phi(\mathbf{k}_0) d\Omega}. \tag{A.5}$$

We see that the scattering pattern of a sample is directly related to the potential field of the neutrons in the sample. We assume that the form of this potential landscape is congruent with the atomistic picture we have of matter. The Fermi pseudo potential relates these two using the set of positions, $\mathbf{R}_i$ and the proportionality factor b_i:

$$V(\mathbf{r}) = \frac{2\pi\hbar^2}{m_n} \sum_i b_i \, \delta(\mathbf{r} - \mathbf{R}_i). \tag{A.6}$$

Here we introduced the constant b_i, which is called the scattering length. It expresses the strength of the interactions between neutron and nucleus. The scattering length is a complex quantity which depends on both the number of protons and neutron in a nucleus and on the spin state of the neutron and nucleus. We will discuss the scattering event in more detail section A.1.2

Spin incoherence

The dependence of the scattering length on the spin of the neutron gives spin incoherence effects which are not present in X-ray scattering experiments. Given the spins of the neutron and the nucleus, σ_0 and I_0, quantum mechanics predicts that the two spins can be combined in two different ways [113]. As the neutron has spin $\frac{1}{2}$, the number of possibilities depend on the spin of the nucleus: $2(I + 1)$ possibilities with a scattering length b^+ and $2I$ with a scattering length b^-. The weighted average of these two gives the coherent scattering length:

$$b_{coh} = \frac{1}{2I + 1} \left[(I + 1)b^+ + Ib^- \right]. \tag{A.7}$$

This scattering length is called coherent because it is the part of the scattering that is the same for all nuclei, irrespective of the initial spin states of the neutron and the nuclei. The coherent scattering length is the scattering power of the sample as a whole, which enables the observation of coherence effects between different atoms, i.e. long range ordering may be observed. Diffraction experiments can be used to determine the structure of a material from the coherent scattering, which shows peaks when the structure of the sample is periodic.

The deviations from this coherent scattering length are called the incoherent scattering. Incoherent scattering is determined by a single atom and is therefore

isotropic [114]. We note 1) that incoherence results from the difference between the two scattering lengths b^+ and b^-, 2) that X-ray scattering shows no dependence on nuclear spin and has therefore no spin incoherence 3) that different isotopes have different scattering lengths, which gives also an incoherent contribution to the scattering and finally 4) that isotopes with zero nuclear spin (^{16}O, ^{12}C) have only one scattering length and scatter only coherently.

Coherent scattering by crystals

When the sample size is small compared to the distances source-sample and sample-detector, the spatial part of the incident and scattered state of the neutron can be approximated by plane waves. Using the plane-wave approximation we can work out equation A.5 and find the coherent differential cross section as a function of the set of atom positions, $\mathbf{R}_i$, and the wave vector transfer $\mathbf{Q}$ (equation A.1):

$$\left(\frac{\mathrm{d}\sigma}{\mathrm{d}\Omega}\right)_{coh} = \left|\sum_i \langle b_i \rangle \, \mathrm{e}^{\mathrm{i}\mathbf{Q}\cdot\mathbf{R}_i}\right|^2. \tag{A.8}$$

Crystals possess a regular arrangement of the atoms and are characterized by the unit cell, the building block of the crystal. Consider a unit cell defined by the set of vectors $\mathbf{a}_1, \mathbf{a}_2$ and $\mathbf{a}_3$. The position of a certain unit cell can be defined by three integers:

$$\mathbf{L} = l_1\mathbf{a}_1 + l_2\mathbf{a}_2 + l_3\mathbf{a}_3. \tag{A.9}$$

The position of the ith atom of the lattice can then be expressed in terms of the vector pointing to the the unit cell $\mathbf{L}$ and the vector from the unit cell origin to the the atom $\mathbf{r}_j$:

$$\mathbf{R}_i = \mathbf{r}_j + \mathbf{L}. \tag{A.10}$$

We define the reciprocal lattice vectors $\mathbf{b}_{1,2,3}$ by:

$$\mathbf{a}_\nu \cdot \mathbf{b}_\mu = 2\pi\delta_{\nu\mu} \; (\nu, \mu = 1, 2, 3). \tag{A.11}$$

A reciprocal lattice vector can be written as

$$\mathbf{G}_{hkl} = h\mathbf{b}_1 + k\mathbf{b}_2 + l\mathbf{b}_3, \; (h, k, l \text{ are integers}). \tag{A.12}$$

Using the definition of the nuclear structure factor,

$$F(\mathbf{Q}) = \sum_j \langle b_j \rangle \mathrm{e}^{\mathrm{i}\mathbf{Q}\cdot\mathbf{r}_j}, \tag{A.13}$$

we can rewrite equation A.8 as:

$$\left(\frac{\mathrm{d}\sigma}{\mathrm{d}\Omega}\right)_{coh} = N\frac{(2\pi)^3}{v_a} \left|F(\mathbf{Q})\right|^2 \sum_{\mathbf{G}_{hkl}} \delta(\mathbf{Q} - \mathbf{G}_{hkl}), \tag{A.14}$$

where N denotes the number of unit cells and v_a is the unit cell volume. The possible reflection directions of the neutrons are determined by the reciprocal lattice vectors. Neutrons are only diffracted into the directions given by the condition $\mathbf{Q} = \mathbf{G}_{hkl}$. The intensity of these reflections are determined by the structure factor, which is in turn completely determined by the contents of the unit cell. The derivation we give here is valid for a perfect single crystal, whereas in the case of powders we find that the reciprocal space of the powder sample consists of spheres with radius $|\mathbf{G}_{hkl}|$. A ring $\mathbf{Q}$-vectors now fulfill the reflection condition $\mathbf{Q} = \mathbf{G}_{hkl}$ and Debye-Scherrer cones are observed.

What happens to the reflection intensities when thermal motions smear the atoms out? We assume that now the position of an atom is given by:

$$\mathbf{R}_i = \mathbf{r}_j + \mathbf{L} + \mathbf{u}_i, \tag{A.15}$$

where $\mathbf{u}$ is the (isotropic) displacement of the ith atom. This gives an extra term

$$T_j(\mathbf{Q}) = \left\langle e^{i\mathbf{Q}\cdot\mathbf{u}_j} \right\rangle = e^{-\frac{1}{6}\mathbf{Q}^2\langle\mathbf{u}_j^2\rangle}, \tag{A.16}$$

the Debye-Waller factor, which we put into the structure factor as well:

$$F(\mathbf{Q}) = \sum_j \langle b_j \rangle \, e^{-\frac{1}{6}\mathbf{Q}^2\langle\mathbf{u}_j^2\rangle} \, e^{i\mathbf{Q}\cdot\mathbf{r}_j}. \tag{A.17}$$

The thermal displacements of the atoms in the crystal multiply the structure factor with a decaying exponential factor, especially at higher temperatures when the displacements are larger. Here we disregarded the fact that the atom actually move due to the thermal activation. This time-dependence of the atomic positions in the sample results in inelastic scattering, which we deal with in the next section.

A.1.2 Inelastic neutron scattering

In an inelastic scattering experiment not only momentum, but also energy transfer is analyzed, meaning that the structure *and* the dynamics of a sample material is measured. Stated differently, when the potential V the neutron experiences in a sample is not only position-, but also time-dependent, $V = V(\mathbf{r}, t)$, inelastic scattering events occur. Instruments which determine the energy differences between incident and scattered neutrons effectively measure the double differential cross section:

$$\frac{\mathrm{d}\sigma}{\mathrm{d}\Omega\,\mathrm{d}E_1} = \frac{I}{\Phi(\mathbf{k}_0)\,\mathrm{d}\Omega\,\mathrm{d}E_1}, \tag{A.18}$$

which includes the energy window $\mathrm{d}E_1$ around the final energy E_1 of the scattered neutron. The Golden Rule can again be applied inserting $V(\mathbf{r}, t)$ instead of $V(\mathbf{r})$ in equation A.5. We then have to average equation A.5 with the possibility $p(n_0)p(\sigma_0)$ of finding the initial state n_0 of the sample and the initial spin state σ_0 of the

neutron. By summing over all final states, using the plane wave approximation as in the diffraction case and writing the conservation of energy as a δ-function, one gets:

$$
\frac{\mathrm{d}^2\sigma}{\mathrm{d}\Omega\,\mathrm{d}E_1} = \frac{|\mathbf{k}_1|}{|\mathbf{k}_0|} \sum_{n_0\sigma_0} p(n_0)p(\sigma_0) \sum_{n_1\sigma_1} \left| \langle \sigma_1 n_1 | \sum_i b_i\, \mathrm{e}^{\mathrm{i}\mathbf{Q}\cdot\mathbf{R}_i} |n_0\sigma_0\rangle \right|^2 \tag{A.19}
$$
$$
\cdot\,\delta(\hbar\omega - E_0 + E_1)
$$

The δ-function can be written as a Fourier-integral from time t to the radial frequency ω, the latter being proportional to the energy. The expression can now be worked out using Heisenberg operators and one finds:

$$
\frac{\mathrm{d}^2\sigma}{\mathrm{d}\Omega\,\mathrm{d}\omega} = \frac{|\mathbf{k}_1|}{|\mathbf{k}_0|} \frac{1}{2\pi} \int\limits_{-\infty}^{+\infty} \mathrm{d}t\, \mathrm{e}^{-\mathrm{i}\omega t} \sum_{i=1}^{N}\sum_{j=1}^{N} \langle b_i b_j\rangle \left\langle \mathrm{e}^{\mathrm{i}\mathbf{Q}\cdot\mathbf{R}_i(0)} \mathrm{e}^{-\mathrm{i}\mathbf{k}\cdot\mathbf{R}_j(t)} \right\rangle \tag{A.20}
$$

The distinction between coherent and incoherent scattering also applies to inelastic scattering: the expansion of the term $\langle b_i b_j\rangle$ gives

$$
\langle b_i b_j\rangle = \langle b_i\rangle\langle b_j\rangle + \delta_{ij}(\langle |b_i|^2\rangle - \langle b_i\rangle\langle b_j\rangle) = b_{coh}^2 + \delta_{ij} b_{inc}^2. \tag{A.21}
$$

Using $\sigma_{coh} = 4\pi b_{coh}^2$ and $\sigma_{inc} = 4\pi b_{inc}^2$, equation (A.20) can be split into two parts, a coherent part

$$
\left(\frac{\mathrm{d}^2\sigma}{\mathrm{d}\Omega\,\mathrm{d}\omega}\right)_{coh} = \frac{\sigma_{coh}}{4\pi} \frac{|\mathbf{k}_1|}{|\mathbf{k}_0|} \frac{1}{2\pi} \int\limits_{-\infty}^{+\infty} \mathrm{d}t\, \mathrm{e}^{-\mathrm{i}\omega t} \sum_{i=1}^{N}\sum_{j=1}^{N} \left\langle \mathrm{e}^{\mathrm{i}\mathbf{Q}\cdot\mathbf{R}_i(0)} \mathrm{e}^{-\mathrm{i}\mathbf{Q}\cdot\mathbf{R}_j(t)} \right\rangle \tag{A.22}
$$

and an incoherent part

$$
\left(\frac{\mathrm{d}^2\sigma}{\mathrm{d}\Omega\,\mathrm{d}\omega}\right)_{inc} = \frac{\sigma_{inc}}{4\pi} \frac{|\mathbf{k}_1|}{|\mathbf{k}_0|} \frac{1}{2\pi} \int\limits_{-\infty}^{+\infty} \mathrm{d}t\, \mathrm{e}^{-\mathrm{i}\omega t} \sum_{j=1}^{N} \left\langle \mathrm{e}^{\mathrm{i}\mathbf{Q}\cdot\mathbf{R}_j(0)} \mathrm{e}^{-\mathrm{i}\mathbf{Q}\cdot\mathbf{R}_j(t)} \right\rangle \tag{A.23}
$$

The coherent part contains a sum of the terms $\mathrm{e}^{\mathrm{i}\mathbf{Q}\cdot\mathbf{R}_i(0)}\mathrm{e}^{-\mathrm{i}\mathbf{Q}\cdot\mathbf{R}_j(t)}$ for all combinations of particles. This term takes into account the correlations between the position of a particle and the position of every other particle, included itself, at different times. It gives therefore interference effects: the sample scatters as a whole. Only repeated distances (periodic structure) and joint motions (phonons) are seen. This explains the name coherent.

The incoherent part is a sum of the terms $\mathrm{e}^{\mathrm{i}\mathbf{Q}\cdot\mathbf{R}_j(0)}\mathrm{e}^{-\mathrm{i}\mathbf{Q}\cdot\mathbf{R}_j(t)}$ for every particle. This term expresses the correlation between the positions of a particle j *itself* at different times. Thus the incoherent part represents the sum of motions of individual particles.

Definitions

The intermediate function $I(\mathbf{Q}, t)$ is defined as

$$I(\mathbf{Q}, t) = \frac{1}{N} \sum_{i=1}^{N} \sum_{j=1}^{N} \left\langle e^{i\mathbf{Q}\cdot\mathbf{R}_i(0)} e^{-i\mathbf{Q}\cdot\mathbf{R}_j(t)} \right\rangle \tag{A.24}$$

The scattering function $S(\mathbf{Q}, \omega)$ is defined by

$$S(\mathbf{Q}, \omega) = \frac{1}{2\pi} \int\limits_{-\infty}^{+\infty} dt\, e^{-i\omega t}\, I(\mathbf{Q}, t) \tag{A.25}$$

So that the coherent double differential cross section is

$$\left(\frac{d^2\sigma}{d\Omega d\omega} \right)_{coh} = \frac{N\sigma_{coh}}{4\pi} \frac{|\mathbf{k}_1|}{|\mathbf{k}_0|} S(\mathbf{Q}, \omega) \tag{A.26}$$

Similarly the self intermediate function and the incoherent scattering function can be defined as

$$I_s(\mathbf{Q}, t) = \frac{1}{N} \sum_{j=1}^{N} \left\langle e^{i\mathbf{Q}\cdot\mathbf{R}_j(0)} e^{-i\mathbf{Q}\cdot\mathbf{R}_j(t)} \right\rangle \tag{A.27}$$

$$S_i(\mathbf{Q}, \omega) = \frac{1}{2\pi} \int\limits_{-\infty}^{+\infty} dt\, e^{-i\omega t}\, I_s(\mathbf{Q}, t) \tag{A.28}$$

Then the incoherent double differential cross section is

$$\left(\frac{d^2\sigma}{d\Omega d\omega} \right)_{inc} = \frac{N\sigma_{inc}}{4\pi} \frac{|\mathbf{k}_1|}{|\mathbf{k}_0|} S_i(\mathbf{Q}, \omega) \tag{A.29}$$

A.1.3   Neutron scattering by hydrogen molecules

The scattering of a neutron by a hydrogen molecules shows some remarkable effects. The two protons in the molecule may have correlated spins, which makes that the scattering length of the molecule as a whole differs drastically from the sum of the scattering contribution of the two protons apart. Furthermore, the scattering length is very dependent on the initial energy of the neutron when this energy is comparable to the excitation energies of the rotations of the molecule. First we will describe the scattering of a neutron by a single proton in more detail. After handling about ortho and para forms of the hydrogen molecule, we present the scattering of neutrons by hydrogen molecules.

Scattering by a single atom

Imagine a single free hydrogen atom. Its nucleus with spin I is described by $\mathbf{i}_0$. A neutron (spin $\frac{1}{2}$) with a wave-vector $\mathbf{k}_0$ and spin state $\boldsymbol{\sigma}_0$ interacts with this nucleus, which may lead to scattering. We describe the neutron and the proton as one quantum system. The spins of the two particles can combine forming the state $|+\rangle$ with total spin $t = I + \frac{1}{2}$ or state $|-\rangle$ with total spin $t = I - \frac{1}{2}$. These two situations have different scattering lengths b^+ and b^-, respectively. Now we define the scattering length operator $\hat{b}$:

$$\hat{b}|+\rangle = b^+|+\rangle, \quad \hat{b}|-\rangle = b^-|-\rangle, \tag{A.30}$$

which can be written in the form

$$\hat{b} = A + B\boldsymbol{\sigma} \cdot \mathbf{i} \tag{A.31}$$

with

$$A = \frac{1}{2I+1}[(I+1)b^+ + Ib^-], \tag{A.32}$$

$$B = \frac{1}{2I+1}[b^+ - b^-]. \tag{A.33}$$

The double differential cross section for the transition $0 \to 1$, in analogy to equation A.20, is:

$$\left(\frac{\mathrm{d}^2\sigma}{\mathrm{d}\Omega\,\mathrm{d}E_1}\right)_{0\to1} = \frac{|\mathbf{k}_1|}{|\mathbf{k}_0|}\left|\langle\boldsymbol{\sigma}_1\mathbf{i}_1|\hat{b}\,\mathrm{e}^{\mathrm{i}\mathbf{Q}\cdot\mathbf{R}_i}|\boldsymbol{\sigma}_0\mathbf{i}_0\rangle\right|^2 \tag{A.34}$$

As the scattering length density operator works on the spin state of the neutron before and after the scattering process, we need to evaluate the term $\langle\boldsymbol{\sigma}_1\mathbf{i}_1|\hat{b}|\boldsymbol{\sigma}_0\mathbf{i}_0\rangle$ to find the effective scattering length of the process $0 \to 1$. Using the expressions for the Pauli spin operators or matrices, we find that

$$\langle\boldsymbol{\sigma}_1\mathbf{i}_1|\hat{b}|\boldsymbol{\sigma}_0\mathbf{i}_0\rangle = \begin{cases} A + BI_z & \text{for} \quad \boldsymbol{\sigma}_0 \text{ up}, \quad \boldsymbol{\sigma}_1 \text{ up}, \\ A - BI_z & \text{for} \quad \boldsymbol{\sigma}_0 \text{ down}, \quad \boldsymbol{\sigma}_1 \text{ down}, \\ B(I_x + \mathrm{i}I_y) & \text{for} \quad \boldsymbol{\sigma}_0 \text{ up}, \quad \boldsymbol{\sigma}_1 \text{ down}, \\ B(I_x - \mathrm{i}I_y) & \text{for} \quad \boldsymbol{\sigma}_0 \text{ down}, \quad \boldsymbol{\sigma}_1 \text{ up}. \end{cases} \tag{A.35}$$

We used I_x, I_y and I_z to denote the cartesian spin components of the nucleus. When a scattering experiment is repeated, each of these components average to zero as the spin of the nucleus is initially independent from the neutron spin. Thus we find that the coherent scattering cross section (which is equal to the square of the average scattering length) is for non spin-flip transitions

$$\sigma_{coh,\,nsf} = 4\pi A^2 = \sigma_{coh} \tag{A.36}$$

and in the case that the spin of the neutron is flipped

$$\sigma_{coh,\,sf} = 0. \tag{A.37}$$

The incoherent cross section, $4\pi[\langle b^2\rangle - \langle b\rangle^2]$, can be found in the same way and reads when the spin is not flipped

$$\sigma_{inc,\ nsf} = 4\pi\tfrac{1}{3}B^2 I(I+1) = \tfrac{1}{3}\sigma_{inc} \qquad (A.38)$$

and

$$\sigma_{inc,\ sf} = 4\pi\tfrac{2}{3}B^2 I(I+1) = \tfrac{2}{3}\sigma_{inc} \qquad (A.39)$$

for spin-flip transitions.

Rotational states of a hydrogen molecule

Due to its diatomic nature, hydrogen can rotate around two axes. The possible energies E_J of the rotation of the hydrogen molecule are quantized by integer values of the angular momentum J. Each value of J has $2J+1$ levels with the quantum number m_J. For a hydrogen molecule that is free to rotate, the energies of the rotational levels are given by $E_J = J(J+1)B$. From the experimental value of B, (7.35 meV) [47], we can evaluate the difference between the two lowest rotational states ($J = 0$ and $J = 1$): 14.7 meV (or, equivalently, $\approx$170 K). We note that the $2J + 1$–fold degeneracy is lifted when the molecule is in an environment that is not centro-symmetric, a fact that is used in this thesis to characterize hydrogen molecules that are adsorbed on carbon surfaces.

Because the two protons in a H_2-molecule are fermions, their overall wavefunction should be anti-symmetric under exchange of the two nuclei. Rotational states with even values of J, have a symmetric spatial eigenfunction and the spin eigenfunction needs to be antisymmetric to achieve an overall antisymmetric wavefunction. This antisymmetric spin eigenfunction is a singlet spin state with nuclear spin 0. Odd values of J have an antisymmetric spatial eigenfunction, and conversely a symmetric spin part of the wavefunction (a triplet state with nuclear spin 1). Hydrogen in rotational states with odd values of J is called ortho-hydrogen, whereas hydrogen in rotational states with even values of J is denoted para-hydrogen. At high temperatures (e.g. room temperature) the ratio of ortho- to para-hydrogen molecules is 3 to 1.

The hydrogen molecule as a scatterer

We denote the positions of the protons indexed $p = 1, 2$ in a hydrogen molecule by:

$$\mathbf{R}_i = (-1)^n \tfrac{1}{2}\mathbf{d}, \qquad (A.40)$$

where the origin is chosen in the center of the molecule and $\mathbf{d}$ points from proton 1 to 2. We assume for the moment that the center of mass of hydrogen molecule is fixed in space. The total spin K of the two protons in state $\mathbf{K}$ can again be formed by a singlet and by a triplet state of the protons. When the neutron interacts with

the hydrogen molecule, i.e. with both protons,[1] the differential cross section for the process $0 \rightarrow 1$ reads:

$$\left(\frac{\mathrm{d}^2\sigma}{\mathrm{d}\Omega\,\mathrm{d}E_1}\right)_{0\to1} = \frac{|\mathbf{k}_1|}{|\mathbf{k}_0|}\left|\langle\boldsymbol{\sigma}_1\mathbf{K}_1\mathbf{J}_1|\sum_{p=1,2}\hat{b}_p\,\mathrm{e}^{\mathrm{i}(-1)^p\frac{1}{2}\mathbf{Q}\cdot\mathbf{d}}|\boldsymbol{\sigma}_0\mathbf{K}_0\mathbf{J}_0\rangle\right|^2, \qquad (A.41)$$

where we have included the initial and final rotational states $\mathbf{J}_0$ and $\mathbf{J}_1$. If the initial and final states are both symmetric or both antisymmetric with respect to a exchange of the labels of two protons,

$$\sum_{p=1,2}\hat{b}_p\,\mathrm{e}^{\mathrm{i}(-1)^p\frac{1}{2}\mathbf{Q}\cdot\mathbf{d}} = \sum_{p=1,2}\hat{b}_p\,\mathrm{e}^{-\mathrm{i}(-1)^p\frac{1}{2}\mathbf{Q}\cdot\mathbf{d}}, \qquad (A.42)$$

which means that we can write equation A.41 as:

$$\left(\frac{\mathrm{d}^2\sigma}{\mathrm{d}\Omega\,\mathrm{d}E_1}\right)_{0\to1} = \frac{|\mathbf{k}_1|}{|\mathbf{k}_0|}\left|\langle\boldsymbol{\sigma}_1\mathbf{K}_1|\hat{b}_1+\hat{b}_2|\boldsymbol{\sigma}_0\mathbf{K}_0\rangle\langle\mathbf{J}_1|\cos(\tfrac{1}{2}\mathbf{Q}\cdot\mathbf{d})|\mathbf{J}_0\rangle\right|^2. \qquad (A.43)$$

Using the definition of the scattering length operator in equation A.31 we find:

$$\langle\mathbf{K}_1|\hat{b}_1+\hat{b}_2|\mathbf{K}_0\rangle = \langle\mathbf{K}_1|2A + B\boldsymbol{\sigma}\cdot\mathbf{K}|\mathbf{K}_0\rangle. \qquad (A.44)$$

Since A is zero when the initial and final states of the nuclear spin are different and because we assumed equal nuclear symmetry before and after the event, this expression is applicable when

$$\Delta K = 0, \quad |\Delta J| = 0, 2, \ldots \qquad (A.45)$$

and by a summation over the levels with nuclear spin K_1, we find

$$\left(\frac{\mathrm{d}^2\sigma}{\mathrm{d}\Omega\,\mathrm{d}E_1}\right)_{0\to1} = \frac{|\mathbf{k}_1|}{|\mathbf{k}_0|}[4A^2 + B^2K_0(K_0+1)]\left|\langle\mathbf{J}_1|\cos(\tfrac{1}{2}\mathbf{Q}\cdot\mathbf{d})|\mathbf{J}_0\rangle\right|^2. \qquad (A.46)$$

We can interpret this as a effective scattering cross section for such a process, $4A^2 + B^2K_0(K_0+1)$, multiplied by a factor that is determined by the shape of the diatomic hydrogen molecule (similar to the Debye-Waller factor). We can write this scattering cross section as a sum of coherent and incoherent parts: $\sigma_{coh} = 4\pi A^2$ and $\sigma_{inc} = 4\pi B^2K_0(K_0+1)$.

In the situation that the nuclear wave-function changes from symmetric to antisymmetric or vice versa, i.e.

$$|\Delta K| = 1, \quad |\Delta J| = 1, 3, \ldots, \qquad (A.47)$$

---

[1]For deep inelastic scattering (very large energy transfers), the neutron again probes the two proton apart. The energy transfer where this happens depends on the binding of the two protons in the hydrogen molecule [115].

we get the following expression:

$$\left(\frac{\mathrm{d}^2\sigma}{\mathrm{d}\Omega\,\mathrm{d}E_1}\right)_{0\to1} = \frac{|\mathbf{k}_1|}{|\mathbf{k}_0|}\frac{\sigma_{inc}}{\pi}[1-\tfrac{1}{3}K_0(K_0+1)]\,\left|\langle\boldsymbol{\sigma}_1\mathbf{K}_1\mathbf{J}_1|\sin(\tfrac{1}{2}\mathbf{Q}\cdot\mathbf{d})|\boldsymbol{\sigma}_0\mathbf{K}_0\mathbf{J}_0\rangle\right|^2, \quad \text{(A.48)}$$

where again $\sigma_{inc} = 4\pi B^2 K_0(K_0+1)$.

A full derivation of these expressions can be found in the articles of Young and Koppel [116] and Sears [117] and in Lovesey's theory of neutron scattering from condensed matter [114]. In the case of the process $J_0 = 0 \to J_1 = 0$ the scattering is only coherent as $K_0 = 0$. If we now take the scattering function of the hydrogen molecule $S(\mathbf{Q},\omega)$ into account, the double differential cross section reads [118]:

$$\left(\frac{\mathrm{d}^2\sigma}{\mathrm{d}\Omega\,\mathrm{d}E_1}\right) = N\frac{|\mathbf{k}_1|}{|\mathbf{k}_0|}\frac{\hbar}{\pi}\sigma_{coh}\,j_0^2(\tfrac{1}{2}|\mathbf{Q}|\,|\mathbf{d}|)\,S(\mathbf{Q},\omega), \quad \text{(A.49)}$$

where $\sigma_{coh} = 1.77$ barn, N is the number of hydrogen molecules, $j_0^2(\tfrac{1}{2}|\mathbf{Q}|\,|\mathbf{d}|)$ is the zeroth spherical Bessel function and $S(\mathbf{Q},\omega)$ is the scattering function of the hydrogen molecules. In the case of the transition from para to ortho hydrogen, $J_0 = 0 \to J_1 = 1$ (and from $K_0 = 0$ to $K_1 = 1$), the incoherent scattering is:

$$\left(\frac{\mathrm{d}^2\sigma}{\mathrm{d}\Omega\,\mathrm{d}E_1}\right) = N\frac{|\mathbf{k}_1|}{|\mathbf{k}_0|}\frac{\hbar}{\pi}\,3\sigma_{inc}\,j_1^2(\tfrac{1}{2}|\mathbf{Q}|\,|\mathbf{d}|)\,S_i(\mathbf{Q},\omega-\Delta E/\hbar), \quad \text{(A.50)}$$

where we use $\sigma_{inc} = 78.8$ barn, the first order spherical Bessel function $j_1^2(\tfrac{1}{2}|\mathbf{Q}|\,|\mathbf{d}|)$ and the incoherent scattering function $S_i(\mathbf{Q},\omega)$ with a correction to the energy ω due to the excitation of the first rotational level at $\Delta E = 14.7$ meV. The factor $3\sigma_{inc}$ arises from the fact that we scatter to the triple degenerated state $J = 1$, $K_1 = 1$. We see that a sample containing para hydrogen molecules (i.e. at low temperature) scatters only coherently with a very small cross section for neutron energies below the excitation energy of 14.7 meV. When the neutron energy comes above this excitation energy, the cross section becomes very large and almost completely incoherent.

A.2 Calculation methods

To calculate microscopic properties of matter, such as stability of compounds, bond lengths and strengths, diffusion coefficients and reaction paths, several methods have been developed, some of which we describe briefly below. We pay short notice to empirical (or force-field) methods, describe the Hartree-Fock method briefly as this has much in common with Density Functional Theory, that we introduce afterwards. A more elaborate discussion of these methods can be found elsewhere [119, 120, 121].

A.2.1 Empirical methods

Using simple models of harmonic potentials, electrostatic interactions, and dispersion forces, empirical methods allow for basic comparisons of energies and for geometry optimizations. Empirical methods are usually very useful and fast, compared

to rigorous quantum calculations. In principle, these approaches are not able to model chemical reactions and bond forming or breaking since the electronic structure of the system does not enter these models. For distorted, uncommon bonding situations these empirical methods produce unreliable results. We have tried this empirical method for hydrogen in magnesium metal. The results, however were unphysical as the hydrogen atom in the metal showed very little interaction with the magnesium atoms in the sample. We therefore used the *ab initio* density functional theory method to calculate properties of the metal-hydrogen system.

A.2.2   *Ab initio* methods

Ab initio methods predict properties of physical systems starting from the positions and types of the atoms. In principle no adjustable parameters are used in the calculation method, although in practice still a considerable number of choices has to be made. The desired properties are then found by evaluating the laws of nature as far as they are known and are implemented in the method. *Ab initio* methods are regarded to be especially suited for the simulation of uncommon systems or properties. In these methods, it is generally assumed that the electrons adjust their positions (i.e. wavefunctions or density distribution) instantaneously (known as the Born-Oppenheimer approximation [122]) to the motion of the nuclei. The atoms are regarded to be static (the nuclei provide the potential landscape for the electrons) during a calculation step and the state of the system is described by the time independent Schrödinger equation in eigenvalue formulation:

$$\hat{H}\Psi = E\Psi, \tag{A.51}$$

where $\hat{H}$ is the hamiltonian of the system expressed as a quantum mechanical operator, E is the energy of the wavefunction Ψ that describes the system. As an exact solution is only available for very small systems such as the hydrogen nucleus with one electron, we need approximations to solve Schrödingers equation for basically every other system that is larger than this.

A.2.3   Hartree-Fock method

In the Hartree-Fock method, the wavefunction of the total system is assumed to consist of a product of N one-electron wavefunctions $\psi(\mathbf{r})$:

$$\Psi = \psi_1(\mathbf{r}_1)\psi_2(\mathbf{r}_2)\cdots\psi_N(\mathbf{r}_N). \tag{A.52}$$

This means effectively that all electrons are treated as being independent from each other. In reality the electrons do not only feel the potential due to the nuclei, but also have mutual Coulomb and exchange interactions, the latter being imposed by the Pauli exclusion principle. Since this implies that $N!$ interactions have to be evaluated, in Hartree-Fock theory these interactions are described by the interaction of

every electron with the averaged electron density $\rho(\mathbf{r})$. Since electrons are fermions, the total wavefunction should be antisymmetric on exchange of two electrons. This is achieved by the construction of the Slater determinant where the matrix element on row i and column j is given by $\psi_j(\mathbf{r}_i)$. The inclusion of the exchange by means of the Slater determinant also introduces exchange integrals which are a function of two one-electron wavefunctions and the distance between the electrons. The variational principle stating that the wavefunction with the lowest energy is also the exact ground state wavefunction, is applied to find the lowest energy state of the system. The Schrödinger equation has now been reduced to a set of one-electron equations which can be solved numerically for a discrete set of positions or continuously using a finite set of basis functions, such as molecular orbitals or gaussians.

A.2.4 Density Functional Theory

Density Functional Theory (DFT) uses a functional that acts on the electronic density of a atomic system to evaluate the energy. Hohenberg and Kohn [123] proved that for a non-degenerate quantum system there exists a functional that gives the energy of a given configuration and takes the electron density $\rho(\mathbf{r})$ as its input. They also showed that the energy functional $E[\rho]$ of the electron density $\rho(\mathbf{r})$ is minimal for the ground state density. When one knows this functional, the ground state energies can be calculated using an iterative approach. The advantage of the density functional theory lies in the fact that the wavefunction Ψ is a function of the $3N$ positions of all electrons, whereas the electronic density is a function of the three space-coordinates only and the evaluation can therefore be much quicker. The theorem of Hohenberg and Kohn is an existence proof of the density functional, but there is no prescription how to construct it. It is necessary to use approximations regarding the parts of the functional that deal with kinetic energy, exchange and correlation energies of the system of electrons.

The functional can be written as the sum of the kinetic energy part T, a potential energy part V taking the Coulomb interactions between electrons and the nuclei and between the electrons themselves into account and finally an exchange-correlation energy part U that captures all many-body interactions:

$$E[\rho] = T[\rho] + V[\rho] + U[\rho]. \tag{A.53}$$

Unfortunately it is not known how the kinetic T energy part can be evaluated from the electron density $\rho(\mathbf{r})$. Kohn and Sham [124] therefore proposed the following form of the functional:

$$E[\rho] = T_{ni}[\psi_i] + V[\rho] + U[\rho] + E_{xc}[\rho], \tag{A.54}$$

where T_{ni} is the kinetic energy of a set of one-electron wavefunctions $\psi(\mathbf{r})$, chosen such that the resulting density $\rho_{KS}(\mathbf{r})$ is equal to the density $\rho(\mathbf{r})$ that has to be calculated:

$$\rho(\mathbf{r}) = \rho_{KS}(\mathbf{r}) = \sum_i |\psi_i(\mathbf{r}_i)|^2. \tag{A.55}$$

The terms V and U can easily be expressed as a sum of Coulomb expressions by integrating over the electron density. The electrostatic interactions between the nuclei, which is constant given a certain conformation of the nuclei, may be accounted for in the term V. The exchange-correlation functional part contains all contributions to the energy that are not accounted for by the other terms.

Various approximations have been published to the exchange-correlation functional, like the local density approximation (LDA) and the generalized gradient approximation (GGA) [121]. The local density approximation assumes that the exchange-correlation potential at point $\mathbf{r}$ is equal to the exchange-correlation potential of an homogeneous electron gas with a constant density $\rho(\mathbf{r})$. Generally, the use of generalized gradient methods, which also take the gradient in the density into account, does not improve the results significantly.

The problem is now reduced to a set of one-electron equations, similar to the Hartree-Fock equations. Several methods exist to solve these equations using plane waves, projector augmented waves, gaussian functions, molecular orbitals or other functions as basis sets. Plane waves such as used by the VASP package [101] are the natural choice for periodic boundary conditions that are found in most solid state problems. However, the cusps in the electron density at the place of the nuclei are difficult to describe by plane waves as many of them are needed, which can be overcome by the use of adjusted nuclear pseudopotentials [121] or projector-augmented wave (PAW) potentials [125, 126, 127].

Using Bloch's theorem each electronic wavefunction can be written as the product of a plane wave and a cell-periodic part [121]. Since the latter is a sum of plane waves we get

$$\psi_i = e^{i\mathbf{k}\cdot\mathbf{r}} \sum_{\mathbf{G}} c_{i,\mathbf{G}}\, e^{i\mathbf{G}\cdot\mathbf{r}} = \sum_{\mathbf{G}} c_{i,\mathbf{k}+\mathbf{G}}\, e^{i(\mathbf{k}+\mathbf{G})\cdot\mathbf{r}}, \qquad (A.56)$$

where $\mathbf{G}$ denotes the set of reciprocal lattice vectors, $c_{i,\mathbf{k}+\mathbf{G}}$ are the plane wave coefficients and $\mathbf{k}$ is the wavevector of the Bloch plane wave. In a periodic calculation the number and position in the reciprocal unit cell of the $\mathbf{k}$-points is important for the accuracy of the calculation. The number of $\mathbf{k}$-points can be reduced when we use a smearing method to take the partial occupancies of the states near the Fermi surface into account. For metals the method of Methfessel and Paxton [128] is used. The smearing parameter SIGMA that is used by VASP needs to be chosen carefully. If SIGMA is taken to large, the smearing is unphysical and the energy turns out wrong even for very dense $\mathbf{k}$-point meshes. On the other hand, a small value for SIGMA makes many $\mathbf{k}$-points necessary. The program VASP that we used for the calculations described in this thesis produces estimates for the entropy contribution in the results, which is the difference between the energy and the free energy. This entropy contribution should be minimal (i.e. smaller than 1 meV per atom) for accurate results [108]. We found that in the case of the magnesium metal supercell (36 magnesium atoms and 1 hydrogen), we had to chose $2 \times 2 \times 2$ $\mathbf{k}$-points and a value for the smearing parameter SIGMA=0.2 eV to fulfill this criterion.

The advantage of DFT over the Hartree-Fock method is that all 'difficult' terms

are taken into an effective potential in DFT which is the same for every electron, whereas in the case of the Hartree-Fock method the effective potential differs from electron to electron. Thus one can imagine that the DFT calculations are much faster. Despite the fact that the exact form of the density functional in unknown and that no converging recipe is known to improve them, DFT calculations are widely used as they predict physical quantities remarkably well using limited computing resources. The energy of a conformation of the nuclei is calculated by performing a self-consistent iteration procedure of finding a density and evaluating the energy. The functional changes every step as it is dependent on the density itself. The new density can be found by several minimization schemes such as the method of the steepest descend or the conjugate-gradient method [121]. When the energy changes are below a given limits, this procedure is considered to be finished.

A.2.5 Moving the ions: vibrational frequencies and molecular dynamics

Up to now the positions of the ions were fixed, which is a consequence of the Born-Oppenheimer approximation. We can approximate the movements of nuclei by a series of such static calculations, each with a different set of positions of the ions. If we want to relax a given structure, calculate vibrational frequencies or simulate a dynamical system in time, forces according to the Hellmann-Feynman theorem [121] are used. This theorem states that the force $\mathbf{f}_I$ on the ion I, defined as the derivative of the energy to a position $\mathbf{R}_I$ of the ion, is characterized by the partial derivative only:

$$\mathbf{f}_I = -\frac{\mathrm{d}E}{\mathrm{d}\mathbf{R}_I} = -\frac{\partial E}{\partial \mathbf{R}_I}, \tag{A.57}$$

and the partial derivatives of the sum of one-electron wavefunctions to the position of the ion, $\sum_i \partial \psi_i / \partial \mathbf{R}_I$ and $\sum_i \partial \psi_i^* / \partial \mathbf{R}_I$ vanish. The Hellmann-Feynman forces are used in this thesis to calculate the vibrational spectrum of magnesium hydride and to perform a molecular dynamics simulation of a hydrogen atom in magnesium metal.

In the first case the atoms in the asymmetric unit cell are displaced by a fixed, small amount in the three cartesian directions. In the harmonic approximation (it is assumed that the forces are proportional to the displacements), the vibrational frequencies can then be evaluated using a projection of the motions onto a normal coordinate system. When the motions in adjacent unit cells are correlated, which is clearly the case for solids, a full phonon calculation is necessary. Such a calculation can be performed using the PHONON program of Parlinski [102]. We then need to calculate the Hellmann-Feynman forces for a supercell that is large enough to make sure that the effective range of the forces are smaller than the supercell size. For crystals of uncharged, organic molecules, the effective range of interaction typically has a radius of ≈ 5 Å. Since DFT methods scale in computational time with the third power of the number of atoms, the super cell calculations are considerably longer

than single cell calculations. The program PHONON gives the full dispersion curves of all phonon branches in the crystal on the basis of the forces and the symmetry in the super cell.

Secondly, for molecular dynamics simulations a constant time-step is used between successive evaluations of the total energy of the system. The displacements and velocities of the ions are adjusted according to the laws of classical mechanics. The time step needs to be chosen such that the self-consistent convergence is achieved in a few iterations. We found that the magnesium metal-hydrogen system converged in 2–3 iterations when a time step of 1 fs was used. The simulation is run at a predefined temperature by means of an algorithm which scales the velocities of all atoms at every time-step such that the kinetic energy distribution of the ions resembles the given temperature.

A.2.6 Diffusion coefficients

The trajectory that the hydrogen atom followed during the molecular dynamical simulation, can be used to evaluate the diffusion coefficient. The tracer diffusion coefficient (we follow a single particle: the tracer particle) D is given by the following expression [129]:

$$D = \lim_{t \to \infty} \left[\frac{1}{2dt} \frac{1}{N} \sum_{i=1}^{N} [\mathbf{r}_i(t)]^2 \right], \qquad (A.58)$$

where t is the total simulation time, d is the dimensionality, $i = 1 \ldots N$ is the index to the repetition number of the simulation and $\mathbf{r}_i(t)$ is the position of the diffusing particle at time t and simulation run i with respect to the starting point $\mathbf{r}_i(0) = 0$ for all i. In practice this expression has to be approximated, especially when one has to use calculations on large super cells that run slow even on fast computers. The following expression is an approximation to the diffusion coefficient when only one simulation run is available:

$$D \simeq \frac{1}{N_t} \sum_{j=1}^{N_t} \frac{|\mathbf{r}_j - \mathbf{r}_{ref}|^2}{2 \, d \, j \, \mathrm{d}t}, \qquad (A.59)$$

where we now sum over the number of time-steps $j = 1 \ldots N_t$ each having a length in time of $\mathrm{d}t$. The reference position vector $\mathbf{r}_{ref}$ is part of the trajectory. We found that the most reliable results are obtained when we average the diffusion coefficients obtained with $\mathbf{r}_{ref}$ respectively at the start ($\mathbf{r}_{ref} = \mathbf{r}_1$) and the end point ($\mathbf{r}_{ref} = \mathbf{r}_{N_t}$) of the simulated trajectory.

We note that normally a macroscopic and microscopic diffusion coefficients are distinguished. The macroscopic or chemical diffusion coefficient is used in Fick's law of diffusion which states that the flux $\mathbf{J}$ is directly proportional to the macroscopic diffusion coefficient D_m times a volumetric concentration gradient ∇C:

$$\mathbf{J} = -D_m \nabla C. \qquad (A.60)$$

Since the transport is strictly speaking not proportional to the concentration gradient, but rather to a gradient in the chemical potential, a microscopic or jump diffusion coefficient is also defined. It is no surprise that one determines the macroscopic diffusion coefficient with macroscopic techniques such as conductivity measurements and the microscopic diffusion coefficient with microscopic techniques like inelastic neutron scattering or molecular dynamical simulations. The two diffusion coefficients are connected by a thermodynamic factor θ

$$\theta = \frac{\partial(\mu/kT)}{\partial \ln x}, \tag{A.61}$$

where μ/kT is the chemical potential relative to the absolute temperature kT and x is the molar concentration of the diffusing particles. When the chemical potential of the diffusing particles can be written as $\mu = \mu^0 + kT \ln(x)$ (this ideal–solution chemical potential is found for very low concentrations), the thermodynamic factor is equal to unity which is clearly the case for hydrogen in the metal α–phase (see the discussion in the thermodynamic assessment of the magnesium-hydrogen system by Zeng et al. [104]).

Appendix B

Hydrogen adsorption in carbon nanostructures compared: nanotubes, fibres and coals

Abstract

Single walled carbon nanotubes (SWNT) were reported to have record high hydrogen storage capacities at room temperature, indicating an interaction between hydrogen and carbon matrix which is stronger than known before. Here we present a study of the interaction of hydrogen with activated charcoal, carbon nanofibers and SWNT, that disproves these earlier reports. The hydrogen storage capacity of these materials correlates with the surface area of the material, with the activated charcoal having the largest. The SWNT appear to have a relatively low accessible surface area due to bundling of the tubes; the hydrogen does not enter the voids between the tubes in the bundles. Pressure-temperature curves were used to estimate the interaction potential, which was found to be 580 ± 60 K. Hydrogen gas was adsorbed in amounts up to 2 wt.% only at low temperatures. Molecular rotations observed with neutron scattering indicate that molecular hydrogen is present, and no significant difference was found between the hydrogen molecules adsorbed in the different investigated materials. Results from Density Functional Theory computer calculations show molecular hydrogen bonding to an aromatic C-C bond that is present in the materials investigated. The claims of high storage capacities of SWNT related to their characteristic morphology are unjustified.

B.1   Introduction

The importance of hydrogen as a future energy carrier is generally acknowledged. The advantages of a hydrogen-based economy would be its sustainable and envi-

ronmentally friendly character. Apart from factors concerning the energy efficient production of hydrogen as well as cost effective use of hydrogen in fuel cells, the application of hydrogen as an energy carrier is limited by hydrogen storage problems. Storage of hydrogen is either too expensive, too heavy, takes too much volume and/or is unsafe. Therefore hydrogen storage in new materials and devices is an active field for research world wide. Storage of hydrogen in new forms of carbon materials attracted world wide interest when Dillon et al. published 5-10 wt% hydrogen storage in single walled carbon nanotubes (SWNT) [18]. Subsequently claims of high hydrogen storage capacities at room temperature and pressures higher than 100 bar in graphitic nanofibers (GNF) and lithium and potassium doped multi walled carbon nanotubes were made [19, 20, 21]. However, more recently several reports that falsify these claims have appeared [29, 30, 31, 32]. Despite considerable effort, computations do not support those high storage capacities on the basis of physisorption processes [22, 23, 24, 25, 26, 27, 28].

Recently we reported adsorption capacities in the range 0-2.5 wt% at low temperatures and ambient pressure in various nanostructured carbon samples [16]. The process responsible for storage under the low-temperature ambient-pressure conditions is clearly physisorption.[1] An important yet unanswered question is how the strength of the interaction resulting in physisorption varies between carbon based materials with different topologies. In this paper we report on a study of the interactions between hydrogen and different carbon materials ranging from activated charcoal to single walled carbon nanotubes. In our measurements the rotation of a hydrogen molecule is used as a sensitive probe for the presence of the molecule and for interactions between surface and adsorbed hydrogen molecules at the microscopic/molecular level. These results are compared to macroscopic adsorption measurements as well as first-principles calculations.

B.2 Experimental section

Four different materials have been investigated in this study: Two activated carbons: AC Norit 990293 (NAC) and AC Norit GSX (GSX), a 'fishbone' carbon nano-fibre sample (GNF) and a sample consisting of single walled carbon nanotubes (SWNT). Activated carbons are highly micro- and mesoporous carbon materials. Steam-activated carbons have been prepared from raw materials (e.g. peat, lignite, coal) and carbonized and reacted with steam at 1000 degrees Celsius. In this way some of the carbon atoms are removed by gasification, which yields a very porous structure.

Graphitic nanofibers were grown using a fixed bed reactor. Nickel particles on a silica support (Aerosil 200) dissociate methane, forming hydrogen and carbon atoms that dissolve in the nickel particle. These carbon atoms diffuse through the nickel catalyst particle to form a carbon nanofiber. The silica support was removed in a

---

[1]The energy of adsorption is defined to be smaller than 4000K for physisorption [130]. If the energy of adsorption is greater than 4000 K the molecule forms chemical bonds

refluxed boiling KOH solution. In the same manner a treatment with HNO_3 was used to remove the Ni particles [131]. The nanofibers used in this investigation had a fishbone arrangement of the graphite planes with respect to the fiber axis. The diameter of these fibers ranges between 20 and 30 nm, with an average of 25 nm. We loaded these fishbone fibers with 0.2 wt% Pd nanoparticles using ion-exchange from a $Pd(NH_3)_4Cl_2$ solution [132]. This was done in order to open up the possibility to have atomic H in the sample, that may possibly even intercalate in between the graphite layers as has been speculated by others [19, 20, 21].

The single walled carbon nanotubes were obtained commercially (from Carbon Nanotechnologies Incorporated, Houston, USA). The nanotubes were produced by the HiPCo process in which $Fe(CO)_5$ decomposes in a CO atmosphere [133]. Our sample contains 17.5 wt% or less than 5 at% of leftover iron catalyst particles. The sample was characterized by X-ray diffraction, which showed no sharp peaks, indicating that no crystalline form of graphite or iron was present. Mössbauer spectroscopy revealed that the left-over catalyst particles are almost exclusively present in the form of Fe_3C. Transmission electron microscopy was used to investigate the diameter of the nanotubes and the iron carbide particles. The carbon nanotubes are packed with a smallest repetition distance of about 1.25 nm, indicating that the size of the tubes is around 1.25 nm, whereas the iron carbide particles are larger, with diameters up to 4 nm. The surface area of the relatively low number of massive iron carbide particles is much smaller than that of the nanotubes, and any adsorption of H_2 on these particles can therefore not be observed.

Adsorption measurements

Samples were loaded in aluminum containers and mounted in a closed cycle refrigerator. The samples were evacuated to below 1 mPa while heated to 323 K for at least 12 hours. Adsorption isotherms were recorded by opening a valve to a known volume of hydrogen gas with a known pressure, waiting for equilibrium and measuring the pressure, and repeating this procedure up to 1 bar. Temperature-pressure curves were measured inside the same system.

Inelastic neutron scattering

The samples under investigation were loaded in aluminum sample chambers, mounted into a cryogenic system and evacuated to below 1 mPa while heated to 323 K for at least 12 hours. The sample thickness was such that up to 10% of the neutrons was scattered by the nuclei of the sample when hydrogen was loaded. The samples were cooled to 3.6 K and a background measurement was performed on the evacuated sample. Then the sample was heated to 77 K and hydrogen was loaded up to a pressure of 1 bar. This temperature and pressure were chosen because these are the reference conditions in our previous work. When insufficient hydrogen had been adsorbed for a good neutron spectrum, filling was continued at 1 bar at a temperature

that was lowered by a few degrees (this enhances the adsorption capacity considerably). In this manner 100-200 ml STP H_2 was adsorbed in the sample, sufficient for recording an accurate neutron spectrum in a reasonable time. The hydrogen loaded sample was then cooled down to 3.6 K and a spectrum was recorded. Note that we can exclude the possibility of having measured on solid hydrogen because the hydrogen adsorbs already completely at 50 K (i.e. the hydrogen vapor pressure is always much lower than the equilibrium vapor pressure for liquid or solid hydrogen).

The measurements were performed on the time-of-flight spectrometer RKS at the 2 MW nuclear reactor in Delft, the Netherlands. This spectrometer uses two choppers and a rotating pyrolitic graphite monochromator to produce a pulsed, mono-energetic beam. The incident energy of the neutron beam was selected to be 157.3 cm^{-1}. The scattered neutrons are detected by an array of detectors giving a momentum transfer range of 0.2-3.5 Å^{-1} and their arrival time is recorded. The time-of-flight of the neutrons were transformed into energies and the structure factor $S(Q,\omega)$ was obtained by multiplying with k_i/k_f and by normalizing on the incident beam monitor. In order to improve statistics the spectra were summed over the momentum transfer Q so that the average value of the spectra is 1.6 Å. Scattering of the sample without hydrogen was subtracted from the spectrum of the hydrogen-loaded sample. In order to extract not too much of the 'empty sample spectrum', corrections were made for the small screening of the scattering of the sample holder and carbon sample by the hydrogen in the loaded sample. In this way only the scattering of hydrogen is visible in the corrected spectra. All experiments were performed at a temperature of 3.6 K. These low temperatures are needed because at higher temperatures the thermal energy of the hydrogen molecules appears to enable them to move along the surface, giving unwanted broadening of the spectra.

In order to be able to observe a possible decrease in elastic scattering with time, each spectrum was divided into 5-10 sub-runs. Such decrease in elastic scattering could result from the slow conversion of ortho- to para-hydrogen because ortho-hydrogen scatters approximately 40 times more than para-hydrogen (see below for explanation).

Theoretical calculations

In order to understand the experimental results we performed computer calculations by means of Density Functional Theory, using Dmol[3]. We used the numerical basis set DND (double numerical with d functions) and the Perdew Wang local correlation density functional.

B.3 The hydrogen molecule as a probe.

Due to its diatomic nature, hydrogen can rotate around two axes. The possible energies E_J of the rotation of the hydrogen molecule are quantized and are labelled by the rotational quantum number J. For a hydrogen molecule that is free to rotate

(this is in good approximation the case in solid hydrogen [47]) the energies of the rotational levels are given by $E_J = J(J+1)B$. The rotational constant B, can be evaluated with formula (refeq:Ba) [47] in which $\hbar$ is Planck's constant divided by 2π, m_p is the mass of the protons and R is the distance between the protons.

$$B = \frac{2\hbar^2}{m_p R^2} \; , \qquad\qquad\qquad (B.1)$$

From the experimental value of B, 59.3 cm^{-1} (7.35 meV) [47], we can evaluate the difference between the two lowest rotational states ($J = 0$ and $J = 1$): 119 cm^{-1} (or $\approx$170 K). It is important to note here that the rotational transition only occurs for molecular hydrogen, i.e. atomic hydrogen bonded to a carbon plane does not show this transition.

Because the two protons in a H$_2$-molecule are fermions, their overall wavefunction should be anti-symmetric under exchange of the two nuclei. Rotational states with even values of J, have a symmetric spatial eigenfunction and the spin eigenfunction needs to be antisymmetric to achieve an overall antisymmetric wavefunction. This antisymmetric spin eigenfunction is a singlet spin state with nuclear spin 0. Odd values of J have an antisymmetric spatial eigenfunction, and conversely a symmetric spin part of the wavefunction (a triplet state with nuclear spin 1). Hydrogen in rotational states with odd values of J is called ortho-hydrogen, whereas hydrogen in rotational states with even values of J is denoted para-hydrogen. At high temperatures (e.g. room temperature) the ratio of ortho- to para-hydrogen molecules is 3 to 1. At temperatures much lower than 170 K the lowest rotational state $J = 0$ is energetically favorable. However the conversion from ortho- to para-hydrogen can be extremely slow because it involves a change of the total nuclear spin from 1 to 0. The presence of paramagnetic catalysts or impurities as in our samples can speed up the conversion from days to less than hours. The neutron cross-section of ortho and para hydrogen are rather different (ortho: 80 barn/molecule, para: 1.8 barn/molecule). Care should be taken in the experiment to observe if the ortho-para conversion is complete or not. It may also be noted that atomic hydrogen has a large cross section (80 barn/atom).

When a hydrogen molecule is adsorbed on a surface or in a cavity, the potential it feels may not be isotropic because of the atomic nature of any surface, and this may hinder the rotation of the adsorbed hydrogen molecule. Then spherical symmetry is broken, causing the triplet $J = 1$-level to split. Such splitting contains information on the symmetry of the site at which hydrogen is adsorbed. An example was observed by e.g. Fitzgerald et al. for hydrogen molecules in interstitial sites in solid C$_{60}$ [48].

If the molecular hydrogen electron cloud is severely altered because it takes part in a bond with the surface, the distance between the protons increases due to reduced electronic screening. (This H-H bond lengthening effect is also known as bond activation [49].) This leads to a smaller value of the rotational constant B (see eq. (B.1)). Such effects of bond elongation were illustrated by Eckert and co-

workers with experiments on different metal-complexes having a dihydrogen ligand (the so-called Kubas-compounds). They found that the separation of the lowest two rotational levels of the dihydrogen ligand is smaller in complexes where the dihydrogen ligand molecule was more tightly bound, and the larger proton-proton bond lengths found in this way were confirmed by neutron diffraction [49].

For weakly bonded molecules, as is the case in physisorption by van der Waals interaction, no significant electron density is transferred to the adsorbent or is used to form the bond. Thus it is not expected that large shifts of the rotational constant B will occur. The hydrogen molecules can then be described as (almost) free quantum mechanical rotors. In contrast, for more strongly bound chemisorbed molecular hydrogen in e.g. zeolites a strong shift of the $J = 1$ level can be observed [52].

With the neutron experiments presented here we are able to discriminate between molecular and atomic hydrogen on the basis of the presence of the rotational transition and the strongly different neutron scattering cross sections. Furthermore under the assumption that the rotational level may be stronger split for stronger bound hydrogen, the value of the splitting gives an indication of the strength of the bond experienced by the hydrogen molecule. This should then also be in agreement with the adsorption energy found from the adsorption measurements. These methods will provide a means to investigate if the high storage capacity claims for carbon nanofibers and carbon nanotubes can be supported or not by a hydrogen-matrix interaction that is much stronger or of a different nature than found in other graphites.

B.4   Experimental results

B.4.1   Pressure and temperature dependent hydrogen adsorption

All of these samples were tested for hydrogen storage capacity at 77 K and 1 bar. For the SWNT this was the first time we determined this, while for the other compounds the adsorbed amounts (obtained volumetrically) under these conditions were the same as we found previously [16]. Figure B.1 shows the amount of adsorbed hydrogen as a function of hydrogen pressure for Norit GSX. The experimental curve follows the Langmuir isotherm (solid line in figure B.1) given by:

$$\theta = \frac{KP}{1 + KP},\tag{B.2}$$

where θ is the coverage of the adsorbent surface, K is the equilibrium constant and P is the pressure. From the Langmuir isotherm a coverage of approximately 0.8 was derived.

We modified this model to get the temperature dependence of the pressure of the gas above a surface. Introducing the rate of adsorption, Φ_a, which is proportional
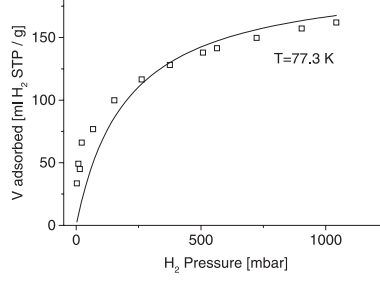
Figure B.1: Hydrogen adsorption capacity for activated charcoal (Norit GSX) as a function of hydrogen pressure. The line is a fit with a Langmuir adsorption isotherm. The hydrogen surface coverage $\theta \approx 0.8$ at $P = 1$ bar.
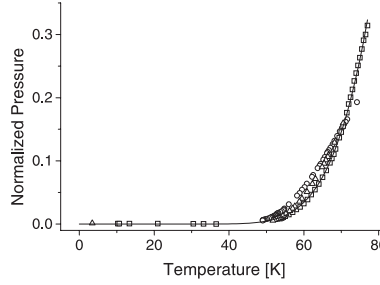
Figure B.2: Temperature-pressure curves for SWNT (circles), Norit AC 990293 (triangles) and Norit GSX (squares). The line is a fit with the model $P = C'\sqrt{T}e^{-\frac{H_{ad}}{kT}}$ through the measured curve for Norit GSX. Using this model the adsorption energies were obtained (580±60 K).

to the number of molecules hitting a vacant adsorption site we get:

$$\Phi_a \propto \frac{P}{\sqrt{T}}(1 - \theta), \tag{B.3}$$

where T is the temperature of the system and $(1 - \theta)$ is the fraction of unoccupied adsorption sites. We used the fact that the density of a gas is proportional to the pressure, whereas the average gas molecule velocity is proportional to $\sqrt{T}$. The rate of desorption, Φ_d, is proportional to a frequency, f, at which the surface atoms vibrate (this frequency is of the order of 10^{13} Hz) and the Boltzmann distribution factor, giving:

$$\Phi_d \propto fe^{-\frac{H_{ad}}{kT}}\theta, \tag{B.4}$$

where H_{ad} is the enthalpy of adsorption, k is the Boltzmann constant and θ is the fraction of occupied adsorption sites. Combining these two gives:

$$P = Cf\sqrt{T}e^{-\frac{H_{ad}}{kT}}\frac{\theta}{1 - \theta}, \tag{B.5}$$

with C being a constant. When the volume of the gas phase is small, we can assume the fractional coverage θ to be constant in the temperature range investigated. For

two samples (SWNT and NAC) we recorded the pressure as a function of the sample temperature during cooling. The pressure of hydrogen gas above Norit GSX during warming was also measured. These measurements are presented in figure B.2. The least squares fit on the GSX data with the model derived above is shown in the figure. Results from these fits are given in table B.1. From the errors associated with the fitted values of the adsorption potentials, we conclude that the adsorption potential is 580±60 K or 5±0.5 kJ mol^{-1}. The review article of Vidali et al. on potentials of physical adsorption give a well depth of 51.7 meV for graphite, which equals 600 K or 5 kJ mol^{-1}, [46] in agreement with our results. Clearly the value of Dillon et al. of 19.6 kJ mol^{-1} for hydrogen adsorbed onto single walled carbon nanotubes is not reproduced. [18]

Table B.1: Properties of the investigated materials. V is the volume at standard temperature and pressure (1 bar and 295 K) of hydrogen stored in 1 g of material at 77 k and 1 bar, S_{BET} is the BET surface area (the value for SWNT is from reference [61]) H_{ad} is the enthalpy of adsorption derived from pressure-temperature curves and p is the peak position in the neutron spectra due to the rotational transition.

	NAC	GSX	SWNT	GNF
V [ml STP]	238	160	60	20
S_{BET} [m^2/g]	2200	933	380	196
H_{ad} [K]	513	576	525	-
p [cm^{-1}]	119	120	119	117

The macroscopic measurements show that hydrogen adsorption on carbon surfaces as a function of hydrogen pressure already starts to saturate at 1 bar at a temperature of 77 K (see figure B.1). The sites at which the hydrogen molecules adsorb under the experimental conditions in this work will be commensurate with the carbon hexagons in the matrix [134]. The layout of these sites is hexagonal with a distance between reflections planes of 3.69 Å[134], corresponding to a density of 1 hydrogen site per every three hexagons. This low density of sites explains how a coverage of 80% can be found from the Langmuir isotherm. On geometrical grounds, using a site area based on the hydrogen molecular size of 0.142 nm^2 only, a coverage of $\approx 34\%$ is derived [16]. It is known that at higher fillings (attainable using lower adsorption temperatures) an incommensurate hydrogen layer is formed with such a much higher packing [134].

B.4.2   Inelastic neutron scattering results

Figure B.3 shows the measured spectra for the four different carbon materials. Table B.1 lists the results from least squares fits of the peaks with a Gaussian peak profile. The Gaussian peak profile was chosen because it is a good description of the
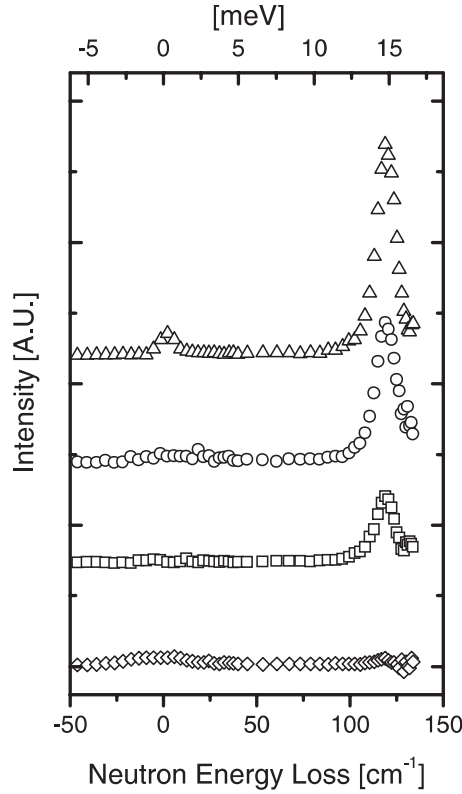
Figure B.3: Neutron energy loss spectra of hydrogen adsorbed in Norit AC990293 (triangles), single walled carbon nanotubes (circles), Norit GSX (squares) and graphitic nanofibers(diamonds). The data are normalized on the incident number of neutrons on the sample. The (mostly elastic) scattering of the sample without hydrogen has been subtracted (see text) which makes that only the scattering by hydrogen is visible. The graphitic nanofibers adsorb even after extra filling a very small amount of hydrogen, resulting in a very weak peak.

resolution function of the instrument at these energy transfers. The determination of the absolute position of the peaks is influenced by systematic errors due to uncertainties in the neutron incident energy and path-lengths in the instrument. We estimate this error to be 2%, which is 2 cm^{-1}, of the neutron energy loss. The fitted peak positions show that a shift of the rotational transition energy cannot be observed within experimental accuracy. The peak widths are comparable with the experimental resolution, which was determined to be 11 cm^{-1} (full width at half maximum) from a gauge measurement on solid hydrogen. No splitting of the $J = 1$ level due to hindering of the rotation was observed.

The intensities in the elastic peak (zero energy transfer) are much lower than the rotational transition peak. This excludes the presence of molecular ortho-hydrogen and of atomic hydrogen in significant amounts, because scattering cross-sections for both are larger than for the transition of $J = 0$ to $J = 1$. Furthermore the elastic peak intensity compared to the inelastic peak intensity is as should be expected for the scattering by the para-hydrogen in the samples. Also when observing the

spectra of the samples as a function of time (obtained from the different subruns for each spectrum) it was clear that the conversion of ortho- to para-hydrogen was completed already during the few hours of cooling. This is caused by the enhanced nuclear relaxation induced by the paramagnetic catalyst residuals (SWNT, GNF) or impurities (NAC, GSX).

Because the elastic peak intensity is so small this leaves no room for atomic hydrogen (having a large neutron cross-section) to be present in any significant amount. The assumption that a part of the reversible hydrogen storage is via the formation of atomic hydrogen and hydrogenation of the carbon is therefore not supported by the results. This contrasts with the assumptions in some recent theoretical works [22]. Also in the Pd loaded sample there is no sign of enhanced H_2 take-up due to the formation of atomic H (the Pd itself will absorb hydrogen up to $PdH_{0.6}$, but the concentration is too low to observe).

The $J = 1$ rotational peak is in the same position in carbon materials that have completely different topologies: the highly regular curved sheets of carbon in SWNTs, conical curved carbon sheets in fishbone nano-fibres, and highly porous activated carbons. Evidently the conclusion has to be that the morphology of the carbon surfaces has little effect on the rotation potentials for hydrogen. This would indicate that also the bonds responsible for the adsorption are similar in the different materials, in agreement with the macroscopic adsorption data. The claims for large adsorption capacities in SWNTs can now be discarded both on the basis of macroscopic adsorption data and microscopic interaction strength's.

Discussion INS results

Here we will compare our neutron results on the SWNT with the three other types of sample as well as with results found by others in C_{60} [48] and single walled nanotube containing samples [50, 51]. This comparison will give an answer to where the hydrogen molecules are located in the SWNT sample.

It is important to note that SWNT form bundles of many aligned tubes during the production process [135]. On our sample we found that the X-ray diffraction pattern showed a peak at a momentum transfer of 0.536 Å^{-1}. This corresponds to a plane distance of 1.17 nm, and assuming a close packing of the tubes, the average tube-tube distance is 1.35 nm. This is close to the minimum distance between tubes that we measured using TEM (1.25 nm). We will use the X-ray figure of 1.35 nm because it may represent a better average tube-tube distance for the bulk of the sample.

It is sometimes suggested that the hydrogen molecules go in the interstitial channels of the nanotube bundles. In that case the number of available hydrogen sites will be very large compared to the situation where hydrogen adsorbs on the outer surface of the bundles only. In C_{60} hydrogen indeed enters such interstitial sites. Fitzgerald et al. used a pressure of 130 bar to load hydrogen in C_{60} at room temperature, after which the hydrogen was frozen in the lattice at 150 K. The position

of the hydrogen molecules on the interstitial sites in C_{60} was determined by neutron diffraction methods [48]. There are two types of sites (or voids) available for H_2: one with a diameter of 2.26 Å and one with a diameter of 4.12 Å. Only the last site was shown to accommodate H_2 up to 40%, the first site is not occupied at all. The fact that the H_2 does not enter the smaller site was explained by the size of the H_2 molecule being too large, it has a diameter of 2.9 Å. The $J = 1$ level of hydrogen in the occupied sites was shifted downwards to 14.35 meV (115.7 cm^{-1}), and also split [48] by 0.7 meV (6 cm^{-1}). This indicates a significantly larger change in the rotational energy levels and also interaction of the hydrogen with the C_{60} matrix than in any of the samples measured by us. Such splittings and shifts would have been observed in our experiments. The fact that we find peaks that within error bars are not shifted with respect to solid hydrogen, shows that indeed hydrogen is very weakly disturbed by the bond to the surface of all of the carbon materials under investigation. This indicates a weak bond, which is supported by the macroscopic measurements.

Inelastic neutron spectra in samples containing soot and 20-30 weight % or 50 volume % of single walled carbon nanotubes have been published before by Brown et al. [50] and Ren et al. [51] respectively. These samples contained significant amounts (80-70 wt.% and 50 vol.% respectively) of amorphous and nanocrystalline carbon as well as metal nanoparticles. Especially the nanostructured carbon is problematic in this respect because its surface area will be non-negligible, making significant amounts of hydrogen adsorption possible. Their experiments used pressures as high as 110 bar to load the sample container with the sample with hydrogen. After this initial loading the sample was cooled to 25 K, where the hydrogen source was disconnected. Subsequently the cells were evacuated at $\approx$25 K to remove any non-adsorbed hydrogen. It may be noted that this loading procedure is rather different from ours, because we used just 1 bar at 77 K to adsorb the hydrogen. However, we obtained in a reproducible manner similar or higher adsorbed hydrogen amounts for the SWNT. Both articles report the inelastic (unsplit) peak due to the hydrogen molecular rotor. The peak position was found to be close to the value for the free H_2, the elastic peak was not clearly shown.

Combining the results and comparing with the situation for C_{60}, we may state that H_2 does not enter the interstitial channels of the SWNT sample, and the reason why may be illustrated in figure B.4. The diameter of the interstitial channels between nanotubes of 1.35 nm diameter is 2.1 Å, which is too small for hydrogen molecules to enter. It is even smaller than the void in C_{60} of 2.26 Å which is not occupied by H_2 either. Furthermore the inelastic neutron data show no difference between the four different types of nanostructured carbon samples. Because the size of the channel between the SWNTs is much smaller (2.1 Å) than the void in C_{60} (4.12 Å) one would expect at least a similar but likely a larger influence on the spectra of the adsorption in the channels. Clearly this is not the case and we therefore have to exclude that significant amounts of H_2 adsorbs in the interstitial channels. It may also be noted that Talapatra et al. reported that smaller gases
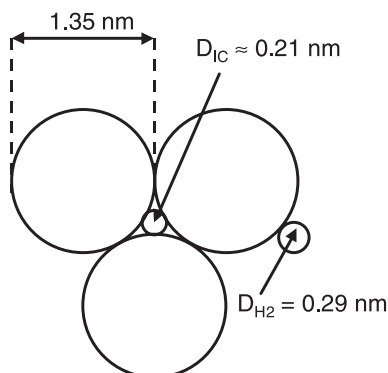
Figure B.4: Schematic graph of the consequence of the stacking of nanotubes in bundles with tube-tube distances of 1.35 nm. The interstitial channel between the bundles is indicated to be too small for hydrogen molecules (2.1 Å versus 2.9 Å).

like He and Ne did not enter the interstitial channels either [135].

B.4.3   Calculations

The materials all have aromatic rings in their graphite structure. The fact that the different samples give the same results for the interaction potentials raises the hypothesis that the characteristic van der Waals bonding can be modelled by only taking into account a carbon hexagon structure with its delocalized electrons.

As a check we performed computer calculations by means of Density Functional Theory, using Dmol^3. We used the numerical basis set DND (double numerical with d functions) and the Perdew Wang local correlation density functional. First we optimized the position of a hydrogen molecule above a small piece of graphite built from four carbon hexagons (figure B.5). The position with lowest energy for the hydrogen molecule was 2.91 Å above a central C-C bond. Then we turned the hydrogen molecule stepwise by 180 degrees and evaluated the potential energy each 20 degrees. In this way we obtained an estimate of the barrier for rotation for the adsorbed molecule. The barrier we find is indeed very small and is within
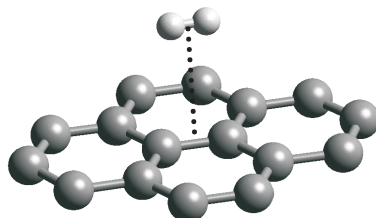
Figure B.5: The graphite surface and the hydrogen molecule in their minimum energy position. The hydrogen molecule is located right above the center of the C-C bond. From this configuration the energy was calculated using DFT when the hydrogen molecule was turned around.

computational accuracy consistent with the experiments.

We conclude that different forms of carbon are essentially the same for hydrogen molecules as long as they possess the characteristic aromatic carbon rings. Thus the amount of hydrogen storage is governed by the number of accessible aromatic C-C bonds in the sample, which is related to the surface area. The morphology of the adsorption sites on more than one C-C bond distance has less importance.

B.5   Discussion

From this study some perspectives for hydrogen storage using physisorption onto graphite surfaces can be evaluated. It appears that these materials will not meet the goals set by the Department of Energy of the US (6.5 wt%) at moderate conditions such as room temperature and pressures up to 10 bar. This can be concluded from the interaction energy which is around 580 K (5 kJ/mol) (which means that at room temperature virtually no hydrogen adsorbs) and from the fact that even a single graphite sheet needs to be covered for 80% by hydrogen molecules on *both* sides to meet the goals.

An ideal hydrogen storage material using physisorption would have an interaction potential around 2500 K ($\approx$ 20 kJ mol^{-1}) and a very high surface area (>2000 m$^2 g^{-1}$). In this way the residence time at room temperature for adsorbed molecules is comparable with hydrogen adsorbed on graphite at 77 K. Optimizing the surface area and hydrogen pressure could then in principle lead to a material capable of storing 6.5 wt% of hydrogen at room temperature and moderate pressures. However, at present there is no indication as how to realize such a high interaction potential in a material with a high specific surface area.

Recent experiments on carbon materials by G. Gundiah and co-workers showed hydrogen storage capacities in the range of 0.2 wt% to 3.7 wt% at 300 K and 140 bar [38]. In order to compare these results with ours, we have to extrapolate the use of equation (B.5) to a temperature of 300 K. We take the coverage θ to be the same for both temperatures, meaning the same amount of storage. Further we assume to be constant the frequency f and the adsorption enthalpy H_{ad}=580 K. With these assumptions we estimate a pressure of 530 bar at 300 K to give similar storage capacities as 1 bar at 77 K. In our work we found a hydrogen storage capacity for SWNT of 60 ml STP per g, which equals 0.54 wt%. The ratio of the estimated pressure (530 bar) and the pressure used by Gundiah et al. (140 bar) is comparable to the ratio in hydrogen storage capacities (0.54 wt% versus 0.2 wt% for untreated SWNT). Their results for untreated SWNT therefore supports the findings presented in this work.

B.6 Conclusions

In this article we report a study of microscopic aspects of physisorption of hydrogen on carbon surfaces with several nano morphologies. From the isotherms and temperature dependent pressure measurements we conclude that the interaction between a hydrogen molecule and a carbon surface is 580 ± 60 K or 5 ± 0.5 kJ mol^{-1}. However, at room temperature and ambient pressure the residence time is very short, leading to negligible adsorption. Inelastic neutron scattering experiments reveal that molecular H_2 is present and that the splitting of the ground and excited level of the molecular hydrogen rotor is essentially the same as for free hydrogen in all investigated carbon materials. No sign of a strong bond of the hydrogen molecule with the substrate was found in any of the materials. This finding compared to H_2 loaded interstitially in C_{60}, and the low adsorption quantities rule out the possibility that H_2 adsorbs in the narrow interstitial channels between the nanotubes. The bond of hydrogen to carbon does not depend on the topology of the surface. The only thing that counts then is the amount of surface accessible by hydrogen. This surface area appears to be largest in the activated carbons. The SWNTs form bundles and this aggregation apparently severely limits the accessible surface. Computer calculations using Density Functional Theory confirm that the hydrogen molecule is weakly bound to a C-C bond where it experiences only a small barrier for rotation.

Appendix C

Resolving Rotational Spectra of Hydrogen Adsorbed on a Single Walled Carbon Nanotube Substrate

Some of the early results on hydrogen storage in single walled carbon nanotubes (SWNT) have not been reproduced and at the moment it is generally believed that SWNT store hydrogen in molecular form in the same way as other graphitic materials with a high surface area.[8] Untreated nanotubes are bundled which limits the accessible surface area drastically, but thermal and acidic treatments can increase the hydrogen storage capacity due to an increase in accessible surface area.[38] Furthermore the adsorption energy of hydrogen on SWNT and other nanostructured carbons are comparable.[39] Here we present a detailed description of the adsorption of hydrogen in SWNT materials.

The energy E_J of the rotational level J associated with the rotation of a hydrogen molecule is quantized: $E_J = J(J+1)B$, where B has the value 7.35 meV (59.3 cm^{-1}).[47] The rotational spectrum of H$_2$ will be distorted when it is adsorbed and the triple degeneracy of the $J = 1$ level can be lifted making the rotational levels split. We use the transition from $J = 0$ to $J = 1$, which, in a centro symmetric environment, has two lines with intensities 1:2. In general a stronger interaction between the adsorbed molecule and adsorbent leads to a more distorted spectrum, providing a sensitive and a local probe of the environment of a H$_2$ molecule.[39, 136]

Neutron scattering results of the region of interest (i.e. around the rotational peak) are presented in Figure C.1. The insets (a) and (b) show the whole spectrum measured for the highest H$_2$ loading and the background run, respectively. The neutron spectra show a strong peak around 14.7 meV, the energy of the rota-
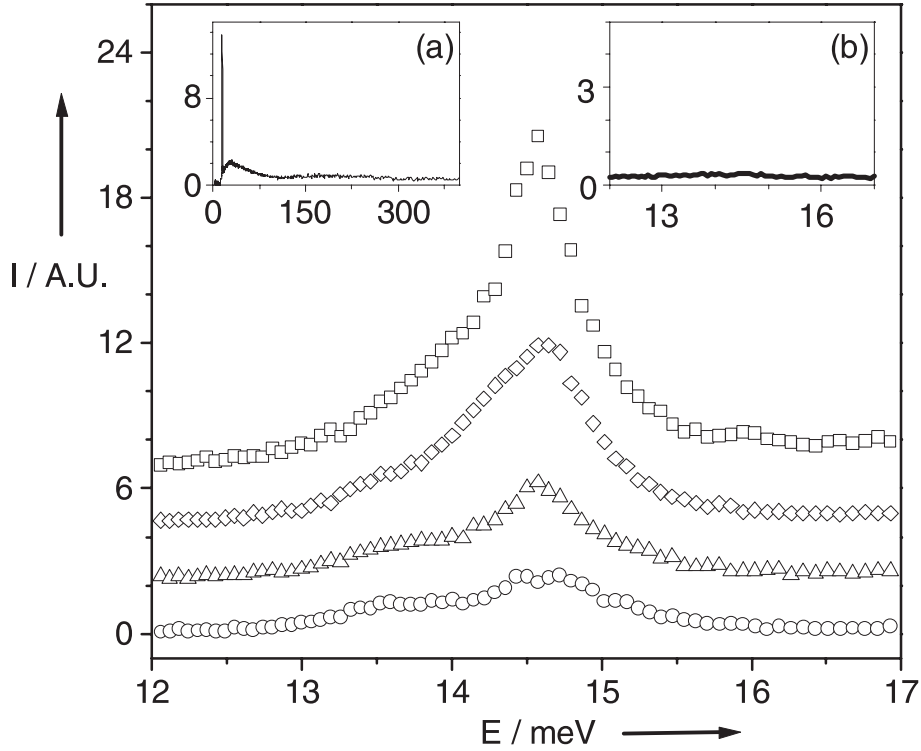
Figure C.1: Inelastic neutron spectra for indicated hydrogen loadings in single walled carbon nanotubes. Spectra are taken at a loading of 267 ml (squares), 157 ml (diamonds), 85 ml (triangles) and 56 ml (circles) STP H_2. Inset (a) shows the whole spectrum for the highest loading. The broad wing visible between 20 and 100 meV is due to recoiling H_2 molecules. Inset (b) shows the spectrum of the bare nanotubes.

tional transition. This peak indicates unambiguously that hydrogen is adsorbed in *molecular* form. The rotational peak in the spectra is made up from more than one component. The additional structure of the rotational spectrum was not seen before due to a lack of resolution.[39, 50, 51] Initially the peak shows a doublet. At higher loading a broad peak adds up. The last spectrum shows these two contributions together with a sharper line on top.

In Figure C.2 fits using Gaussians are given of each of the spectra with the separate contributions. Table C.1 gives the parameters of the fits used. The spectrum with the lowest H_2 loading clearly shows two peaks (I and II) upon visual inspection with rough intensity ratio's of 1:2. As described above this is a spectrum of a single hydrogen site. However, the fit improved by adding a separate weak line in between the two others (peak III). This would correspond to a weakly populated second site where there is less anisotropy in the environment i.e. less distortion of the H_2 molecule. For a higher loading of hydrogen the first two lines are always present, increasing in intensity for a filling of 85 ml STP, but saturated for higher fillings.

In the spectrum of 157 ml STP of adsorbed H_2 the additional line III appears

Table C.1: Areas, widths and positions of the four Gaussian lines used to fit the neutron data. Line I and II have the same width and areas as 1:2. Line III is always present and starts to saturate at the loading of 157 ml. Line IV only comes into play at the highest loading, when a second layer has been formed.

V / ml	56	85	157	267
A_{I} / A.U.	0.95	1.26	1.26	1.26
A_{II} / A.U.	1.91	2.51	2.51	2.51
$w_{\mathrm{I}} = w_{\mathrm{II}}$ / meV	0.85	0.85	0.85	0.85
x_{I} / meV	13.63	13.63	13.63	13.63
x_{II} / meV	14.72	14.72	14.72	14.72
A_{III} / A.U.	0.26	0.52	4.08	4.15
w_{III} / meV	0.32	0.32	0.74	0.98
x_{III} / meV	14.53	14.53	14.48	14.33
A_{IV} / A.U.	0	0	0	3.16
w_{IV} / meV	-	-	-	0.36
x_{IV} / meV	-	-	-	14.58

stronger and broadened. The highest loading we studied (267 ml STP), shows in addition to the spectrum at 157 ml STP a sharp peak at the position corresponding to free hydrogen. The equilibrium pressure here approaches, but is certainly lower, the pressure of solid hydrogen at the experimental temperature.

The macroscopic measurements are shown in Figure C.3. In the case of adsorption at temperatures high enough so that less than a monolayer adsorbs, the Langmuir isotherm is applicable: $V = V_L kP/(1 + KP)$, where V is the adsorbed volume, V_L is the volume of the gas which fills up all available sites, k is a kinetic constant and P is the pressure. The line which fits the first part of the isotherm is drawn in Figure C.3. It is known that at low temperatures hydrogen adsorbed on graphite possesses different phases, depending on temperature and loading.[134, 137, 138, 139] In order to measure in a suitable pressure range the isotherm was measured at 60 K, i.e. much higher than the melting points of these 2-D phases.[140] At these temperatures the system can be described as supercritical matter, in which the H$_2$-H$_2$ intermolecular distances become continuously smaller as the density increases.

The straight part of the isotherm can be explained by the application of Gibbs equation stating that the concentration of the adsorbed layer is proportional to the concentration of the gas phase, i.e the pressure. After completion of the first monolayer the pressure will rise rapidly, explaining the kink at 163 ml g^{-1} in the isotherm. The adsorption potential of this second layer is much less than of the first adsorbed molecules. From the amount of adsorption at the completion of the first layer we can calculate the surface area as follows: 163 ml (STP) or 190 ml g^{-1} has been adsorbed, this is 8.5 mmol H$_2$ g^{-1} or 5.1×10^{21} molecules H$_2$ g^{-1}. Using the surface area per hydrogen molecule calculated from a two dimensional close packed
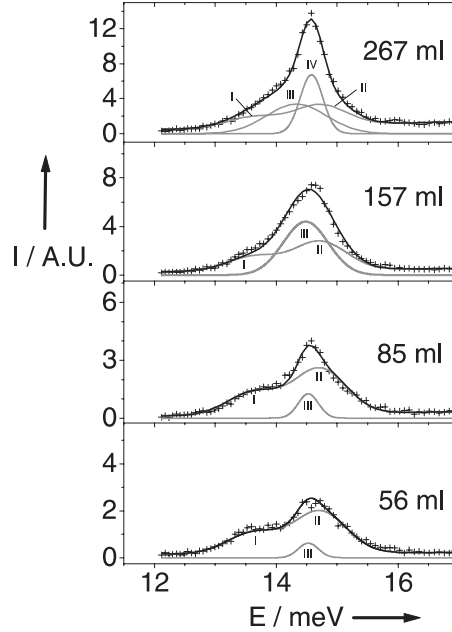
Figure C.2: The fit (solid line) of the spectra (symbols) with spectral contributions as described in the text drawn separately (gray line). Gaussian lineshapes were used for the $J = 0$ to $J = 1$ rotational transition of hydrogen adsorbed on several surface sites in the nanostructured SWNT matrix. Lines I and II result from one adsorption site and are therefore taken together (including the background). Lines III and IV are drawn separately in gray. Parameters can be found in Table C.1.

layer of hydrogen molecules with a nearest neighbor distance of 3.51 Å [134, 137] i.e. 0.107 nm^2, we find the surface area: 550 m^{2}g^{-1}. This is 45% higher than the surface area of 380 m^{2}g^{-1} found by Eswaramoorthy et al.[61] Our value may be higher due to sample differences and because the hydrogen molecule is smaller than nitrogen that is used in the BET analysis. H$_2$ may occupy some of the smaller voids in the structure thus probing an effectively larger surface area.

Nanotubes are arranged in bundles. Grooves between the tubes in the bundles may form a site which is favorable for hydrogen adsorption: because the hydrogen molecule can touch two surfaces,[38, 55, 40, 57] the adsorption potential is known to be about twice that of hydrogen on planar graphite. During the neutron measurements at 15 K there is sufficiently low mobility of the hydrogen molecules to spend more time in such a groove because this is energetically favorable,[57] i.e. such groove forms preferential sites. In literature there has been a long discussion about the nature of the adsorption sites for gases in nanotube samples. Some authors suggested interstitial or intertubular sites. However as we indicated earlier,[39] adsorption of hydrogen is not possible in interstitial sites when all tubes have comparable diameters, because the intertubular voids are much to small (2.1 Å diameter) for the large hydrogen molecules (2.9 Å diameter). Lately Johnson et al. proposed the model of a bundle of nanotubes with different diameters.[62] Then statistically
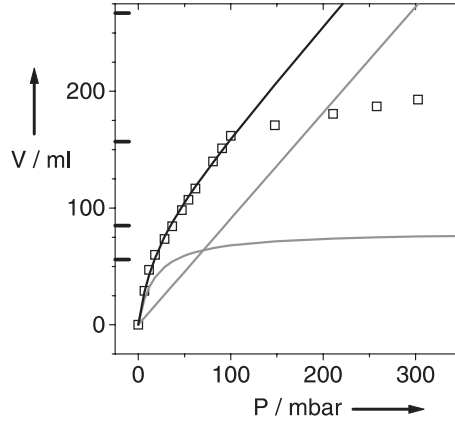
Figure C.3: The pressure-composition isotherm for 0.85 g of single walled carbon nanotubes measured at a temperature of 60 K. The line drawn in the figure is the Langmuir isotherm which fits the first part of the measured isotherm. The function is represented by $V = V_L kP/(1 + kP)$ where the maximum amount of adsorption in the preferential site $V_L = 80$ ml STP and $k = 0.057$ mbar^{-1} is a kinetic parameter. The straight section between ≈ 50 and 160 ml shows that the density of the adsorbed layer increases continuously as a result of adsorption on the carbon surface at temperatures far above the critical temperature. Above ≈ 160 ml adsorption requires higher pressures because the first hydrogen monolayer becomes saturated and further layers have lower adsorption potentials. Bold tick marks on the vertical axis indicate the loadings that were used for the neutron measurements.

some misfits may occur which provide voids large enough for hydrogen to adsorb in. In any case the total amount of accessible surface is given by what comes out of the measurement of the adsorption: 550 m^{2}g^{-1}.

The analysis of the spectra as given in Table C.1 results in the following observations. There appears indeed to be a site that is occupied preferentially at low temperature. However, this site is saturated rapidly and contributes only to a fraction of the total adsorption at higher H$_2$ loading. This compares well with limited numbers of sites in the grooves as described above. For higher loading the rest of the surface area of the bundles becomes progressively occupied. Having smaller adsorption energy this apparently also results in a lower distortion of the spectrum contribution III. The change of the shape of peak III upon increasing occupation may be related to the changes in the proximity of neighboring H$_2$ molecules. These molecules are initially relatively far from each other, hardly feeling each other, giving a narrow peak (degenerate $J = 1$ level). The layer which we observe in the third spectrum with a loading of 157 ml STP, is an almost fully packed surface layer. Then apparently slight (distributions of) hindering of the rotational modes of the hydrogen molecules results, making the peak broader than the experimental resolution.

For the highest loading a fourth spectral contribution occurs that we attribute to the formation of additional layers of H$_2$ on top of the first monolayer. The vapor pressure at the temperature of the measurement was still too low to form solid

hydrogen in the sample. The signal from these layers is almost the same as from free hydrogen because the adsorption potential is (almost) as low as that in solid hydrogen: the signal is located close to 14.7 meV. The linewidth of this contribution equals the instrumental resolution. Such layers have been observed previously in vycor cavities.[141]

Using a combination of techniques we are able to unravel that hydrogen first adsorbs on a preferential site, most likely the grooves. Subsequently, it occupies the surface of the tubes, where it has very high mobility. The density of hydrogen molecules on the surface of the nanotubes is proportional to the gas pressure up to completion of the first layer. Finally, a second layer is formed as the pressure is increased, even when the adsorption temperature is far above the critical temperature. The findings presented here show that adsorption on convex surfaces such as present in nanotubes is similar, but not equivalent to adsorption on planar surfaces.

Experimental Section

SWNT were obtained from Carbon Nanotechnologies Inc. The nanotubes were produced by the HiPCo process in which $Fe(CO)_5$ decomposes in a CO atmosphere.[133] Our sample contains less than 5 at% of leftover iron catalyst. The sample was characterized by X-ray diffraction, which showed no sharp peaks, indicating that no crystalline form of graphite or iron was present. From TEM-measurements we inferred that the nanotubes are packed with a smallest repetition distance of about 1.25 nm, indicating that the size of the tubes is around 1.25 nm.

The inelastic spectra were recorded using TOSCA (ISIS, UK).[142] The resolution of TOSCA at the region of interest (i.e. an energy transfer of $2B$=14.7 meV) is 0.3 meV. An aluminium sample cell was loaded with 0.85 g of SWNT. The sample was evacuated at 353 K to pressures of 10^{-4} Pa for 20 hours to remove water and other adsorbed molecules. The cell was cooled down to 77 K and hydrogen was loaded to a known amount. Spectra were recorded at loadings of 0, 56, 85, 157 and 267 ml H_2 STP, and at 15 K to avoid unwanted broadening of the spectra by thermal diffusion. The whole series of measurements including a background run took 14 hours. The data is normalized to incident monitor counts, so that the area under a peak is a direct measure of the amount of hydrogen present in the sample cell. The signals from forward and backward detectors were added.

The sample cell and cryogenic equipment we used for the neutron measurements, was also used to measure the pressure-hydrogen content isotherm. The gas-handling system had a known volume at room temperature. Thin capillaries connected the room temperature volume with the sample cell operated at 60 K. This temperature was used in order to have sufficient accuracy for the pressure measurements and because it is near our reference temperature used before.[39] The isotherm was measured by adding small amounts of hydrogen gas and recording the equilibrium pressures.

Acknowlegdements

Appendix D

The Vibrational Spectrum of Magnesium Hydride from Inelastic Neutron Scattering and Density Functional Theory

H.G. Schimmel, M. R. Johnson, G.J. Kearley, A.J. Ramirez-Cuesta, J. Huot and F. M. Mulder, *Materials Science and Engineering B-Solid State Materials for Advanced Technology*, **108**, 38-41 (2004).

Abstract

Light-weight magnesium metal can reversibly store up to 7 wt.% hydrogen and is therefore interesting for application as hydrogen storage material. Neutron vibrational spectroscopy has been used to study the interactions of hydrogen atoms with it surroundings. The neutron spectra are compared directly with Density Functional Theory calculations providing detailed insight in structure and dynamics. Dispersion of the vibrational modes has to be taken into account in order to reproduce the data. This study on bulk magnesium hydride will provide a bench mark for similar studies on nanostructured magnesium alloys: these are more promising as hydrogen storage materials because of their significantly faster hydrogen sorption processes. Because of its sensitivity and the compatibility to calculations, the vibrational spectra of these nanostructured compounds can be used as a probe for the local structure and the influence of the nanostructure on the potential landscape experienced by the hydrogen. Parameters can be extracted for MD and Monte Carlo calculations of slower diffusion processes.

D.1   Introduction

The use of hydrogen as an energy carrier is hindered by several technical problems. Hydrogen is a very light and volatile gas, so that high pressures (several hundred atmospheres) or very low temperatures (hydrogen condenses at 20 K and 1 bar) are

needed to store an amount sufficient for mobile applications. Since several decades scientists are looking for materials which can reversibly store hydrogen. Currently intensive research is on light-weight magnesium alloys.[8] The hydride MgH_2 stores hydrogen up to approximately 7 wt%. However, its use at the present time is limited due to slow kinetics of the hydriding and dehydriding reaction, even at elevated temperatures.

To enhance the hydrogen sorption properties it is tried to reduce particle size, or alloy magnesium with other elements, or add catalysts.[76] Structural characterization methods such as X-ray diffraction are lacking sensitivity for the defect-type changes in the structure of the magnesium caused by the particle size reduction treatments. Neutron vibrational spectroscopy, on the other hand, can distinguish materials having different treatment histories. By applying neutron vibrational spectroscopy and comparing the results with computer calculations a structural model can be found that reproduces the vibrational data.[143] In order to apply these methods to MgH_2 and its nanostructured varieties a first step is to understand the bulk vibrational spectra. This first step is presented here. The calculations can tell which peaks are to be assigned to which vibrational modes in the data. It may be noted that vibrational spectra obtained with neutrons are significantly more straightforward to simulate than light-scattering spectra such as obtained with Raman and Infrared spectroscopy. The reason is that the neutron spectra represent the motions of the nuclei, not of the electrons, and the interaction between nucleus and neutron is known exactly. This makes that the intensities of the spectra at all relevant frequencies can be calculated much more directly. Additionally, the sensitivity is highest for the important element hydrogen. Modern calculation methods using Density Functional Theory are able to predict the experimental spectra with sufficient accuracy.[144] In this paper we present experimental work on commercial magnesium hydride powder as well as a simulated spectrum calculated using Density Functional Theory. It is shown that it is possible to achieve a satisfying agreement between measurement and calculation if we take into account dispersion.

D.2   Experiment

The neutron scattering spectrometer TOSCA we used is located at the pulsed neutron spallation source ISIS in the United Kingdom[1]. This spectrometer uses an 'inverted geometry' and is at present the fastest machine of its kind in the world. Incident on the sample is the pulsed beam of thermal neutrons which have been thermalised in water near the spallation source. Those neutrons which are scattered over an angle of 135 degrees (backward scattering) or 45 degrees (forward scattering) *and* which have a final energy of 3.5 meV are counted. By means of the time-of-flight of the neutrons their incident velocity can be calculated from which their energy transfer is derived. The sample is mounted in an air-tight aluminum sample container

---

[1]See http://www.isis.rl.ac.uk/molecularspectroscopy/tosca/ for a description of the instrument.
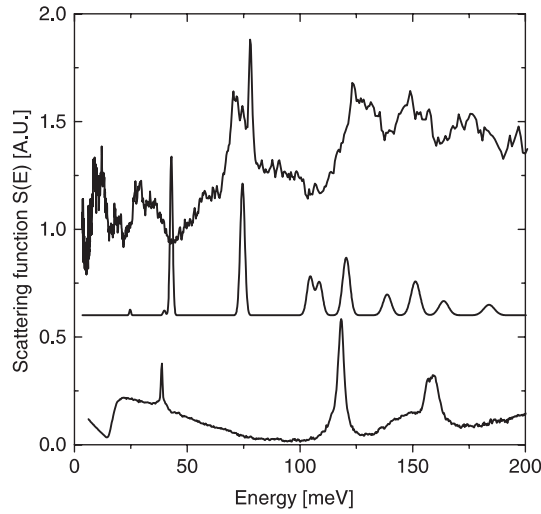
Figure D.1: Vibrational spectrum of MgH$_2$ obtained with neutron spectroscopy (top line), together with a Γ-point calculation with Density Functional Theory (middle line) and the Raman spectrum of the same compound (bottom line).

in a glove box. To obtain an accurate spectrum in a reasonable time, 0.30 gram of magnesium hydride was loaded in the sample container. The measured spectrum from the commercially obtained bulk magnesium hydride is shown as the top line in figures D.1 and D.2.

The broad wings in the spectrum are typical for a solid-state, dispersed phonon spectrum. An exception is the extremely narrow peak near 75 meV. The width of this peak is comparable to the width of the resolution function of TOSCA at this energy transfer. Normally such sharp peaks only arise in the case of a molecular crystal where certain internal modes of one molecule are not coupled to those of a neighboring molecule.

In light scattering the momentum transfer at energy transfers in the region 0 to 500 meV is always small compared to relevant momentum transfers in the sample. The reason is that the wavelength of light is approximately 1000 times larger than typical atomic distances. For instance Raman spectroscopy measures at a momentum transfer close to zero, the point of the Brioullin zone which is easy to calculate. The Raman spectra do not show the dispersion therefore. The measured Raman spectrum has a huge background due to fluorescence. This background has partly been subtracted so that the spectrum fits in figure D.1 (bottom line).

D.2.1 Density-functional theory and phonon calculations

With a calculation method which produces the energy of the total system for a given arrangement of the atoms and the Hellmann-Feynmann forces from the electronic wavefunction, it is possible to calculate the frequency spectrum. One starts with an optimised structure so that the atoms are in their minimum energy position for
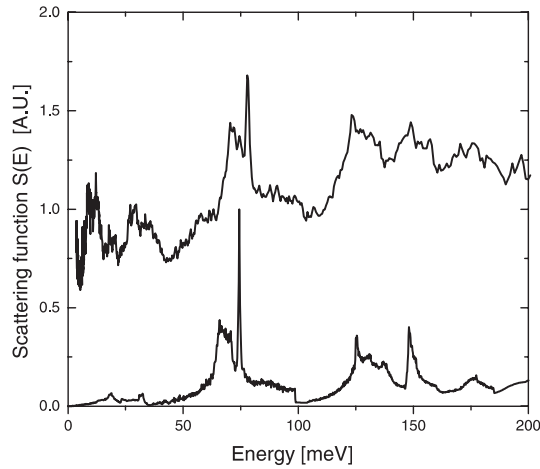
Figure D.2: Vibrational spectrum of MgH_2 obtained by neutron spectroscopy (top line) and simulation using a phonon calculation with force constants from Density Functional Theory (bottom line).

the calculation, with residual forces close to zero. Then each of the atoms in the asymmetric unit cell is displaced over a small distance along each of the Cartesian directions and the electronic structure is calculated for each displaced configuration giving the Hellmann-Feynmann forces on all atoms. Each configuration therefore gives one row of the matrix of force constants, the remaining rows being derived from the space group symmetry. Introducing the atomic masses in the force constant matrix gives the dynamical matrix, from which the normal mode frequencies and eigenvectors are obtained by diagonalisation. The INS spectrum is completely determined by this information, the atomic scattering cross-sections and the scattering vector Q.

The neutron scattering spectrum as calculated using DFT with $Dmol^3$ (gamma point only, no dispersion) is shown in figure D.1 as the line in the middle. This calculation used periodic boundary conditions on the unit cell. It clearly does not reproduce the neutron spectrum we measure. Note that the peaks calculated at 40 and 120 meV have analogues in the Raman spectrum. The Hirshfeld partitioning of the calculated electron density gives a charge of -0.16 e on the hydrogen atoms and +0.32 e on the magnesium atoms. This shows that the bonding is partly covalent, partly ionic.

Such a calculation with periodic boundary conditions is equivalent to a calculation at a momentum transfer of 0 Å^{-1} (the Γ-point). The fact that this Γ-point-only calculation does not at all reproduce the neutron spectrum shows that the interactions between atoms in neighboring unit cells are not negligible. Therefore the energy of a wave excited in the crystal by a neutron depends on its wavevector or momentum k (phonon dispersion). In order to take this dispersion into account, a more detailed phonon calculation had to be done.

For the phonon calculations on magnesium hydride we chose a supercell with

dimensions of 2a×2b×3c that is (8.5 Å×8.5 Å×9 Å). This is reasonable when compared to practice: a phonon calculation is converged if the force constants between an atom at the center of the supercell and those at the cell boundaries are effectively zero. For crystals of uncharged, organic molecules, this sphere of interaction typically has a radius of $\approx$5 Å. Since DFT methods scale in computational time with the third power of the number of atoms, the supercell calculations are considerably longer than single cell calculations.

All DFT calculations were performed with VASP [101, 145] using Vanderbilt-type ultrasoft pseudopotentials.[125] The recommended energy cutoff (396 eV) and a k-point spacing of 0.1 Å^{-1} were used. Atomic coordinates and lattice parameters were optimized in the single unit cell before constructing the $2 \times 2 \times 3$ supercell and optimizing the coordinates of the atoms once more. Using a reciprocal space representation for the pseudopotentials and a fine integration grid, as flagged by the ADDGRID command in VASP, very small residual forces on the atoms were obtained. The maximum residual force was 10^{-5} eV/Å and the average force was 10^{-6} eV/Å. A series of single point energy calculations, each of which give Hellmann-Feynmann (HF) forces acting on all atoms in the supercell, were then performed on the structures obtained by displacing, one at a time, each of the 3 inequivalent atoms by 0.05 Å in the inequivalent, positive and negative Cartesian directions. That gave 8 HF force calculations in all.

The HF forces and optimized supercell structure were then given as input to the program PHONON [102, 146, 147], which, by implementing the direct method, generates and diagonalises the dynamical matrix for any point in reciprocal space, using all the symmetry of the crystal structure (MgH$_2$ has a rutile-type structure with spacegroup $P4_2/mmm$). Force constants were checked and found to decay by three orders of magnitude in going from the supercell centre to the closest cell boundary.

For the density of states (DOS), a large number of reciprocal space points were chosen at random. The calculated external mode spectrum was then used to generate the multiphonon contributions to the spectral profile. The calculated dynamical structure factor $S(\mathbf{Q}, \omega)$ was obtained from the DOS for an isotropic polycrystalline sample, for the scattering configuration of the instrument. Finally the spectrum was convoluted with the instrumental resolution function. The spectrum that results is shown in figure D.2 as the bottom line. The accordance of the measured and calculated spectrum is remarkable.

## D.3   Discussion and conclusions

From the results obtained here we infer that an accurate description of the measured spectrum of magnesium hydride can be given if the force constants are evaluated using a supercell of at least $2 \times 2 \times 3$ unit cells. Force constants which range longer than the size of this supercell appear to be sufficiently small to be negligible. A mapping of the Brioullin zone in reciprocal space using the the program PHONON
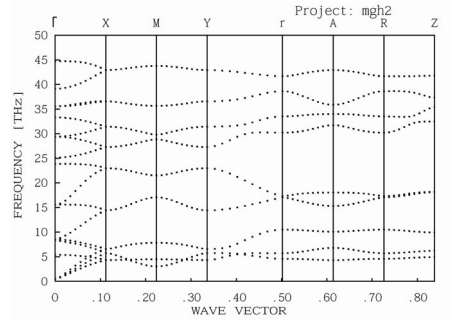
Figure D.3: The phonon dispersion curve as calculated by PHONON from force constants obtained from a Density Functional Theory calculation using VASP.

then reproduces the spectrum in an accurate way. Surprisingly the sharp feature present in the spectrum of magnesium hydride has its origin not in a local mode. It is due to the existence of a relatively flat part of the phonon branch as can be seen from figure D.3. Around the point A in the Brillouin zone, the phonon dispersion curve shows a flat part. The energy of this mode is the same as the energy of the sharp feature in the spectra. The point A in the Brillouin zone is shown in figureD.4. The wavevector associated with this point is one which has a wavelength of twice the unit cell in all directions. This means that the vibrations in all neighbouring unit cells are anti-parrallel. Phonons with wavevectors close to this point have energies very close to 75 meV so that a peak at this energy arises.

Now the spectrum is understood the vibrational spectroscopy may be applied to other than bulk MgH_2 samples. For instance if one substitutes some atoms or induces some stress in the material, phonon frequencies are expected to change by certain amounts. It may be anticipated that a small distribution in substituent concentration or induced stress will smear out the sharp peak, and such features may thus provide a sensitive probe for changes in the local environment of a hydrogen atom up to the length scale of a nanometer, which is not accessible by diffraction.
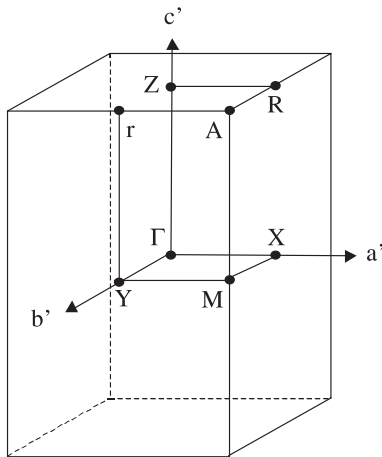
Figure D.4: The Brillouin zone of the tetragonal MgH_2 structure. Symmetry points used by the calculation are indicated.

Because of this small length scale it is also sensitive for defects, provided that the defect concentration is high enough. Defect concentrations may be very important for the hydriding and dehydriding properties of metals like magnesium. At present results on nanostructured MgH_2 are being analyzed and they do indeed show a large change of the narrow peak at 75 meV, in addition to more subtle changes.

We conclude that it is possible to reproduce the spectrum of a metal hydride system in a reliable way if one takes into account dispersion. We discussed certain features in the experimental spectrum using the calculation. This technique is potentially very useful as a probe of the environment of the hydrogen atom in magnesium hydride which is modified on nanometer length scales.

Appendix E

Structural Information on Ball Milled Magnesium Hydride from Vibrational Spectroscopy and Ab-Initio calculations

H.G. Schimmel, M.R. Johnson, G.J. Kearley, A.J. Ramirez-Cuesta, J. Huot and F.M. Mulder, submitted to *Journal of Alloys and Compounds*

Abstract

Ball milled magnesium hydride with an average size of about 40 nm and bulk magnesium hydride have been studied with vibrational spectroscopy together with density functional computer calculations. Using this combination of techniques structural information can now be obtained on a nanometer scale, which is especially important for nanosized samples. Such samples exhibit very broad diffraction lines, from which limited information about the structure can be extracted. It was found that ball milling distorts the vibrational spectra due a distribution in stresses over the sample. Cycling of the hydrogen content results in the spectrum of unmilled samples, while the particle size remains small and hydrogen storage characteristics continue to be better for ball milled samples. We conclude that improved performance for hydrogen storage applications of ball milled magnesium hydride has to be attributed to the reduction of the particle size, while defect densities inside the particles play less of a role.

E.1 Introduction

Magnesium metal is an interesting material in connection with hydrogen storage. The metal being light in weight is capable of storing up to 7 wt% of hydrogen. However, due to slow kinetics and thermodynamic characteristics, pure magnesium can only be hydrided at high temperatures and high hydrogen pressures. Several ways have been reported that speed up the hydriding and dehydriding processes. The

addition of a catalyst to the surface of magnesium particle enhances the kinetics [93, 94, 148]. Ball milling breaks down the magnesium hydride particles and induces stresses and defects in the structure [96, 95]. The ball milling treatment increases the hydriding kinetics by approximately a factor of 10. As ball milling breaks down the particles, a higher surface area is present for hydrogen to enter the particles. Ball milling introduces defects zones which may assist the diffusion of hydrogen to the MgH_2 nucleus, and defect clusters which may lower the barrier for nucleation of MgH_2. In order to reveal the most important factors in increasing hydrogen sorption, it is crucial to have a better understanding of the changes made by the ball milling treatment. Diffraction experiments are not suited for this purpose, because they rely on long range order in samples. The ball milled particles being small, show broad lines, and little information can be extracted from the diffraction spectra. Local changes and defects in the structure are only visible in the background. Vibrations on the other hand, are governed by forces between atoms which in general have a range less than one nanometer. By probing vibrations, together with a structural model and a method that predicts the vibrations, we can effectively probe the material on a nanometer scale and in this way become more sensitive to local defects [99]. As we reported before [100], we calculated and reproduced the vibrational spectrum of bulk MgH_2 (i.e. before ball milling). The present article reports further studies on ball milled magnesium hydride samples.

Magnesium hydride crystalizes in a rutile-type structure with spacegroup $P4_2/mmm$. MgH_2 transforms in an orthogonal γ-phase (α-PbO$_2$-type structure) at high temperatures and pressures [97]. In ball milled samples this phase is also present (according to X-ray diffraction results up to an amount of 25 wt% [96]). This phase is metastable in the ball milled samples and is removed when the hydrogen content of the sample is cycled or when a sample is heated to 570 K [96, 97].

E.2   Experimental Section

Bulk magnesium hydride (95 wt% MgH_2 and 5 wt% Mg) has been bought from Th. Goldschmidt AG. The hydride was mechanically milled under argon by using a Spex 8000 ball mill. A hardened steel crucible and three steel balls of 12.7 mm in diameter were used for milling. The ball to powder weight ratio was 10:1. All handlings were performed in a glove box under argon. X-ray diffraction was carried out using a Siemens D-5000 X-ray diffractometer with Cu K-α radiation. Hydrogen was removed from one ball milled sample by heating to 473 K under vacuum. When all hydrogen was removed from the hot cell, new hydrogen gas was introduced at a pressure of 5 bar, so that MgH_2 was formed again. Three samples of approximately 0.3 g were used in the experiments: a bulk sample, a ball milled and a ball milled rehydrided sample.
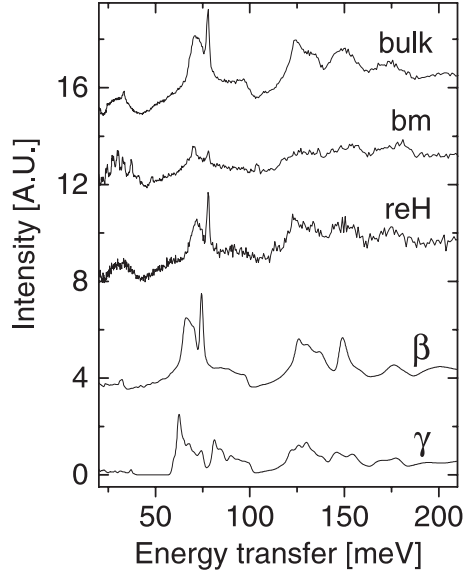
E.2.1   Vibrational Spectroscopy

Vibrational spectroscopy is an ideal tool for studying materials with a nanostructure. For nanostructured materials, diffraction experiments cannot distinguish between the size of the particles in the sample and a distribution in unit cell parameters. Vibrational spectroscopy is sensitive for the immediate environment of atoms. The vibrational frequencies and intensities are the result of forces between atoms which generally have a range shorter than 1 nanometer. Using neutrons in a sample with a high hydrogen content as MgH_2 means that we only observe the vibrations of the hydrogen atoms (the cross sections of Mg and H differ more than a factor 20). Neutrons are especially suited for vibrational analysis because they measure motions of nuclei, not of the electrons. The motions of nuclei are relatively easy to simulate using ab-initio calculations and the interaction between neutrons and nuclei is well known.

The inelastic neutron scattering spectrometer TOSCA is an instrument at the pulsed neutron spallation source at ISIS, United Kingdom. The instrument uses an inverted geometry, in which *scattered* neutrons with a final energy of about 3.5 meV are analyzed. Initial energies are calculated from the time-of-flights. TOSCA has an energy transfer range between 4 and 500 meV.

E.2.2   Calculations

Vibrations in adjacent unit cells of MgH_2 are coupled so that we actually measure a phonon spectrum. An accurate description of the measured spectrum requires a calculation of all phonons that exist in the Brillouin zone. The forces need to be mapped for all atoms within its range, about a nanometer. Therefore we chose a supercell with dimensions of 2a×2b×3c (that is optimized dimensions 9 Å×9 Å×9 Å) for the force calculations of MgH_2. All DFT calculations were performed with VASP [101, 145] using Vanderbilt-type ultrasoft pseudopotentials [125]. A series of single point energy calculations, each of which give Hellmann-Feynmann (HF) forces acting on all atoms in the supercell, were then performed on the structures obtained by displacing, one at a time, each of the 3 inequivalent atoms by 0.05 Å in the inequivalent, positive and negative Cartesian directions. That gave 8 HF force calculations in all. More details of this procedure are given elsewhere [100].

The optimized supercell and HF forces were then given as input to the program PHONON [102, 146, 147], which, by implementing the direct method, generates and diagonalizes the dynamical matrix for any point in reciprocal space, using all the symmetry of the crystal structure. Force constants were checked and found to decay by three orders of magnitude in going from the supercell centre to the closest cell boundary. For the density of states (DOS), a large number of reciprocal space points were chosen at random. By repeatedly convoluting this one-phonon spectrum with itself, the multi-phonon (upto 5) was obtained. The dynamical structure factor $S(\mathbf{Q}, \omega)$ was calculated for an isotropic polycrystalline sample, for the scattering configuration of the instrument. Finally the spectrum was convoluted with the

Figure E.1: Vibrational spectra (from top to bottom) of bulk MgH_2, ball milled MgH_2 and for MgH_2 that was ball milled and rehydrided. The calculations for β- and γ-MgH_2 are also shown.

instrumental resolution function.

Essentially the same procedure was used to simulate the vibrational spectrum of the γ-phase of MgH_2. We used a supercell with dimensions of 2a×2b×2c (giving 9 Å×11 Å×10 Å)

E.3   Results and Discussion

The spectra that we measured for bulk MgH_2, ball milled MgH_2 and for MgH_2 that was ball milled and rehydrided is shown in figure E.1 together with the calculations for respectively the β and γ phase. The sharp features in the spectrum result from parts of the phonon dispersion curves which are relatively flat so that they make up a peak or a sharp feature when summed up to form the experimental spectrum. These flat parts of the phonon dispersion curves can be found near the edges of the Brillouin zone as is clear from figure E.2a together with the picture of the Brillouin zone of MgH_2 in figure E.2b.

The sharp peak in the spectrum disappears almost completely during the ball milling treatment. The whole spectrum seems to have rounder features. Take for example the shoulders around 60 meV and 120 meV. The edge is much sharper for both the bulk and the ball milled rehydrided sample, whereas it is rounded off in the spectrum of the ball milled sample. It is expected that small changes in unit cell parameters due to the ball milling treatment shift the positions of these features in the spectrum. A relatively small distribution in stresses can thereby cause the observed rounding of the spectrum.
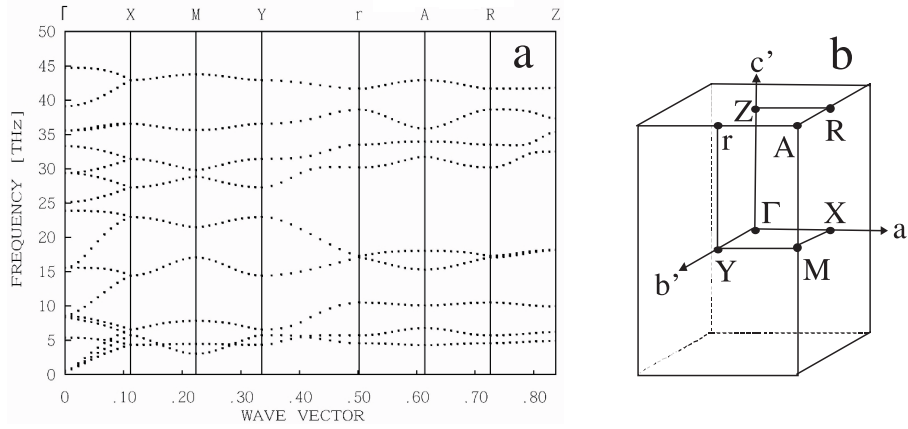
Figure E.2: The phonon dispersion curve as calculated by Phonon from force constants obtained from a Density Functional Theory calculation using Vasp (a) and the Brillouin zone of the tetragonal MgH_2 structure (b). Symmetry points used by the calculation are indicated.

In order to check the assumption that a distribution of stresses rounds the vibrational spectrum, we calculated the spectrum for magnesium hydride under an isotropic pressure of 10 kbar and for contractions of 2% of the a and c axes. Clear shifts of the features occur in these calculations. For the γ-phase we simulated a 2% contraction of all axes. A 'fit' of the experimental ball milled spectrum was constructed by taking the average of the different calculations for both the MgH_2 β- and γ-phases. Figure E.3 shows the measurement on the ball milled sample and a fit made from 25% of the averaged calculation for the γ phase plus 75% of the averaged β phase calculations together with an exponential background (the approximate phase fractions are taken from ref [96]).

The low-energy part of the spectra (i.e. between 20 and 50 meV) are shown in figure E.4. In this part the spectrum from the ball milled sample shows much more structure than the bulk and annealed samples. A comparison with the calculations shows that this part resembles more the γ-phase calculation than the β-phase calculation. The phase fraction of γ-MgH_2 might be as high as 50%, as judged from the low-energy region. A possible explanation may be that the γ-phase is so much distorted that in the high energy part (fitted in figure E.3) only a huge background is found. The calculations show that the low energy part is less effected by these stresses, so that the low energy part is a better source for the determination of the phase fractions. We conclude that the amount of γ-phase MgH_2 is much higher than 25%, likely as high as 50%. In the diffraction experiments [96] the excess amount of γ-MgH_2 apparently is invisible due to a very small particle size and possibly also strain effects, making the diffraction peaks too broad to be distinguishable from the background.

The extraction of hydrogen from the ball milled MgH_2, followed by a successive reloading gives a sample which has a vibrational spectrum equivalent to that of the
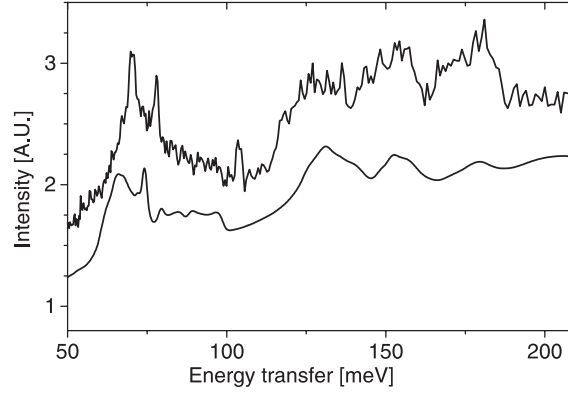
Figure E.3: The vibrational spectrum of ball milled magnesium hydride (top) with 'fit' (bottom). For both phase (β and γ) calculations have been performed on deformed structures. These calculations are averaged and used in the fit shown which consists of 75% of the calculated and averaged spectrum of β-MgH$_2$ plus 25% of γ-MgH$_2$ plus the background function $2.2 - 1.7 \exp(-0.01E)$. However, as becomes clear from figure E.4, the actual fraction of the γ phase is much higher than 25% and a large portion of the background has to be attributed to γ particles.

bulk, unmilled powder (see third spectrum from above if figure E.1). The cycling of the hydrogen content thus reduces the stresses resulting from the ball milling treatment, removes the γ-phase and anneals defects because the whole of the sample undergoes a phase transition during the cycling of hydrogen. It is known that the kinetics of a ball milled sample remain fast after the sample has been cycled a few times [96]. This indicates that the improvements in the ball milled samples should be sought in the reduction of the particle size, rather than in side effects of the ball milling (i.e. defects and the presence of the high pressure γ-phase).
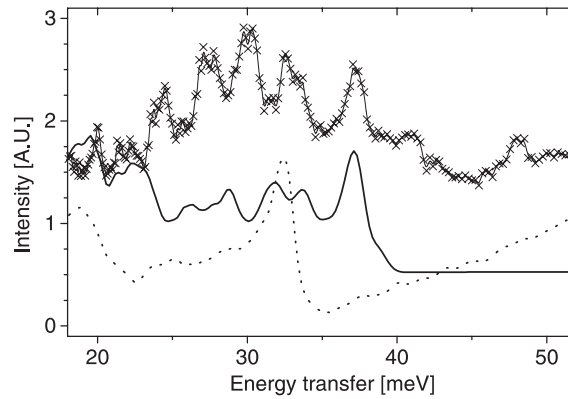
Figure E.4: The vibrational spectrum of ball milled magnesium hydride (top line with crosses) with calculated spectra for γ MgH2 (bottom solid line) and β MgH$_2$ (bottom dotted line). The calculated spectra are enlarged by a factor 10 with respect to the scale used in figure E.3. The ratio between β and γ-phase in the ball milled sample samples might be as high as 50%.

E.4 Conclusions

Ball milled and bulk magnesium hydride has been studied with vibrational spectroscopy. Using Density Functional computer calculations, it is now possible to reproduce the spectrum of bulk MgH_2 accurately. The spectrum which results after ball milling shows a distribution in stresses over the sample. Calculations where stresses were induced have been performed showing that key features in the spectrum are sensitive to a distribution of stresses in the sample. It was found that the high energy part of the vibrational spectrum is rather sensitive to stresses induced by for instance ball milling. Certain phases whose spectra exhibit large stress-dependence might be invisible in the high energy part (i.e. above 50 meV) of the inelastic spectrum. However, vibrational spectroscopy together with density functional frequency calculations provide answers to questions relating to structure not available with diffraction methods. Especially in the field of nanoscale-science, vibrational spectroscopy reveals information which is difficult or impossible to extract from broad diffraction lines. Cycling of the hydrogen content of the sample returns the vibrational spectrum of bulk magnesium hydride, while the particle size remains small. This shows that cycling of the hydrogen content anneals the structure. We conclude that the enhanced hydrogen sorption and desorption kinetics are mainly due to the reduction of the particle size and not due to stresses and defects. We predict that the same improvement will be found in nanosized magnesium samples prepared by other means.

Acknowlegdement

Appendix F

Hydrogen in magnesium metal (alpha phase) observed using neutron diffraction and simulations

H.G. Schimmel, G.J. Kearley, J. Huot and F.M. Mulder, submitted to *Journal of Alloys and Compounds*

Abstract

Hydrogen diffusion through magnesium metal is one of the rate determining steps for sorption kinetics of magnesium. From known Gibbs free energies for the magnesium-hydrogen system we have calculated the concentration x of hydrogen in MgH_x in equilibrium with MgH_2: $x = 1.13 \cdot 10^{-3}$ at 673 K, which has been verified by experiments. From an ab-initio dynamical simulation we obtained the position of hydrogen in magnesium metal (mostly in tetrahedral sites), the Debye-Waller factors (0.06 Å^2 for tetrahedral sites and 0.08 Å^2 for octahedral sites) and the diffusion constant $D = 6.6 \cdot 10^{-9}$ m^2/s at 673 K.

F.1   Introduction

Hydrogen storage in light metals and alloys is interesting for mobile applications of hydrogen as an energy carrier. Until now the ideal metal alloy has not been found[8, 149]. The search for new materials or new treatments for existing compounds is being undertaken by many scientists. Because of their low density, Mg and Mg$_2$Ni currently draw interest. However, the application of magnesium metal as a hydrogen storage compound is hampered by the slow dynamics at moderate temperatures so that operation temperatures above 350 degrees Celsius are necessary for bulk materials. Magnesium may be loaded with hydrogen to form MgH$_2$, which possesses a reversible storage capacity by weight of about 7%. It has been shown that a ball

milling treatment increases the dynamics of hydrogen sorption by magnesium by about a factor of 10, and a further increase may be achieved by the addition of catalysts such as V and Nb[76] or metal oxides[93]. Measurements on ball milled MgH_2+5 at% V indicate that the nucleation and grow process is important for this material, but long range diffusion plays also a role, especially when the driving force is small[91]. After the splitting of hydrogen molecules in atoms, hydrogen atoms have to diffuse through magnesium metal to a magnesium hydride nucleus (the transport properties of MgH_2 are generally expected to be very poor). This paper focusses on the diffusion of hydrogen through Mg metal. New results on the location and dynamics of hydrogen in the magnesium metal (α phase) will be reported, based on ab-initio simulations and supported by experiment. First we calculate the amount of hydrogen in magnesium alpha using thermodynamical data. This amount of hydrogen is also found present our diffraction spectrum. From the ab-initio calculations we derive the positions of hydrogen, its Debye-Waller factor and the microscopic diffusion constants, which are in accordance with experiment.

F.2   Experimental

Magnesium metal powder was obtained from AlfaAesar and magnesium hydride (99%, remainder magnesium) powder was obtained from Aldrich chemicals.

F.2.1   Neutron scattering

The concentration of hydrogen in the metal magnesium phase could be determined from the diffraction peak which was measured on the neutron scattering spectrometer OSIRIS (ISIS spallation source, UK). We used cylindrical stainless steel containers with inner diameter of 26 mm and a wall thickness of 0.8 mm. The container was filled with as-bought magnesium metal powder. The background runs were taken first, after which the cans were opened and magnesium hydride powder was added. By putting MgH_2 on top we made sure that the equilibrium pressure of MgH_2 at the measurement temperature was present in our sample. In this way the amount of hydrogen present in α-Mg resembles the amount present during hydride formation, without actually forming magnesium hydride (β-MgH_2). These containers were used up to a temperature of 673 K. We note that after cooling down a pressure may remain in such containers because equilibrium is not always preserved during cooling. The beam was not illuminating the MgH_2 at the top of the sample. Since the same metal powder and container with and without a hydrogen atmosphere was put into the beam, we were able to find the scattering exclusively due to hydrogen by subtraction. The diffraction spectrum shows a magnesium metal diffraction peak at a d-spacing of 2.81 Å.
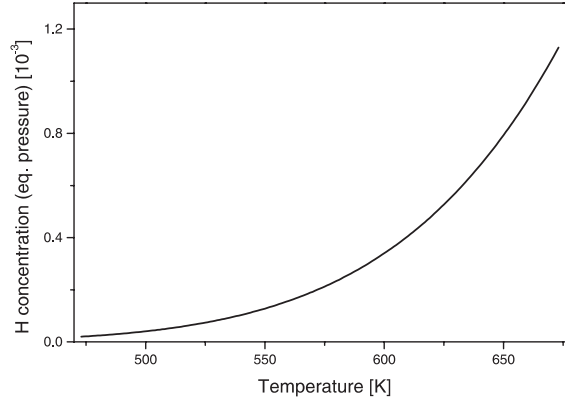
Figure F.1: The concentration of hydrogen in the α-phase of magnesium as a function of temperature in equilibrium with H_2 gas and MgH_2 at the same temperature.

F.2.2 Density functional calculations

Ab-initio computer calculations were performed on a PC-cluster using density functional theory as implemented in the VASP code.[101] A supercell of 3*3*2 unit cells (space group 194, a=3.250 Å, c=5.276 Å), with one hydrogen atom per supercell was used. One k-point, an energy cutoff of 200 eV and LDA PAW-potentials were applied.[127] The energy difference between two typical confirmations was off by 10% with respect to a high precision calculation using a 4*4*4 k-point-grid and a cutoff of 250 eV. The Methfessel-Paxton method with a SIGMA of 0.6 was used to model the occupation of bands around the Fermi level. With a timestep of 1 fs, a molecular dynamics simulation was run of 20 ps.

F.3 Results and discussion

A precise thermodynamic modelling of the magnesium hydrogen system was performed by Zeng at al.[104] They calculated the Gibbs free energies for all phases of the Mg-H system as a function of temperature and gas pressure. The Mg-α phase is described with a sublattice model $(Mg)_1(H,Va)_{0.5}$. When there is equilibrium between the metal α-Mg phase and Mg+H_2, the Gibbs free energies per mole of MgH_x and Mg+H_2 are equal. Inserting the dependence of the equilibrium pressure of MgH_2 on temperature (which can be found in the same way), we can evaluate the concentration x of hydrogen in MgH_x in equilibrium with H_2 gas and MgH_2. A graph is shown in figure F.1. We calculate $x = 1.13 \cdot 10^{-3}$ at 673 K. The calculated points can be approximated by $x = 20 \exp(-54800/RT)$.

The diffraction spectrum is shown in figure F.2 for pure magnesium and for magnesium in a hydrogen atmosphere. Two observations can be made: 1) the background is increased for the hydrogen containing sample and 2) the peak area is lower. From the area of the peak compared to the difference in background
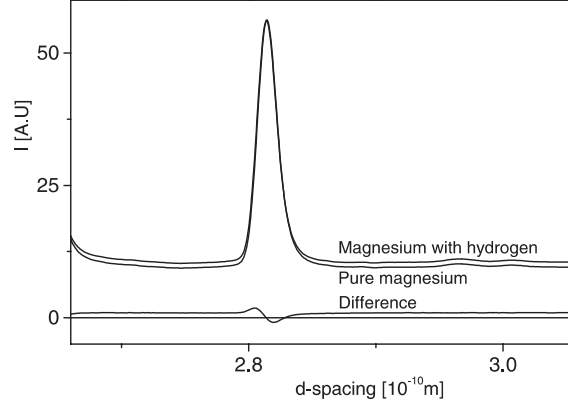
Figure F.2: The first diffraction peak which was recorded on OSIRIS during the quasi-elastic measurements at 673 K. The line with the highest base is from magnesium metal under an equilibrium pressure of MgH_2 at 673 K (17.6 bar). The line with a lower base is from pure magnesium at 673 K without a hydrogen atmosphere. The difference (bottom line) shows that the incoherent background increases, the line area decreases and the line position shifts to higher d-spacing. From this figure a hydrogen concentration x in MgH_x of $1.2 \cdot 10^{-3}$ was calculated.

scattering (which we attribute entirely to extra incoherent scattering by hydrogen), the crystal structure of magnesium metal and the neutron scattering cross-sections of hydrogen and magnesium, we calculate $x = (1.2 \pm 0.2) \cdot 10^{-3}$, which agrees with the thermodynamic considerations above.

As for the dynamic part it is known that the diffusion coefficients of hydrogen in magnesium at 673 K may be as high as $2 \cdot 10^{-8}$ m^2/s ($D = 1.54 \cdot 10^{-6} \exp(-24100/RT)$[105]) or $3 \cdot 10^{-9}$ m^2/s ($D = 3.8 \cdot 10^{-6} \exp(-40000/RT)$[92]). Our ab-initio computer calculations show that hydrogen diffuses through the metal by jumps between octahedral and/or tetrahedral sites. During the 20 ps of the simulation, the hydrogen atom spent roughly 5 ps on octahedral and intermediate positions and 15 ps on tetrahedral positions. Figure F.3 shows the path of the hydrogen atom in space during the simulation viewed along the crystallographic a-axis. The figure shows clearly that the hydrogen atom moves on a sub-picosecond time-scale between the two adjacent tetrahedral sites (Wyckoff site 4f) which are separated by 1.3 Å in the z-direction (i.e. along the c-axis). Jumps from the set of tetrahedral sites towards neighboring octahedral sites (Wyckoff site 2a) at a distance of 2.0 Å occur as well. Furthermore direct jumps in the direction of the c-axis between two octahedral sites, which are 2.6 Å apart, are observed. From the animation of the motions, it becomes clear that once the hydrogen atom escapes from a site, it may travel over quite a distance before it settles down in a new site (i.e. the jumps may be correlated).

The Debye-Waller factor $U = \langle (u_q - \langle u \rangle)^2 \rangle$, where u_q is the inner product of the displacement u and the momentum transfer vector q, of magnesium is 0.05 Å^2, which agrees with the value of 0.047 Å^2 from recent experiments.[150] The mean square displacement of the hydrogen atom during the time that it stays in a certain site are about 0.06 Å^2 for the tetrahedral sites and 0.08 Å^2 for the octahedral sites.
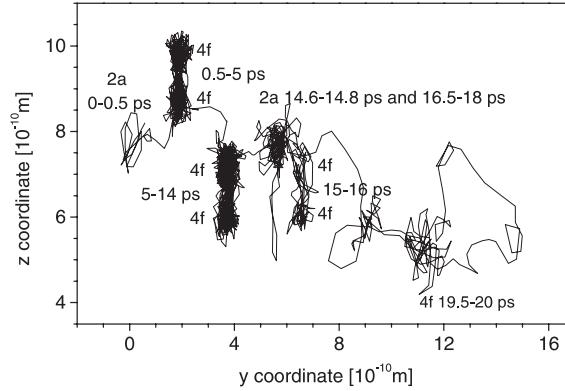
Figure F.3: During the 20 ps ab-initio molecular simulation, the hydrogen atom followed this trajectory through the magnesium lattice, shown in a (cartesian) projection along the a-axis (i.e. along x). Hydrogen exchanges on a sub-picosecond timescale between the two tetrahedral sites which are separated by 1.3 Å. Jumps between octahedral (2a) and tetrahedral (4f) sites occur on average every 2 ps. Some jumps over larger distances occur. The line is drawn between positions which are separated by 10 fs simulation time.

When only one trajectory is available, an estimate for the diffusion coefficient D is

$$D = \frac{\vec{r}^2}{2dt} \qquad (F.1)$$

using the distance from the starting point r, simulation time t and the dimensionality of the system d ($d = 3$). We find a diffusion constant of $D = 6.6 \cdot 10^{-9}$ m^2/s in agreement with the values quoted earlier.

Fick's first law states $J = -D \, dc/dx$, connecting the flux J, the diffusion constant D and the concentration gradient dc/dx. According to this law, it takes approximately 1.2 s to transport the amount of hydrogen in 1 μm^3 MgH$_2$ via a magnesium metal cube of 1 μm^3. The diffusion constant evaluated here and a concentration difference of $2.5 \cdot 10^{-4}$ was used (which means that about 1.5 times the equilibrium pressure has been applied). Under these conditions the diffusion is very fast, and other factors such as the dissociation and nucleation processes are rate limiting. The hydrogen flux is determined by the diffusion coefficient and the concentration gradient. When the pressure is kept constant, the concentration shows a weak dependence on temperature as the ratio between the applied and equilibrium pressures increases. The temperature dependence of the diffusion constant basically determines the flux of hydrogen atoms through magnesium at different temperatures and constant pressure. The diffusion path area may be much smaller than the particle size if hydrogen enters the particle via a small number of gateways: places where a catalyst particles is present on the surface. We note that for desorption the situation is different as the vacuum is a lower limit. For desorption we estimate a flux which scales as $\exp(-(87 \pm 8) \cdot 10^3/RT)$, meaning that it halves every 30 K around 650 K.

F.4   Conclusion

In this manuscript we show that the concentration of hydrogen in magnesium is about 0.1 percent for magnesium in equilibrium with hydrogen gas and magnesium hydride around 673 K. From ab-initio computer simulations we calculate a diffusion constant in agreement with previously published values. For large particles at low temperatures the diffusion of hydrogen through the metal might be rate-limiting when small catalyst particles on the surface limit the cross section of the diffusion channels.

Appendix G

In-situ neutron diffraction during hydrogen cycling of niobium-catalyzed magnesium

H.G. Schimmel, J. Huot, L.C. Chapon and F.M. Mulder, *to be submitted*, (2005).

G.1 Introduction

A *conditio sine qua non* for the development of sustainable technologies for the hydrogen economy is the availability of an economical, safe and practical hydrogen storage mechanism. Since hydrogen gas can be used as a clean fuel both in conventional combustion engines and in fuel cells, it has a large potential as an energy carrier. Hydrogen is a very light and volatile gas, which forces the use of low temperatures, high pressures, a sorption material or a combination of these to store a practical amount of hydrogen (6 wt% in the year 2010 according to the demand of the department of energy of the USA). Hydrogen storage in magnesium metal is interesting from a practical viewpoint as it stores approximately 7 wt% of hydrogen reproducible and reversible. On hydriding magnesium forms magnesium hydride, MgH_2, which is an insulating and transparent solid. Its use is at present hampered by the high absorption enthalpy and the slow kinetics, which makes it practical only at temperatures above 300 degrees Celsius. By means of a ball milling treatment the particle size can be reduced, which speeds the sorption properties by a factor 10. The addition of a catalyst like V or Nb is known to increase the kinetics by another order of magnitude [95, 96, 76].

G.1.1 Kinetic factors for magnesium hydriding

Magnesium metal transforms into magnesium hydride in a gas-solid transition. The driving force for this process scales with the square root of the difference between the equilibrium pressure of magnesium hydride and the pressure that is actually applied.

The hydriding process involves several steps: 1) gas permeation through the particle bed, 2) surface adsorption, 3) hydrogen dissociation, 4) migration of hydrogen atoms from the surface into the bulk, 5) diffusion through the bulk metal and finally 6) nucleation and growth of the hydride phase. Each of these steps might be rate-limiting. The ball milling method speeds the kinetics up and decreases the particle size, which increases the specific surface area, decreases through-particle diffusion path lengths and introduces a high density of defects and distortions. Previously, we have shown that the defects and distortions in the magnesium hydride structure play no decisive role in the increase of the sorption speed as they are annealed when the hydrogen content is cycled, while the kinetics remain fast [100, 103].

The main contributions to the increase in speed are therefore sought in the increase of the specific surface area, the decrease of diffusion path lengths, and factors concerning nucleation and growth. Nb and V catalysts are known for their catalytic activity in the third step (hydrogen activation and bond cleavage) in the absorption process. Mg does not form alloys or intermetallic compounds with Nb or V [151]. Thus when preparing Nb catalyzed Mg samples, one does not expect to mix Mg and Nb. Detailed information on the processes during the hydriding reactions in catalyzed magnesium is needed for a further optimization of magnesium as a hydrogen storage material. Besides that, more knowledge of the limitations of the hydriding reaction kinetics is important for all hydrogen storage compounds where gas-solid reactions play a role. In previous work the Nb phase has been observed using X-ray diffraction [94, 110] and a solid solution gateway phase of niobium was found. We performed a time-dependent, *in situ* neutron diffraction study on the hydriding and dehydriding properties of ball milled and catalyzed $MgNb_{0.05}H_2$. In contrast to the X-ray experiments, the use of neutrons enabled us to locate hydrogen in the structures and refine hydrogen site occupancies. We will show that this improves the understanding of the Mg-Nb-H system.

G.1.2   The $MgNb_{0.05}$–H system

Since it is known that Mg and Nb do not alloy, thermodynamically we have two parallel systems: the Mg-H system and the Nb-H system. Gibb's phase rule states that only one parameter determines the state of a system when three phases play a role, in the first case magnesium metal, magnesium hydride and hydrogen gas. The Mg-H system has therefore a characteristic equilibrium pressure at each temperature. We note that the magnesium metal phase contains hydrogen in very limited amounts (a composition of about $MgH_{\sim 0.001}$ is typical around 400 degrees Celsius [107]). In general such a hydrogen-saturated metal phase is denoted the α-phase and the hydride phase is called the β-phase.

At room temperature niobium metal possesses an α-phase which contains hydrogen up to a concentration of $NbH_{0.25}$. It is a metallic hydride which possesses the typical $\alpha - \alpha'$ transition such as present in other metallic hydrides like palladium. In analogy to a gas-to-liquid transition a critical point is present at 171 degrees Celsius

[152]. Under our experimental conditions the niobium particles are above their critical point and the α-phase may contain hydrogen up to the composition NbH_x, with $0 < x < 1$, depending on the pressure. The Nb-H system has two phases and this means that the hydrogen content of the Nb α phase adjusts itself to the hydrogen pressure, which is dictated by the equilibrium pressures of the Mg-H system.

Experimental section Magnesium hydride powder and niobium metal powder has been ball-milled by a Spex 8000 ball milling apparatus for 20 hours. We loaded 2.15 g of $MgNb_{0.05}H_2$ sample under an inert atmosphere in a silica glass tube that was connected to a gas-handling system. After heating to 350 degrees Celsius hydrogen gas was first released from the cell under the equilibrium pressure with a controlled constant hydrogen flow. Deuterium was then loaded as this isotope provides a better contrast in neutron diffraction experiments. Successive release of deuterium and finally the loading of hydrogen completed the experiment. Diffraction spectra were measured during all these stages of H unloading, D loading and unloading and finally H loading. This manuscript deals with the loading-unloading cycle with deuterium, while the spectra of the hydrogen containing materials confirm that the results also hold for the hydrides.

The loading of deuterium gas was performed at a temperature of 320 degrees Celsius and mostly at a pressure around 4-5 bar, finishing at 11 bar, much higher than the equilibrium pressure of 2.5 bar at this temperature. A neutron diffraction pattern was recorded for each of the 20 steps in the loading process. From a calibrated volume at room temperature and the pressure drop in it, the amount of hydrogen that was absorbed in the magnesium sample was determined. During unloading, also at a constant temperature of 320 degrees Celsius, deuterium was released by evacuating the silica sample cell. The desorption rate was kept constant at 5 ml/min (STP conditions; 1 bar, RT), and pressures were recorded. A diffraction pattern was acquired every 3 minutes and a total of 83 patterns was taken.

GEM is a high intensity neutron diffractometer at the spallation source ISIS at the Rutherford Appleton Laboratories in the United Kingdom [153]. A pulsed beam of neutrons with a range of wavelengths is incident on the sample. Neutrons are scattered mainly elastically (diffraction) and are counted in ≈ 7000 detectors that are positioned around the sample. From the time of flight of the neutron, the path length, and the detector position, the velocity, momentum transfer Q and the d-spacing $d = 2\pi/Q$ can be calculated. The diffraction detectors are grouped into 7 banks, each with a different d-spacing range. GEM combines an unprecedented neutron count rate with a very large Q range and good resolution, facilitating detailed *in situ* measurements.

G.2 Experimental results and analysis

A complete hydriding-dehydriding cycle was obtained as described in the experimental section. The spectra obtained during dehydriding are shown as a color plot in figure G.1 together with the hydride fraction as a function of time. All spectra of the complete cycle were sequentially fitted using the Sequenz shell that generates input files for, and runs, the Rietveldt refinement program GSAS. Five phases could
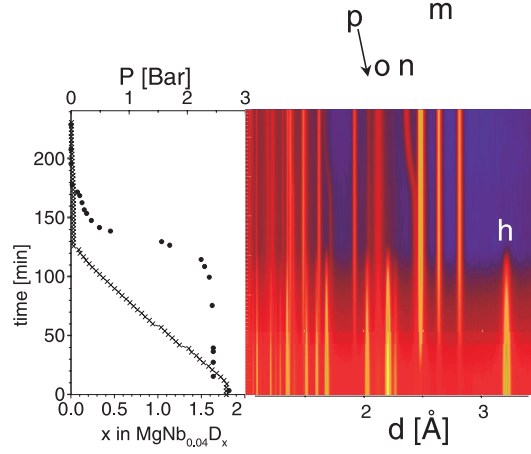
Figure G.1: Image of neutron diffraction patterns during the dehydriding process, including plots of the fitted amount of deuterium and the gas pressure as a function of desorption time.

be identified in the spectra: magnesium metal, magnesium hydride, magnesium oxide, α-niobium and a small, but clearly visible and identifiable contribution from a phase which we discuss below.

From the fits we obtained the phase fractions, lattice parameters, site occupancies, temperature factors and line widths, the latter being determined by the effective particle size and the strain in the particles. The phase fractions, hydrogen occupancies and lattice parameters of the different phases are plotted as a function of the effective composition $MgNb_{0.05}D_{D_{tot}}$ in figure G.2.

We start the discussion of our results at the hydriding process (triangles in figure G.2). The first result that draws our attention is that the volume of the unit cell of magnesium (hexagonal space-group $P6_3/mmc$) starts to increase by about 0.05 Å^3 per unit cell when the loading with deuterium starts. The fact that deuterium enters the magnesium metal phase will increase the volume of the unit cell due to the extra volume of the hydrogen atom which is generally assumed to be 2-3 Å^3 per hydrogen atom [73]. However, the expansion that we observe is much larger than expected from the composition $MgH_{0.001}$ and has to be attributed mainly to temperature effects induced by the energy released during hydrogen absorption. This occurs inside the bulky sample, notwithstanding the fact that the temperature regulation was constant within ± 1 K. The linear thermal expansion coefficient of magnesium metal at these temperatures is $30 \cdot 10^{-6}$/K [150]. This means that the volumetric expansion is about $90 \cdot 10^{-6}$/K, from which it is easily derived that the temperature
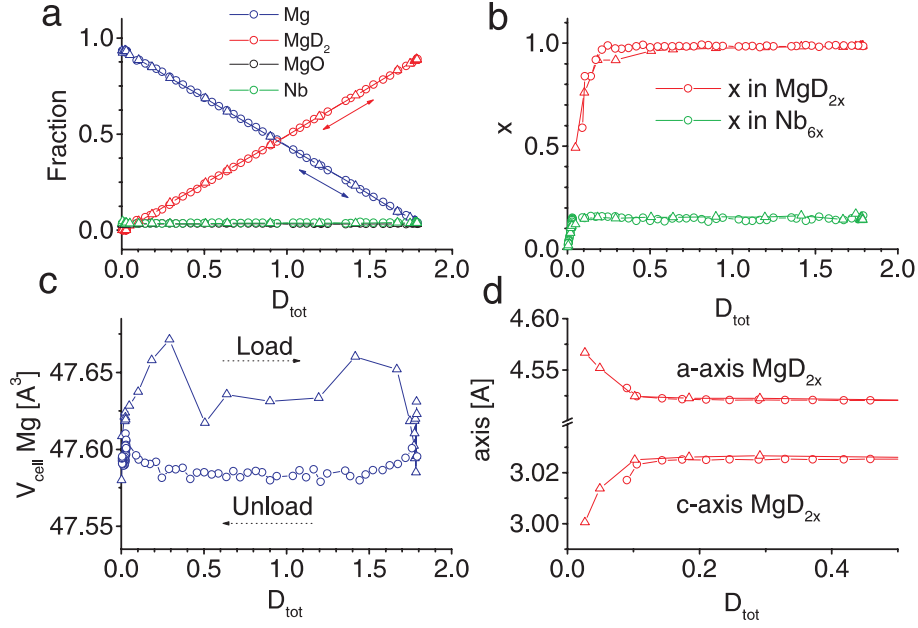
Figure G.2: Lattice parameters and D site occupancies of Mg and MgD_2 as a function of deuterium fraction.

of the magnesium metal has to increase by about 12 K to show this effect. The peak in the unit cell volume at a loading of 0.2 may indicate that initially the temperature rise is quite high as the heater circuit has to adopt to the situation in which heat is generated in the sample. The other phases in the system show a similar dependence of the unit cell volume during hydrogen cycling. The occurrence of a temperature rise upon hydrogen loading will clearly counteract the hydrogen adsorption because the equilibrium pressure for adsorption increases steeply with temperature. This will cause an immediate reduction of the adsorption speed, as well as a reduced nucleation rate for new MgD_2 crystallites (see also the discussion below).

Next, we like to draw the attention of the reader to the parameters of the hydride phase when the concentration of the hydride phase is low. We see that 1) the site occupancy y of deuterium in MgD_{2y} decreases to about $y = 0.5$, much lower than its stoichiometric value $y = 1$, and 2) the a and b axes of the unit cell decrease, while the c-axis becomes longer. Above an effective sample composition $D_{tot}=0.3$, the magnesium hydride phase (more exact, its deuterided form, which has the same rutile-type space-group $P4_2/mmm$) converges to the usual values for the unit cell and occupation parameters, which remain constant from then on. In the analysis it was also considered to have a separate $MgD_{2y<2}$ phase for loadings higher than $D_{tot}=0.3$ next to a stoichiometric MgD_2 phase, but this appeared not to be necessary. The same hydrogen deficient $MgH_{2y<2}$ phase is observed in the fully protonated sample.

At an effective concentration of $MgNb_{0.05}D_{1.8}$ we started the unloading of our
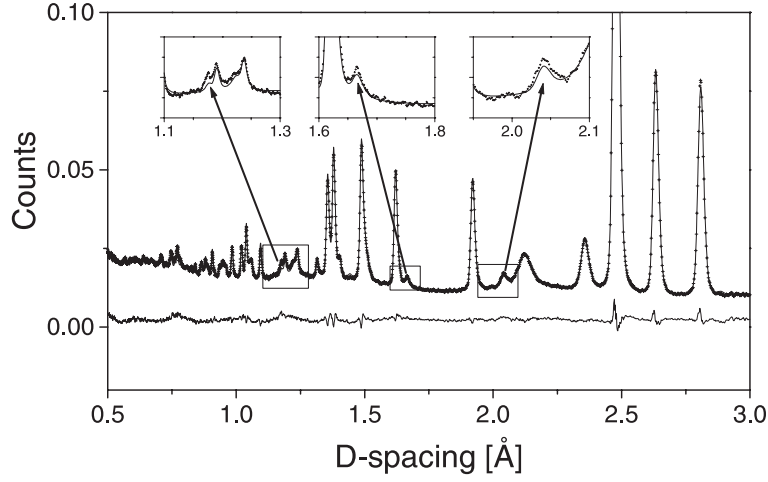
Figure G.3: Rietveldt refinement of the fully dehydrided sample. Two unique peaks that belong to the perovskite phase are indicated by the arrows in the insets.

sample. The spectra taken during desorption with a rate of 5 ml D_2 per minute are plotted from the bottom upwards in figure G.1. The first few diffraction spectra show the spectrum of magnesium hydride, because first the pressure in the sample container is reduced from 11 bar to the plateau pressure of ≈ 2 bar. After that, hydrogen is extracted from the hydride itself, and the magnesium metal phase appears. Since the incoherent cross-section of deuterium for neutrons contributes significantly to the background level, we observe a considerable decrease of the background level during dehydriding. When this background and the magnesium deuteride phase fraction are low enough, the α-Nb phase diffraction peaks become clearly resolved, although they can be fitted consistently in all of the spectra. In the last stage, the pressure becomes lower than the equilibrium pressure of NbD_x (which is about 0.1 bar at this temperature), which then converts to pure Nb metal (the deuterium content of the Nb metal phase is directly related to the D_2 pressure in the sample at low pressures). The lattice of NbD_x shrinks when its deuterium content, x, is reduced, which is clearly visible in the s-shape around $d = 2.4$ Å and 1.7 Å in the upper part of the color plot. Note that when NbD_x releases its D, the MgD_2 has vanished already completely since the equilibrium pressure of NbD_x is much lower than that of MgD_2 for small values of x. This means that for the actual catalytic hydrogen splitting into atoms one should consider NbD to be the more relevant phase.

Finally we observe a small peak at a d-spacing of 2.035 Å which does not belong to one of the known phases. A careful observation of the spectra shows that more peaks are present at smaller d-spacings in the patterns. Three peaks are identifiable by eye: at 2.035 Å, 1.661 Å and 1.175 Å. So we find reflections at 4.07 divided by 2, $\sqrt{6}$ and $\sqrt{12}$, which points towards a cubic phase. We found that known compounds such as $Pb(Mg_{0.333}Nb_{0.667})O_3$ [154, 155], $SrNbO_3$ [156] and $BaNbO_3$ [157, 158] all

possess a cubic perovskite structure with lattice parameters around 4.05 Å at room temperature. Other cubic phases like cubic NbO, MgO all have a lattice parameter clearly larger than what is observed (they both possess a lattice parameter close to 4.21 Å). We propose that during the ball-milling process part of the Nb has been mixed with the outer oxide layers of the Mg particles leading to materials with the structure $Nb(Mg_{0.333}Nb_{0.667})O_3$. Because the peaks are best visible in the fully dehydrided spectra, we first analyzed these spectra carefully to be able to characterize this new phase in more detail. Subsequently all spectra were refined with this phase included. The refinements improved when this phase was added and the fitted phase fraction was constant for all spectra. Setting the molar amount of Mg metal to 100%, the sample contains 3.5% of Nb metal, 1.4% of $Nb(Mg_{0.333}Nb_{0.667})O_3$ and 3.2% of MgO, which leads to an effective sample composition: $MgNb_{0.057}O_{0.031}$. We give the data that were obtained from a fit using GSAS for this phase in table G.1.

Figure G.4 gives the different sub-spectra of the individual phases that occur in the measurements. Note that different D site occupations in NbD_x and MgD_x have an influence on the peak intensities of the respective phases. Because of the very high counting rate of GEM these intensities are determined very accurately. The perovskite phase has only a small number of peaks of which several are overlapping with those of other phases. This explains why we can assign only a few peaks uniquely to this phase without fitting.

## G.3   Discussion and conclusions

Hydrogen depleted MgH$_2$

We have obtained detailed *in situ* information on the phases that are involved when the deuterium content of magnesium particles is cycled. The first patterns of the hydriding part, where the hydride phase is becoming increasingly observable, contain a hydride phase that differs significantly from the stoichiometric phase with respect to the hydrogen occupancy and its unit cell shape. Such a distorted phase may be present as the first stages of nucleation of the hydride phase and/or at the boundary between magnesium metal and magnesium hydride. The observation of Vigeholm et al. [86] that diffusion occurs along the hydride-metal interface is consistent with this finding as such a distorted phase may exhibit a much faster diffusion of hydrogen due to the large concentration of hydrogen vacancies.

Heat effects

We now discuss our observation of an increase in the unit cell volume of Mg that corresponds to a temperature rise of 12 K. We pose the following, realistic, situation: a bed of particles is brought at a temperature of 320 degrees Celsius and a pressure $P_a = 5$ bar of twice the equilibrium pressure, P_{eq}, is applied. On the application of

Table G.1: Parameters of the phases observed during deuterium cycling of Nb catalyzed and ball milled MgD_2.

MgD_2			
Lattice parameter	a,b=4.530 Å, c=3.025 Å		
Space group	$P4_2/mnm$	No. 136 (tetragonal)	
Atom site in Wyckoff notation	Mg:	2a	(0,0,0)
	D:	4f	(0.3044,0.3044,0)
Occupancy	Mg: 1.000		
	D: 1.000		
$MgD_{1.2}$			
Lattice parameter	a,b=4.56 Å, c=3.00 Å		
Space group	$P4_2/mnm$	No. 136 (tetragonal)	
Atom site in Wyckoff notation	Mg:	2a	(0,0,0)
	D:	4f	(0.3044,0.3044,0)
Occupancy	Mg: 1.000		
	D: 0.6		
Mg			
Lattice parameter	a,b=3.235 Å, c=5.253 Å		
Space group	$P6_3/mmc$	No. 194 (hexagonal)	
Atom site in Wyckoff notation	Mg:	2c	(1/3,2/3,1/4)
Occupancy	Mg: 1.000		
Nb			
Lattice parameter	a=3.324 Å		
Space group	$Im\bar{3}m$	No. 229 (body centered cubic)	
Atom site in Wyckoff notation	Nb:	2a	(0,0,0)
Occupancy	Nb: 1.000		
NbD			
Lattice parameter	a=3.44 Å		
Space group	$Im\bar{3}m$	No. 229 (solid solution bcc)	
Atom site in Wyckoff notation	Nb:	2a	(0,0,0)
	D:	12d	(1/4,0,1/2)
Occupancy	Nb: 1.000		
	D: 0.16		
$Nb(Mg_{0.333}Nb_{0.667})O_3$			
Lattice parameter	a=4.070 Å		
Space group	$Pm\bar{3}m$	No. 221 (cubic perovskite)	
Atom site in Wyckoff notation	Nb:	1a	(0,0,0)
	Nb,Mg:	1b	(1/2,1/2,1/2)
	O:	3c	(0,1/2,1/2)
Occupancy	Nb: 1.00		
	Nb: 0.7, Mg: 0.3		
	O: 1.00		
MgO			
Lattice parameter	a=4.227 Å		
Space group	$Fm\bar{3}m$	No. 225 (cubic)	
Atom site in Wyckoff notation	Mg:	4a	(0,0,0)
	O:	4b	(1/2,1/2,1/2)
Occupancy	Mg: 1.000		
	O: 1.000		
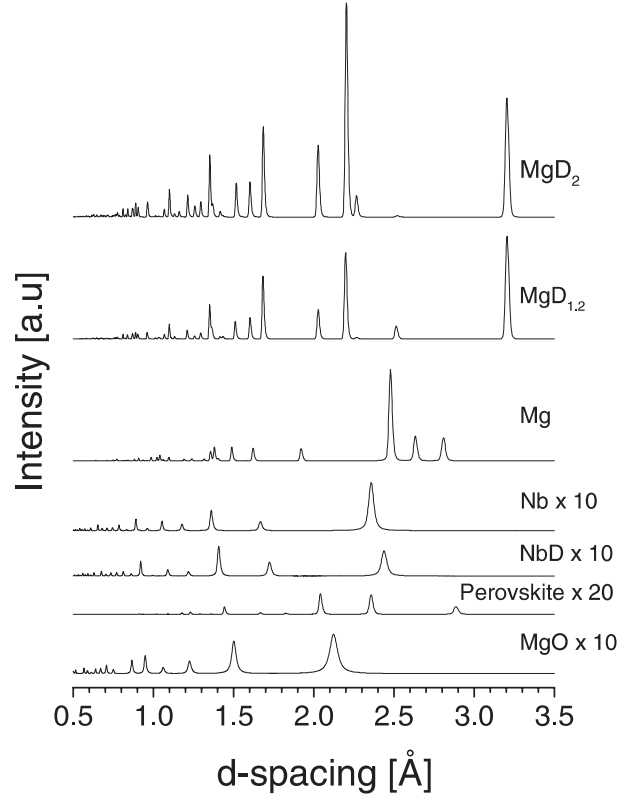
Figure G.4: Plot of the sub-spectra identified in the Nb catalyzed Mg-H system. We show from top to bottom simulated spectra of MgD_2, $MgD_{1.2}$, Mg, Nb, NbD, $Nb(Mg_{0.333}Nb_{0.667})O_3$ and MgO using the parameters from the fits (the thermal factors and line widths are as observed in the measurements).

the pressure, the magnesium metal α-phase will first start to saturate with hydrogen atoms. After a certain time, the hydride phase will nucleate somewhere in the particle. This hydride phase will grow as there exists a driving from the over pressure. Since magnesium hydride is an insulator, the heat, that is generate at the boundary, distributes over the remaining magnesium metal (α-phase). Due to the temperature rise which then occurs, the equilibrium pressure of the particle rises, thus the driving force for new nucleations decreases and the chance of a new nucleation elsewhere in the particle decreases rapidly.

Consider a particle containing N_p mole magnesium atoms of which a fraction, f, has been converted to magnesium hydride. The heat that is released by the conversion to the hydride phase is $H_f = f H_{MgH_2} N_p$, where H_{MgH_2} is the formation enthalpy of magnesium hydride, 74.5 kJ/mol. The heat will increase the temperature of the magnesium particle by $\Delta T = H_f/(M_{Mg} C_{Mg} N_p)$, using the molar mass of magnesium $M_{Mg} = 0.0243$ kg/mol and the heat capacity $C_{Mg} = 1026$ J/(kg K). The equilibrium pressure becomes equal to the applied pressure (which we assumed to be two times the equilibrium pressure initially) when the temperature of the

magnesium particle increases by about $\Delta T = 30$ K (for temperatures around 593 K, for lower temperatures ΔT is lower). Now that we know all parameters, we can calculate $f = \Delta T M_{Mg} C_{Mg} / H_{MgH_2} = 1\%$. We conclude that when just 1% of a Mg particle transforms to MgH_2 the heat that is freed makes the driving force zero due to the temperature-rise of the particle. Only when this heat has been dissipated, a driving force exists again and more hydrogen may adsorb. This shows that heat transfer is not only important for engineering sized batches, but also for microscopic nucleation behavior.

The role of NbH

In contrast to the X-ray experiments of Pelletier et al. and Yavari et al., we did not find the $NbH_{0.6}$ gateway phase. We think that their finding is merely indicating that the pressure in the sample is relatively high during desorption when high desorption rates are used because the hydrogen gas experiences a rather larger barrier when diffusing through the particle bed to the vacuum. We find that during the complete Mg hydrogen cycling stage, NbH is present. Since the addition of Nb catalyzes not only the desorption reaction, but also the absorption process, we think that the catalytic properties of NbH rather than those of Nb metal need further investigation under real conditions, that is high temperature (above the critical point for the α-α' transition) and high pressure.

Nb(Nb,Mg)O$_3$ perovskite a possible proton conductor?

The MgO phase is present on the surface of the Mg particles, even when the materials are always handled in an inert atmosphere. During (de-)sorption the MgO is a barrier for the transport of hydrogen. In this respect the small amount of the cubic Nb-Mg-O perovskite phase is an interesting finding. Such perovskites are known to transport hydrogen [111] and in addition may be catalysts themselves for the splitting of H_2. The perovskite phase, penetrating the MgO layer, could therefore be the missing part of the hydrogen transport pathway.

The perovskite phase is apparently present with particle sizes some two times larger than the average MgO particle size. Apart from this perovskite form, which may result from mixing of Nb into larger MgO particles, it is likely that part of the MgO in the surface layer is substituted by such a $MgNbO_3$ perovskite phase. The finding of such transition metal MgO mixed oxide phases may be more general. Oxides such as Cr_2O_3, V_2O_5, Fe_3O_4 [93] and Nb_2O_5 [159] are known to catalyze the hydrogen splitting at the surface of for instance magnesium, as well as some pure metals like V and Nb [109]. Because all these transition metals T form compounds of the form $Mg_x T_y O_z$, it is interesting to investigate the catalytic activity of these compounds too. It may be noted that Mg-T-O compounds like $Mg_3V_xO_8$ are well known catalysts used for hydrogenation reactions in the petrochemical industry [160, 161].

Conclusions

We conclude that the *in situ* neutron diffraction experiments we report here give much in-depth information on the underlying processes for absorption of hydrogen in metals in general and in magnesium in particular. We especially point out the importance of the heat effects that counteract the nucleation and hydrogenation reaction, even on the size of a single grain. A factor that enhances sorption speeds is the defect hydride structure that we found at the low hydrogen concentrations. Under conditions relevant for absorption and desorption NbH was shown to be the relevant Nb hydride phase for the catalytic activity. In addition a new cubic perovskite phase with an estimated composition of $Nb(Mg_{0.333}Nb_{0.667})O_3$ was indicated that may also be catalytically active as well as proton transporting.

Outlook

The directions for modification of catalyzed magnesium compounds resulting from this work might be indicated as follows. The effect of the absorption heat on the driving force for absorption and the nucleation of the hydride appears to be a severe limiting factor in the absorption rates. This can only be altered by making the binding energy significantly lower, for instance by including other atoms in the lattice. Such lowered binding energy may in addition lead to some larger stability range of the H deficient $MgH_{<2}$ phase, which may then lead to fast hydrogen transport through the hydride phase (until such point that it becomes completely filled). Clearly one cannot add too much heavy elements to the compound without loosing its attractiveness. The transport of H through the Mg alpha phase does not appear as a rate-limiting step, because the high H diffusion speed makes up for the low H densities in this phase. Because the Nb phase is constantly saturated with H during the absorption process the splitting of hydrogen on its surface does not appear to be a rate-limiting step either; otherwise it would not be saturated. The observed mixing of MgO and Nb, and the formation of a new catalytically interesting phase in that way, appears to be an opportunity for further optimization of the materials.

Recently it has been show that the addition of scandium to magnesium forms an alloy of which the hydride is less stable than magnesium hydride and possesses high diffusion coefficients of hydrogen atom through the hydride [162]. A mechanical alloying treatment of MgH_2, a transition metal T that forms stable compounds of the form Mg-T-O and another element (such as Sc) that alloys with Mg in such a way that it lowers the binding energy of H to the Mg alloy might provide a route for further improvements.

Acknowledgements

Bibliography

[1] Wakefield, E. H. *History of the electric automobile; battery-only powered cars.* Society of Automotive Engineers, (1994).

[2] Demirdöven, N. and Deutch, J. *Science* **305**, 974 (2004).

[3] Campbell, C. J. *Population and Environment* **24**, 193 (2002).

[4] *Oil and Gas Investor* **22** January (2002). Editor's comment.

[5] Aleklett, K. and Campbell, C. J. *Minerals and Energy - Raw Mat. Rep.* **18**, 5 (2003).

[6] Agency, I. E. *World energy outlook 2004.* (2004).

[7] Grove, W. R. *Phil. Trans. Royal Soc. London* **Part II, p. 91** (1843).

[8] Schlapbach, L. and Zuettel, A. *Nature* **414**, 353 (2001).

[9] Ogden, J. M. *Physics Today* , 69 April (2002).

[10] of Energy of the United States, D. http://www.eere.energy.gov/hydrogenandfuelcells/hydrogen/pdfs/technical_targets.pdf, (2004).

[11] Chase, M. W. *J. Phys. Chem. Ref. Data* **14 Suppl. 1** (1985).

[12] Lide, D. R. *Handbook of Chemistry and Physics.* CRC Press LLC, 79th edition, (1998).

[13] Li, Q. F., He, R. H., Berg, R. W., Hjuler, H. A., and Bjerrum, N. J. *Sol. State Ion.* **168**, 177 (2004). ; J. O. Jensen et al., MH2004 conf. proc. submitted to *J. All. Comp.*, 2005.

[14] London, F. *Z. Phys. Chem. B* **11**, 222 (1930).

[15] Carpetis, C. and Peschka, W. *Int. J. Hydrogen Energy* **5**, 539 (1980).

[16] Nijkamp, M. G., Raaymakers, J. E. M. J., van Dillen, A. J., and de Jong, K. P. *Appl. Phys. A* **72**, 619 (2001).

[17] Iijima, S. *Nature* **354**, 56 (1991).

[18] Dillon, A. C., Jones, K. M., Bekkedahl, T. A., Klang, C. H., Bethune, D. S., and Heben, M. J. *Nature* **386**, 377 (1997).

[19] Chambers, A., Park, C., Baker, R. T. K., and Rodriguez, N. M. *J. Phys. Chem. B* **102**, 4253 (1998).

[20] Park, C., Anderson, P. E., Chambers, A., Tan, C. D., Hidalgo, R., and Rodriguez, N. M. *J. Phys. Chem. B* **103**, 10572 (1999).

[21] Chen, P., Wu, X., Lin, J., and Tan, K. L. *Science* **285**, 91 (1999).

[22] Meregalli, V. and Parrinello, M. *Appl. Phys. A* **72**, 143 (2001).

[23] Cheng, H., Pez, G., Kern, G., Kresse, G., and Hafner, J. *J. Phys. Chem. B* **105**, 736 (2001).

[24] Cracknell, R. F. *Phys. Chem. Chem. Phys.* **3**, 2091 (2001).

[25] Gordon, P. A. and Saeger, R. B. *Ind. Eng. Chem. Res.* **38**, 4647 (1999).

[26] Wang, Q., Challa, S. R., Sholl, D. S., and Johnson, J. K. *Phys. Rev. Lett.* **82**, 956 (1999).

[27] Dodziuk, H. and Dolgonos, G. *Chem. Phys. Lett.* **356**, 79 (2002).

[28] Rzepka, M., Lamp, P., and de la Casa-Lillo, M. A. *J. Phys. Chem. B* **102**, 10894 (1998).

[29] C.C. Ahn, Y. Y., Ratnakumar, B. V., Witham, C., R. C. Bowman, J., and Fultz, B. *Appl. Phys. Lett.* **73**, 3378 (1998).

[30] Pinkerton, F. E., Wicke, B. G., Olk, C. H., Tibbets, G. G., Meisner, G. P., Meyer, M. S., and Herbst, J. F. *J. Phys. Chem. B* **104**, 9460 (2000).

[31] Hirscher, M., Becher, M., Haluska, M., Dettlaff-Weglikowska, U., Quintel, A., Duesberg, G., Choi, Y.-M., Downes, P., Hulman, M., Roth, S., Stepanek, I., and Bernier, P. *Appl. Phys. A* **72**, 129 (2001).

[32] Hirscher, M., Becher, M., Haluska, M., Quintel, A., Skakalova, V., Choi, Y.-M., Dettlaff-Weglikowska, U., Roth, S., Stepanek, I., Bernier, P., Leonhardt, A., and Fink, J. *J. All. and Comp.* **330-332**, 654 (2002).

[33] Liu, C., Yang, Q. H., Tong, Y., Cong, H. T., and Cheng, H. M. *Appl. Phys. Lett.* **80**, 2389 (2002).

[34] Liu, C., Fan, Y. Y., Liu, M., Cong, H. T., Cheng, H. M., and Dresselhaus, M. S. *Science* **286**, 1127 (1999).

[35] Stroebel, R., Joerissen, L., Schliermann, T., Trapp, V., Schuetz, W., Bohmhammel, K., Wolf, G., and Garche, J. *J. Pow. Sourc.* **84**, 221 (1999).

[36] Tibbetts, G. G., Meisner, G. P., and Olk, C. H. *Carbon* **29**, 2291 (2001).

[37] Ritschel, M., Uhlemann, M., Gutfleisch, O., Leonhardt, A., Graff, A., and Taeschner, C. *Appl. Phys. Lett.* **80**, 2985 (2002).

[38] Gundiah, G., Govindaraj, A., Rajalakshmi, N., Dhathathreyan, K. S., and Rao, C. N. R. *J. Mat. Chem.* **13**, 209 (2003).

[39] Schimmel, H. G., Kearley, G. J., Nijkamp, M. G., Visser, C. T., de Jong, K. P., and Mulder, F. M. *Chem. Eur. J.* **9**, 4764 (2003).

[40] Williams, K. A., Pradhan, B. K., Eklund, P. C., Kostov, M. K., and Cole, M. W. *Phys. Rev. Lett.* **88**, 165502 (2002).

[41] Pradhan, B. K., Sumanasekera, G. U., Adu, K. W., Romero, H. E., Williams, K. A., and Eklund, P. C. *Physica B* **323**, 115 (2002).

[42] Wang, Q. and Johnson, J. K. *J. Phys. Chem. B* **103**, 277 (1999).

[43] Wang, Q. and Johnson, J. K. *J. Phys. Chem. B* **110**, 577 (1999).

[44] Chan, S.-P., Chen, G., Gong, X. G., and Liu, Z.-H. *Phys. Rev. Lett.* **87**, 205502 (2001).

[45] Lee, S. M., An, K. H., Lee, Y. H., Seifert, G., and Frauenheim, T. *J. Am. Chem. Soc.* **123**, 5059 (2001).

[46] Vidali, G., Ihm, G., Kim, H.-Y., and Cole, M. W. *Surf. Science Rep.* **12**, 135 (1991).

[47] Silvera, I. F. *Rev. Mod. Phys.* **52**, 393 (1980).

[48] Fitzgerald, S. A., Yildirim, T., Saltodonato, L. J., Neumann, D. A., Copley, J. R. D., Rush, J. J., and Trouw, F. *Phys. Rev. B* **60**, 6439 (1999).

[49] Eckert, J. and Kubas, G. J. *J. Phys. Chem.* **97**, 2378 (1993).

[50] Brown, C. M., Yildirim, T., Neumann, D. A., Heben, M. J., Genett, T., Dillon, A. C., Alleman, J. L., and Fischer, J. E. *Chem. Phys. Lett.* **329**, 311 (2000).

[51] Ren, Y. and Price, D. L. *Appl. Phys. Lett.* **79**, 3684 (2001).

[52] Mojet, B. L., Eckert, J., van Santen, R. A., Albinati, A., and Lechner, R. E. *J. Am. Chem. Soc.* **123**, 8147 (2001).

[53] Conner, W. C. *Physical Adsorption: Experiment, Theory and Applications*, volume 491. Kluwer Academic, Boston (1997). edited by F. Fraissard, NATO ASI, Ser. C.

[54] Mulder, F. M., Schimmel, H. G., Plomp, J., and Bouwman, W. G. *To be published* (2005).

[55] Williams, K. A. and Eklund, P. C. *Chem. Phys. Lett.* **320**, 352 (2000).

[56] Adu, C. K. W., Sumanasekera, G. U., Pradhan, B. K., Romero, H. E., and Eklund, P. C. *Chem. Phys. Lett.* **337**, 31 (2001).

[57] Schimmel, H. G., Nijkamp, M. G., Kearley, G. J., Rivera, A., de Jong, K. P., and Mulder, F. M. *Mat. Sci. Eng. B* **108**, 124 (2004).

[58] Bienfait, M., Zeppenfeld, P., Dupont-Pavlovsky, N., Muris, M., Johnson, M. R., Wilson, T., DePies, M., and Vilches, O. E. *Phys. Rev. B* **70**, 035410 (2004).

[59] Muris, M., Bienfait, M., Zeppenfeld, P., Dupont-Pavlovsky, N., Johnson, M., Vilches, O. E., and Wilson, T. *Appl. Phys. A* **74**, S1293 (2002).

[60] Wilson, T., Tyburski, A., DePies, M. R., Vilches, O., Becquet, D., and Biefait, M. *J. Low Temp. Phys.* **126**, 403 (2002).

[61] Eswaramoorthy, M., Sen, R., and Rao, C. N. R. *Chem. Phys. Lett.* **304**, 207 (1999).

[62] Johnson, M. R., Rols, S., Wass, P., Muris, M., Bienfait, M., Zeppenfeld, P., and Dupont-Pavlovsky, N. *Chem. Phys.* **293**(2), 217 (2003).

[63] Schimmel, H. G., Kearley, G. J., and Mulder, F. M. *ChemPhysChem* **5**, 1053 (2004).

[64] Georgiev, P. A., Ross, D. K., Monte, A. D., Montaretto-Marullo, U., Edwards, R. A. H., Ramirez-Cuesta, A. J., and Colognesi, D. *J. Phys. Cond. Mat.* **16**, L73 (2004).

[65] Schimmel, H. G., Kearley, G. J., and Mulder, F. M. (2004). Unpublished results from TOSCA, ISIS, UK.

[66] Narehood, D. G., Pearce, J. V., Eklund, P., Sokol, P. E., Lechner, R. E., Pieper, J., Copley, J. R. D., and Cook, J. C. *Phys. Rev. B* **67**, 205409 (2003).

[67] Mackinnon, J. A., Eckert, J., Coker, D. F., and Bug, A. L. R. *J. Chem. Phys.* **114**, 10137 (2001).

[68] Rosi, N. L., Eckert, J., Vodak, M. E. D. T., Kim, J., OKeeffe, M., and Yaghi1, O. M. *Science* **300**, 1127 (2003).

[69] Rowsell, J. L. C., Millward, A. R., Park, K. S., and Yaghi, O. M. *J. Am. Chem. Soc.* **126**, 5666 (2004).

[70] Mao, W. L., Mao, H., Goncharov, A. F., Struzhkin, V. V., Guo, Q., Hu, J., Shu, J., Hemley, R. J., Somayazulu, M., and Zhao, Y. *Science* **297**, 2247 (2002).

[71] Florusse, L. J., Peters, C. J., Schoonman, J., Hester, K. C., Koh, C. A., Dec, S. F., Marsh, K. N., and Sloan, E. D. *Science* **306**, 469 (2004).

[72] van Mal, H. H., Buschow, K. H. J., and Miedema, A. R. *J. Less-Common Met.* **35**, 65 (1974).

[73] Fukai, Y. *Z. Phys. Chem.* **164**, 165 (1989).

[74] Flanagan, T. B. and Oates, W. A. *Hydrogen in Intermetallic Compounds II*, 49. Springer (1992). editor L. Schlapbach.

[75] Bogdanović, B. and Schwickardi, M. *J. Alloys Comp.* **253-254**, 1 (1997).

[76] Huot, J., Liang, G., and Schulz, R. *Appl. Phys. A* **72**, 187 (2001).

[77] Gérard, N. and Ono, S. *Hydrogen in Intermetallic Compounds II*, 165. Springer (1992). editor L. Schlapbach.

[78] Sastri, M. C. V., Viswanathan, B., and Murthy, S. S. *Metal Hydrides.* Springer-Verlag, Berlin, (1998).

[79] Sandrock, G., Suda, S., and Schlapbach, L. *Hydrogen in Intermetallic Compounds II*, 197. Springer (1992). editor L. Schlapbach.

[80] Zaluska, A., Zaluski, L., and Ström-Olsen, J. O. *J. Alloys Comp.* **288**, 217 (1999).

[81] Bloch, J. and Mintz, M. H. *J. Alloys Comp.* **253-254**, 529 (1997).

[82] Martin, M., Gommel, C., Borkhart, C., and Fromm, E. *J. All. Comp.* **238**, 193 (1996).

[83] Rudman, P. S. *J. Appl. Phys.* **50**, 7195 (1979).

[84] Luz, Z., Genossar, J., and Rudman, P. S. *J. Less-Common Met.* **73**, 113 (1980).

[85] Belkbir, L., Joly, E., and Gerard, N. *Int. J. Hydr. En.* **6**, 285 (1981).

[86] B. Vigeholm, K. Jensen, B. L. and Pedersen, A. S. *J. Less-Common Met.* **131**, 133 (1987).

[87] Zhdanov, V. P., Krozer, A., and Kasemo, B. *Phys. Rev. B* **47**, 11044 (1993).

[88] Gerasimov, K. B. and Ivanov, E. Y. *Mat. Lett.* **3**, 497 (1985).

[89] Gerasimov, K. B., Goldberg, E. L., and Ivanov, E. Y. *J. Less-Common Met.* **131**, 99 (1987).

[90] Mintz, M. H., Gavra, Z., and Hadari, Z. *J. Inorg. Nucl. Chem.* **40**, 765 (1978).

[91] Liang, G., Huot, J., Boily, S., and Schulz, R. *J. Alloys Comp.* **305**, 239 (2000).

[92] Renner, J. and Grabke, J. *Z. Metallk.* **69**, 639 (1978).

[93] Oelerich, W., Klassen, T., and Bormann, R. *J. Alloys Comp.* **315**, 237 (2001).

[94] Pelletier, J. F., Huot, J., Sutton, M., Schulz, R., Sandy, A. R., Lurio, L. B., and Mochrie, S. G. J. *Phys. Rev. B* **63**, 052103 (2001).

[95] Zaluski, L., Zaluska, A., and Ström-Olsen, J. O. *J. Alloys Comp.* **253-254**, 70 (1997).

[96] Huot, J., Liang, G., Boily, S., Neste, A. V., and Schulz, R. *J. Alloys Comp.* **293-295**, 495 (1999).

[97] Bortz, M., Bertheville, B., Böttger, G., and Yvon, K. *J. Alloys Comp.* **282**, 84 (1999).

[98] Eckold, G., Caspary, D., Elter, P., Guthoff, F., Hoser, A., and Schmidt, W. *Physica B* **350**, 83 (2004).

[99] Plazanet, M., Johnson, M. R., Gale, J. D., Yildirim, T., Kearley, G. J., Fernández-Díaz, M. T., Sánchez-Portal, D., Artacho, E., Soler, J. M., Ordejón, P., Garcia, A., and Trommsdorff, H. P. *Chem. Phys.* **261**, 189 (2000).

[100] Schimmel, H. G., Johnson, M. R., Kearley, G. J., Ramirez-Cuesta, A. J., Huot, J., and Mulder, F. M. *Mat. Sci. Eng. B* **108**, 38 (2004).

[101] Kresse, G. and Furthmüller, J. Software VASP, Vienna (1999); Phys.Rev. B **54**, 11 169 (1996); Comput.Mat.Science **6**, 15 (1996).

[102] Parlinski, K. Technical report, Cracow, Poland, (2001).

[103] Schimmel, H. G., Johnson, M. R., Kearley, G. J., Ramirez-Cuesta, A. J., Huot, J., and Mulder, F. *J. All. Comp.* (2004). accepted for publication.

[104] Zeng, K., Klassen, T., Oelerich, W., and Bormann, R. *Int. J. Hydrogen En.* **24**, 989 (1999).

[105] Nishimura, C., Komaki, M., and Amano, M. *J. Alloys Comp.* **293-295**, 329 (1999).

[106] Jacobson, N., Tegner, B., Schroeder, E., Hyldgaard, P., and Lundqvist, B. I. *Comp. Mat. Sc.* **24**, 273 (2002).

[107] Schimmel, H. G., Kearley, G. J., Huot, J., and Mulder, F. *J. All. Comp.* (2004). submitted.

[108] Kresse, G. http://cms.mpi.univie.ac.at/vasp/vasp/vasp.html.

[109] Liang, G., Huot, J., Boily, S., Neste, A. V., and Schulz, R. *J. Alloys Comp.* **291**, 295 (1999).

[110] Yavari, A. R., de Castro, J. F. R., Vaughan, G., and Heunen, G. *J. Alloys Comp.* **353**, 246 (2003).

[111] Kreuer, K. D. *Annu. Rev. Mater. Res.* **33**, 333 (2003).

[112] ILL: www.ill.fr and ISIS: www.isis.rl.ac.uk.

[113] Griffiths, D. J. *Introduction to quantum mechanics.* Prentice-Hall, (1995).

[114] Lovesey, S. W. *Theory of neutron scattering from condensed matter; nuclear scattering,* volume 1. Oxford University Press, New York, (1984).

[115] Schimmel, H. G., Montfrooij, W., Verhoeven, V. W. J., and de Schepper, I. M. *Europhys. Lett.* **60**, 868 (2002).

[116] Young, J. A. and Koppel, J. U. *Phys. Rev.* **135**, A603 (1964).

[117] Sears, V. F. *Can. J. Phys.* **44**, 1279 (1966).

[118] Carneiro, K., Nielsen, M., and McTague, J. P. *Phys. Rev. Lett.* **30**, 481 (1973).

[119] Leach, A. R. *Molecular modelling: principles and applications.* Prentice Hall, Harlow, UK, 2nd ed. edition, (2001).

[120] Koch, W. and Holthausen, M. C. *A chemists's guide to density functional theory.* Wiley-VCH, Weinheim, Germany, 2nd ed. edition, (2001).

[121] Payne, M. C., Teter, M. P., Allan, D. C., Arias, T. A., and Joannopoulos, J. D. *Rev. Mod. Phys.* **64**, 1045 (1992).

[122] Born, M. and Oppenheimer, J. R. *Ann. Physik* **84**, 457 (1927).

[123] Hohenberg, P. and Kohn, W. *Phys. Rev.* **136**, B864 (1964).

[124] Kohn, W. and Sham, L. J. *Phys. Rev.* **140**, A1133 (1965).

[125] Vanderbilt, D. *Phys.Rev. B* **41**, 7892 (1990).

[126] Kresse, G. and Hafner, J. *J. Phys.: Condens. Matter* **6**, 8245 (1994).

[127] Kresse, G. and Joubert, J. *Phys. Rev. B* **59**, 1758 (1999).

[128] Methfessel, M. and Paxton, A. T. *Phys. Rev. B* **40**, 3616 (1989).

[129] der Ven, A. V., Ceder, G., Asta, M., and Tepesch, P. D. *Phys.Rev. B* **64**, 184307 (2001).

[130] Attard, G. and Barnes, C. *Surfaces.* Oxford University Press, Oxford, (1998).

[131] Toebes, M. L., Bitter, J. H., van Dillen, A. J., and de Jong, K. P. *Cat. Today* **76**, 33 (2002).

[132] Mojet, B. L., Hoogenraad, M. S., van Dillen, A. J., Geus, J. W., and Koningsberger, D. C. *J. Chem. Soc., Far. Trans.* **93**, 4371 (1997).

[133] Du, W.-F., Wilson, L., Ripmeester, J., Dutrisac, R., Simard, B., and Dénommée, S. *Nano Lett.* **2**, 343 (2002).

[134] Nielsen, M. and Ellenson, W. *Proc. 14th Int. Conf. Low Temp. Phys.* **4**, 437 (1975).

[135] Talapatra, S., Krungleviciute, V., and Migone, A. D. *Phys. Rev. Lett.* **89**, 246106 (2002).

[136] Ramirez-Cuesta, A. J., Mitchell, P. C. H., and Parker, S. F. *J. Mol. Cat. A* **167**, 217 (2001).

[137] Nielsen, M., McTague, J. P., and Passell, L. *Phase Transition in Surface Films*, 127. Plenum, New York (1980). edited by J. G. Dash and J. Ruvalds.

[138] Stephens, P. W., Heiney, P. A., Birgeneau, R. J., Horn, P. M., Moncton, D. E., and Brown, G. S. *Phys. Rev. B* **29**, 3512 (1984).

[139] Freimuth, H. and Wiechert, H. *Surf. Sci.* **162**, 432 (1985).

[140] de Boer, J. H. *The dynamical character of adsorption.* Clarendon Press, Oxford, (1968).

[141] Sokol, P. E., Brown, D. W., and Fitzgerald, S. *J. Low Temp. Phys.* **113**, 717 (1998).

[142] See: www.isis.rl.ac.uk.

[143] Kearley, G. J. *Nucl. Instrum. Meth. A* **354**(1), 53 (1995).

[144] Johnson, M. R. and Trommsdorff, H. P. *Chem. Phys. Lett.* **364**(1-2), 34 (2002).

[145] Kresse, G. and Hafner, J. *Phys. Rev. B* **47**, 558 (1993). ; ibid **49**, 14 251 (1994).

[146] Parlinski, K., Li, Z. Q., and Kawazoe, Y. *Phys. Rev. Lett.* **78**, 4063 (1997).

[147] Parlinski, K. *Am. Inst. Phys. Conference Proceedings 479* , 121 (1999). edited by M. R.Johnson, G. J.Kearley, and H. G. Büttner.

[148] Zaluska, A., Zaluski, L., and Ström-Olsen, J. O. *J. Alloys Comp.* **289**, 197 (1999).

[149] Zuettel, A. *Naturwissenschaften* **91**, 157 (2004).

[150] Unpublished results from POLARIS (ISIS, UK) on the magnesium-hydrogen system, (2003).

[151] Massalski, T. B. *Binary alloy phase diagrams*, volume 3. Metals Park : ASM International, second edition, (1990).

[152] (editor), F. D. M. *Phase diagrams of binary hydrogen alloys.* ASM International, Materials Park, (2000).

[153] Williams, W. G., Ibberson, R. M., Day, P., and J.E.Enderby. *Physica B* **241-243**, 234 (1998).

[154] de Mattan, N., Husson, E., Gaucher, P., and Morell, A. *Mat. Res. Bul.* **25**, 427 (1990).

[155] Bonneau, P., Garnier, P., Calvarin, G., Husson, E., and Gavarri, J. R. *J. Solid State Chem.* **92**, 350 (1991).

[156] Turzhevsky, S. A., Novokov, D. L., Gubanov, V. A., and Freeman, A. J. *Phys. Rev. B* **50**, 3200 (1994).

[157] Casais, M. T., Alonso, J. A., Rasines, I., and Hidalgo, M. A. *Mat. Res. Bul.* **30**, 201 (1995).

[158] Grin, Y., Müller-Buschbaum, H., and von Schnering, H. G. *Zeit. Naturf. B.* **52**, 153 (1997).

[159] Borgschulte, A. *J. Alloys Comp.* (2005). conf. proc. MH2004, submitted.

[160] Balderas-Tapia, L., Wang, J. A., Hernandez-Perez, I., Aguilar-Rios, G. G., and Schacht, P. *Cat. Lett.* **58**, 3034 (2004).

[161] Carrazán, S., Peres, C., Bernard, J., Ruwet, M., Ruiz, P., and Delmon, B. *J. Cat.* **158**, 452 (1996).

[162] Niessen, R. A. H. *J. Alloys Comp.* (2005). conf. proc. MH2004, submitted.

Dankwoord

Met het gereedkomen van dit proefschrift sluit ik ook een belangrijke en interessante periode af. Ik heb de behoefte om verschillende mensen te bedanken voor hun bijdrage aan het werk waarvan ik verslag heb gedaan in dit boekje.

Fokko Mulder, je bent met recht mijn dagelijks begeleider geweest. Ik denk dat er weinig werkdagen zijn geweest waarop we elkaar niet hebben gesproken, over het onderzoek, maar ook over onze kinderen, de maatschappij en de wetenschap in het algemeen. Je doorzettingsvermogen in alle experimentele moeilijkheden en je gedrevenheid om goed onderzoek te doen en dit ook gepubliceerd te krijgen in kwaliteitstijdschriften, hebben me geïnspireerd. Het feit dat ik met plezier en genoegen terugdenk aan de afgelopen vier jaar, komt voor een groot deel door deze goede samenwerking. Don Kearley, bedankt voor de begeleiding, die –met name toen we experimenten deden bij het ILL– veel stoffelijker was dan die van de gemiddelde promotor. Ook het gebruik van simulaties om experimentele resultaten te kunnen interpreteren en begrijpen was heel verhelderend. Ik moet zeggen dat ik de waarde van simulaties nog niet inzag tot ik begon met mijn promotie. Daarnaast bedankt voor de prettige sfeer die er, mede door jouw manier van leidinggeven, op onze afdeling heerst.

Bij het doen van een promotieonderzoek waar het gebruik van brandbare gassen en hoge- en lage temperatuur bij elkaar komen, kon ik gelukkig gebruikmaken van de specialistische kennis en vaardigheden van velen binnen het IRI en daarbuiten. Ik noem graag Kees Langelaan, René den Oudsten, Piet van der Ende, Henk van der Made, Rien Waaijer, Kees de Vroege, Michel Steenvoorden, Kees Westerduin en vele anderen die ik in de loop der tijd lastig heb gevallen met allerhande vragen. Dankzij jullie inzet, vaak op korte termijn, heb ik met een beperkt budget toch mooie experimenten kunnen doen. Ben Bierling, bedankt voor het gangbaar houden van mijn computer. Marianne van Baaren, je bent zonder twijfel de meest belangrijke persoon van onze groep. Bedankt voor de leuke en besliste manier waarop je alles voor me regelde en voor alles waaraan je me hielp herinneren.

Many thanks for the people at ISIS and the ILL; John Dreyer, Chris Goodway, Timmy Ramirez-Cuesta, Mark Telling, Ron Smith, Laurent Chapon, John Stride and Mark Johnson that could arrange everything on short terms during our experi-

ments on different instruments. It was not your fault that we had to go home more than once without any data, or earlier than planned.

Voor de dagelijks benodigde hoeveelheid gespreksstof over andere zaken dan technisch-wetenschappelijke zorgden de contacten met Lambert van Eijck, Marnix Wagemaker, Alexander Schmets, Erik Offerman, Naveed Iqbal, Serdar Sakarya en eigenlijk alle andere leden van onze groep. Verder dank ik zonder alle namen te noemen mijn vrienden en familie voor de belangstelling en het meeleven met de voortgang.

Mijn ouders wil ik met name bedanken. Mijn vader omdat hij mij, zonder dat ik dat zelf besefte, zodanig beïnvloed heeft dat ik dezelfde studie heb gekozen. Technische natuurkunde is zonder twijfel de leukste studie. Dank u wel voor alle belangstelling voor de inhoud en gang van zaken van het onderzoek en voor de steun. Mijn moeder, omdat ze aandacht had voor zowel het onderzoek zelf als voor het proces, hoewel de belangrijkste adviezen werden gegeven op het laatste punt.

Jeannette, mijn lieve echtgenote, deze vier jaar hebben we samen meegemaakt. Ik ben elke dag blij dat we samen door het leven gaan. Bedankt voor je liefde en steun!

Bovenal komt God, die de kracht en het verstand heeft gegeven, de eer en de dank toe.

Curriculum vitae

I was born on the 4th of July in 1977. From 1989 to 1995 I attended the *Driestar College* in Gouda. In 1995 I started my study applied physics at the Delft University of Technology. During my study I worked for one year as teacher in physics and chemistry, again at the *Driestar College.* I finished my study with an undergraduate thesis entitled *A Neutron Scattering Study on Magnetic properties of $LiMn_2O_4$* in 2001. Next, I accepted a PhD position at the Interfaculty Reactor Institute, the scientific part of which is now known as the department of Radiation, Radionuclides and Reactors of the faculty of Applied Sciences of the Delft University of Technology. In this thesis, under supervision of Prof. dr. G.J. Kearley and Dr. F.M. Mulder, I describe my work on potential hydrogen storage compounds.

List of publications

1. *Neutron scattering investigation of the spin dynamics in $Li[Mn_{1.94}Li_{0.04}]O_{3.94}$*
   H.G. Schimmel, W. Montfrooij, G.J. Kearley, V.W.J. Verhoeven and I.M. de Schepper, *Physical Review B* **63**, 214409 (2001).

2. *Persistent frequency shifts in the dynamic structure factor of the quantum harmonic oscillator*
   H.G. Schimmel, W. Montfrooij, V.W.J. Verhoeven and I.M. de Schepper, *Europhysics Letters*, **60**, 868-874 (2002).

3. *Hydrogen adsorption in carbon nanostructures: Comparison of nanotubes, fibers, and coals*
   H.G. Schimmel, G.J. Kearley, M.G. Nijkamp, C.T. Visser, K.P. de Jong and F.M. Mulder, *Chemistry–A European Journal*, **9**, 4764-4770 (2003).

4. *The vibrational spectrum of magnesium hydride from inelastic neutron scattering and density functional theory*
   H.G. Schimmel, M.R. Johnson, G.J. Kearley, A.J. Ramirez-Cuesta, J. Huot and F.M. Mulder, *Materials Science and Engineering B-Solid State Materials for Advanced Technology*, **108**, 38-41 (2004).

5. *Hydrogen adsorption in carbon nanostructures compared*
   H.G. Schimmel, M.G. Nijkamp, G.J. Kearley, A. Rivera, K.P. de Jong and F.M. Mulder, *Materials Science and Engineering B-Solid State Materials for Advanced Technology*, **108**, 124-129 (2004).

6. *Resolving Rotational Spectra of Hydrogen Adsorbed on a Single- Walled Carbon Nanotube Substrate*
   H.Gijs Schimmel, Gordon J. Kearley and Fokko M. Mulder, *ChemPhysChem*, **5**, 1053-1055 (2004).

7. *Hydrogen in magnesium metal (alpha phase) observed using neutron diffraction and simulations*
   H.G. Schimmel, G.J. Kearley, J. Huot and F.M. Mulder, submitted to *Journal of Alloys and Compounds*.

8. *Structural Information on Ball Milled Magnesium Hydride from Vibrational Spectroscopy and Ab-Initio calculations*
H.G. Schimmel, M.R. Johnson, G.J. Kearley, A.J. Ramirez-Cuesta, J. Huot and F.M. Mulder, accepted by *Journal of Alloys and Compounds.*

9. *Spontaneous aligned domains of single walled nanotube bundles on mm length scales*
F.M. Mulder, J. Plomp, H.G. Schimmel, T.V. Krouglov, W.G. Bouwman and M.T. Rekveldt, submitted to *Physical Review Letters.*

10. *Hydrogen sorption of Nb-catalysed nanostructured Mg*
Fokko M. Mulder, H. Gijs Schimmel, Jacques Huot and Laurent C. Chapon, *ISIS anual report 2004 – Highlight article.*

11. *In-situ neutron diffraction during hydrogen cycling of niobium-catalyzed magnesium*
H. Gijs Schimmel, Jacques Huot, Laurent C. Chapon and Fokko M. Mulder, manuscript in preparation.